POLITECNICO DI MILANO

Scuola di Ingegneria Industriale e dell'Informazione

Corso di Laurea Magistrale in Ingegneria Elettrica

Performance Analysis of Time-Reversal MUSIC for Soft Fault Location in Power Cables

Relatore: Flavia Grassi

Tesi di Laurea di:
Manuel Bestetti
852711

Anno Accademico 2017-2018

Prefazione

Oggigiorno il trasferimento di energia e informazioni è costantemente in aumento dato dallo sviluppo delle nuove tecnologie nel campo elettrico ed elettronico. Il ruolo dei cavi elettrici diventa dunque essenziale per assicurare buone prestazioni e il loro stato di salute deve essere periodicamente monitorato. Tuttavia, improvvisamente guasti si originano dal deterioramento, classificati in due categorie principali: *guasti gravi*, come corto-circuiti e circuiti aperti, e *guasti lievi*, come danni di isolamento, crepe, ecc., che sono spesso difficili da rilevare a causa della loro bassa riflettività e rappresentano un passo preliminare verso guasti gravi. A tale scopo è necessaria la disponibilità di tecniche in grado di rilevare i guasti al fine di garantire una migliore affidabilità del cavo. Negli ultimi decenni le tecniche basate sulla riflettometria, in particolare quella nel dominio del tempo (TDR), sono state le più comuni nelle applicazioni industriali per la localizzazione dei guasti ma, nonostante i loro risultati ottimali, presentano alcune limitazioni in presenza di gusti lievi e soprattutto quando si introducono perdite, il che si traduce in un deterioramento della stima di precisione.

Per superare questi problemi, lo sviluppo di nuove tecniche per la localizzazione dei guasti è sempre più studiato. In particolare, negli ultimi anni i metodi basati sull’inversione temporale (time reversal) hanno mostrato grandi vantaggi in questo campo, in particolare due delle sue metodologie: Décomposition de l’Opérateur de Retournement Temporel (DORT) e Time Reversal-MUltiple SIgnal Classification (TR-MUSIC). In questo lavoro TR-MUSIC è presentato e analizzato nelle sue prestazioni. Viene eseguito un accurato studio metrologico di questa tecnica, in cui precisione e accuratezza sono sono studiate sui cavi di potenza. La caratteristica più sorprendente di TR-MUSIC è che garantisce una super risoluzione mentre lavora a frequenze singole, basata sull’analisi della funzione di Green, e mostra anche una buona robustezza del rumore anche per valori di SNR relativamente bassi. In primo luogo, vengono presentate le basi teoriche sui cavi elettrici e il metodo operativo di TDR, mentre nel secondo capitolo viene presentato uno studio sul cavo adottato nel nostro lavoro. Nella terza sezione viene mostrata la teoria e una panoramica sui metodi a inversione temporale. Infine, negli ultimi tre capitoli, vengono presentati i risultati delle simulazioni e degli esperimenti effettuati nel lavoro e

viene eseguito un confronto delle prestazioni tra TR-MUSIC e TDR quando un singolo guasto è presente. In particolare, nel capitolo 4 la precisione e l'accuratezza di entrambi i metodi sono studiate e confrontate in una singola linea senza perdite; nel capitolo 5 vengono introdotte le perdite e nel capitolo 6 le loro prestazioni sono studiate in una rete ramificata a Y.

MUSIC mostra la stessa stima di accuratezza e una risoluzione molto più elevata in precisione rispetto a TDR in assenza di perdite, il che lo rende molto interessante come metodo di localizzazione dei guasti. Operando solo su pattern di fase, in presenza di perdite l'attenuazione non influisce sulle prestazioni, non provocando quindi un deterioramento della risoluzione; inoltre, anche guasti molto lievi possono essere facilmente rilevati. Risultati interessanti si ottengono anche in presenza di rete ramificata, in cui si ottiene un'ottima precisione e si evita l'effetto indesiderato della giunzione mediante il cosiddetto *sistema di baselining*. Per concludere, TR-MUSIC ottiene buoni risultati con reti singole e ramificate, con e senza perdite. Tuttavia, uno studio più esteso per migliorare le prestazioni del metodo può essere condotto in futuro. Alcune di queste prospettive sono illustrate, come lo studio di topologie di linea più complesse o l'analisi in presenza di guasti multipli. Esperimenti e misure hanno avuto luogo presso le strutture di Centrale Supélec (Gif-sur-Yvette, Francia).

Parole chiave: Cavo di potenza, localizzazione di guasti, inversione temporale, parametri scattering, funzione di Green, statistica applicata, misure con VNA.

Abstract

NOWADAYS transfer of energy and information is constantly growing due to the development of new electrical and electronic technologies. The role of electrical cables thus becomes essential to ensure good performances of the whole system and their state of health shall be periodically checked. Suddenly, deterioration occurs eventually causing wiring faults, classified into two main categories: *hard faults*, as short and open circuits, characterized by the fact that they prevent any signal from going further away, and *soft faults*, as insulation damage, cracks etc., which are often difficult to detect due to its weak reflectiveness and represent a preliminary step towards the occurrence of hard faults. For this purpose, the availability of techniques able of detecting faults is necessary in order to guarantee a better cable reliability. In the last few decades the reflectometry-based techniques, in particular the one in time-domain (TDR), has been the most common in industrial applications for fault detection but, despite their optimal results, some limitations occur above all in presence of soft faults and when losses are introduced.

In order to overcome these problems, the development of new fault location techniques is increasingly studied. Accordingly, in the last years time reversal based methods have shown great advantages in this field, in particular two of its methodologies: Décomposition de l' Opérateur de Retournement Temporel (DORT) and Time Reversal - MUltiple SIgnal Classification (TR-MUSIC). In this work TR-MUSIC is presented and analyzed in its performances. A fine metrological study of this technique is carried out, and its precision and accuracy are investigated on medium voltage power cables. The most striking feature of TR-MUSIC is that it ensures a *super resolution* while working at single frequencies, based on Green function phase patterns analysis, and also shows good noise robustness even for low SNR values. Firstly, theoretical background on electrical cables and the operational way of TDR are presented whereas in the second chapter a study of the MV power cable adopted in our work is introduced. In the third section, background, theory and an overview of time reversal is shown. Then, in the last three chapters, the results of simulations and experiments carried out in the work are presented and a performances comparison between TR-MUSIC and TDR for single soft fault made. In particular, in chapter 4 precision and accuracy of both methods are investigated and compared in a single lossless line; in chapter 5 losses are introduced and in chapter 6 their performances are studied in a Y-branched network.

Port MUSIC shows the same accuracy estimation and a much higher resolution in precision with respect to TDR in absence of losses, making it very interesting as fault location method. Operating on phase pattens only, in presence of losses attenuation does not affect its performances, thus not causing a resolution deterioration; besides, very soft faults can be easily detected. Interesting results are also obtained in presence of three branches, where the same precision is performed and the undesired effect of the junction is avoided by means of the so-called *baselining system*. To conclude, TR-MUSIC performs good results with single as well as Y-branched networks in lossless and lossy conditions. However, an extended study could be continued in order to still improve the method's performances. Some of these perspectives are illustrated, as the study of more complex line topologies or the analysis in presence of multiple faults. Experiments and measurements took place in Centrale Supélec's (Gif-sur-Yvette, France) facilities.

Key words: Power cable, Fault detection, Time reversal, Scattering parameters, Green function, Eigendecomposition, Statistics, VNA Experimental validation.

Contents

Chapter 1

General Introduction

In the recent past, the increasing demand of electrical cables due to its fundamental role in transfer of energy and signals brought to the development of new technologies and structures aimed to improve their functionality and reduce the occurrence of faults. In this first chapter, the different types of cables present nowadays and their main applications are introduced, together with the types of faults that could jeopardize the healthy situation of a cable. Accordingly, some fault location techniques as reflectometry (in particular TDR) and TR-MUSIC are briefly presented in its strengths and limitations.

Then, a theory background is recalled, where important concepts in transmission lines useful for the operational mode applied in this work are discussed.

At last, a description of the thesis organization is carried out, where the main concepts treated in each chapter are presented.

1.1 Introduction to Electrical Cables

In 1892, Thomas Edison filed an electrical conductor and surrounded it by insulating material resistant to both fire and moisture, given birth to the first known electrical cable [1]. Practically, given a point A and a point B, it is quite simple getting an electrical signal, just connecting them trough a piece of copper wire. Developments and specializations in wiring have been studied during the *XX* century, bringing to get very powerful and complex structures and making them indispensable in all modern electrical and electronic systems. As a matter of fact, cables represent their backbone structures, acting as the nervous system in the human body where signals, power and commands are delivered to their destinations. Nowadays, electrical cables are everywhere and the increasing complexity in modern electronic and electric systems, such as automotive or avionics fields, have witnessed a huge reckoning on the extensive use of electrical wires. For instance, today's vehicles are not only equipments used just for transporting individuals, but they

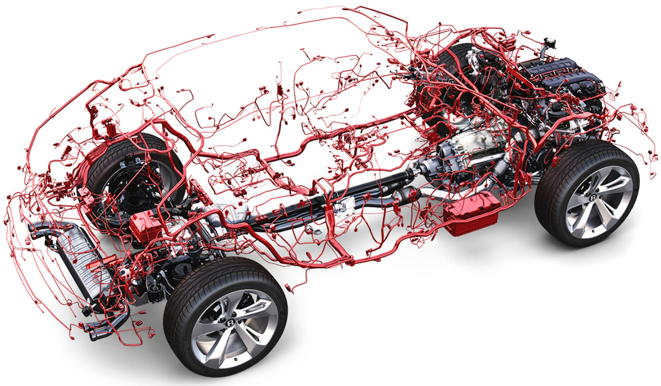

Figure 1-1. A complete network of electrical cables of a typical modern car with bundles of cables in addition to their connectors referred to as the automotive wire harness

have included leisure and entertainment facilities as AC, radio, TV, navigation systems, etc., thus necessitating the presence of wiring networks. In figure 1-1, an electrical cable network in a typical modern car showing bundles of long cables with their connectors is represented, where statistics conducted result that about 35% of the total vehicle infrastructure is electrical based. As a consequence, from few hundred of meters in vehicles some years ago, now modern cars contain about 4km; besides, wire lengths have also increased to several hundred km in civil and military airplanes and even more than 1200km in transport ships. Figure 1-2 describes the cable lengths in different transport systems. Moreover, estimates have shown that about 5000km are present in a nuclear power plant which can skyrocket to 40000km of cables in railway infrastructures of large countries like China and U.S [2]. A large variety of different cable structures exist and, in particular, three main types of cables are the most common: power, coaxial and twisted pair cables. Power cables are usually used for the transmission of electrical power at medium/high voltage, both in the AC or DC mode. They originate from power plants to distribution stations which are responsible for supplying this electrical power to different electricity using facilities. They are made up by different layers, specifically detailed in the next chapter, and they are very used for underground applications. Since they are adopted in high voltage field, particular big sections are required, as shown in figure 1-3

Twisted pair cables have been introduced by Alexander Graham Bell in 1881 [4], for telephone applications in order to reduce crosstalk or electromagnetic induction (EMI) between pairs of wires. Two insulated copper wires are twisted around each other, where each connection on a twisted pair requires both wires (a forward and a return conductor of a single circuit). Although the twisted pair cable is used by older telephone networks and is the least expensive type of local area network (LAN) cable, most systems still contain them at some point along the network. Fiber optic cables and coaxial cables are now widely adopted for LANs.

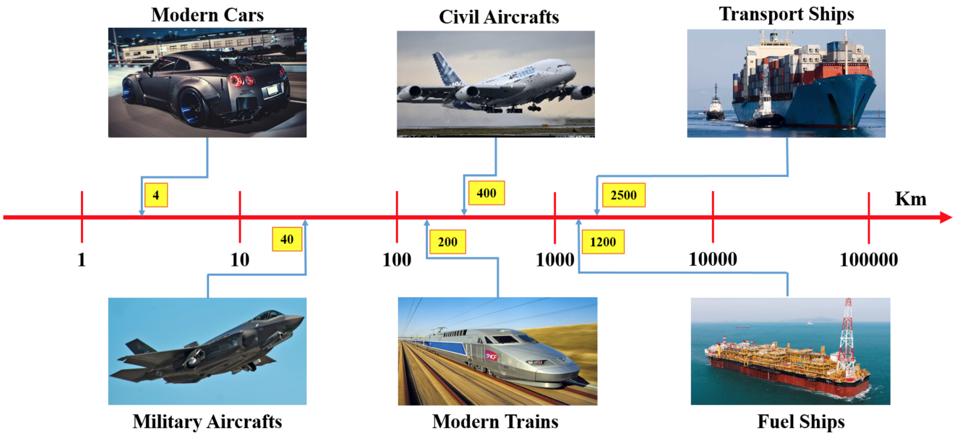

Figure 1-2. Cumulated lengths of electrical cables in transportation systems [3]

A coaxial cable is a type of cable made up by an inner conductor surrounded by a cylindrical insulating layer, which is in turn surrounded by a conducting shield. Coaxial cables are mainly used as transmission lines for radio frequency signals. Their applications include feedlines connecting radio transmitters and receivers with their antennas, computer network connections, digital audio and distributing cable television signals.

In this work, a study of medium voltage power cables will be carried out and it is worthy to note that in our numerical model we used uniform two-wire transmission lines in order to validate the proposed methods for locating faults, while smaller coaxial cables were used in the experimental measurements. Notably, the latter kind of cables allowed comparing the experimental results with the numerical ones, besides they have connectors compatible with most vector network analyzers used for measurements. The same conditions between the numerical and experimental measurements are verified in order to entirely validate the model.

Figure 1-3. Underground high voltage power cables

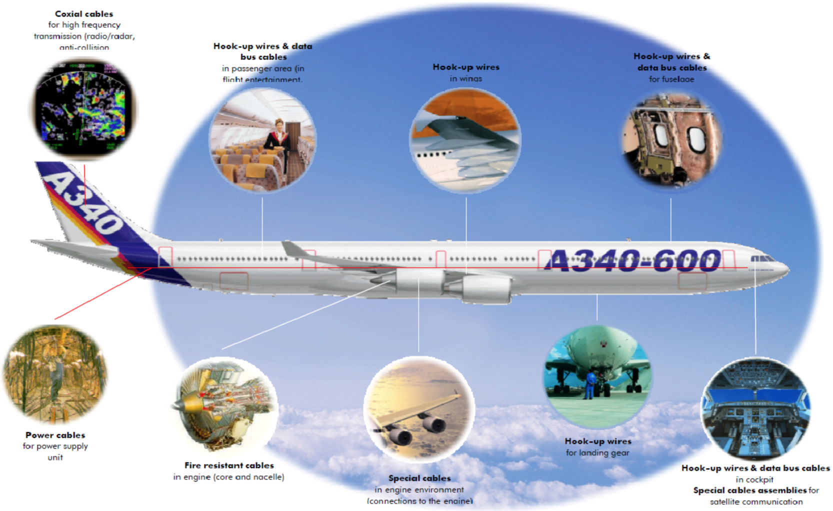

Figure 1-4. A map showing different cable types with their function in an Airbus A340 aircraft [3]

In this section some of the most common cables are introduced, but it is important to note that a very large variety of cables with different functions and applications can be found. As a proof, in figure 1-4 the total cable network present in a single airplane, an Airbus A340, is shown. Due to this massive use of wiring networks in nowadays systems, one day or another, a cable in a network will show signs of weakness or aging leading to the appearance of defects. These anomalies can be the origin of dysfunctions and imply serious consequences for the system or the environment. In fact these defects, hereafter referred to as wiring faults, can be categorized in two main families: hard or soft faults. In the next section, the main reasons behind the occurrence of each of them will be illustrated.

1.1.1 Wiring Faults

Many researches and efforts to protect cables against damaging factors have been adopted in the last few years, but nevertheless, wires are still subject to undesired modifications and breakdowns. Depending on the application field, the consequences of such a performance degradation could be catastrophic and fatal especially when it refers to areas inhabited by humans. Numerous incidents, in many sectors, have happened and billions of dollars have been wasted. Industry facilities, buildings, transportation systems and space/avionic companies are some of the sectors hit by this kind of problem. For example, in May of 1986, a NASA Delta 3925 rocket booster carrying a GOES (Geostationary Operational Environmental Satellite) weather satellite failed due to a momentary short caused by a chafed wire. An Air Force Titan 4B broke up when a short circuit occurred, and 13 years earlier, the failure of another Delta was also due to a chafed wire that caused

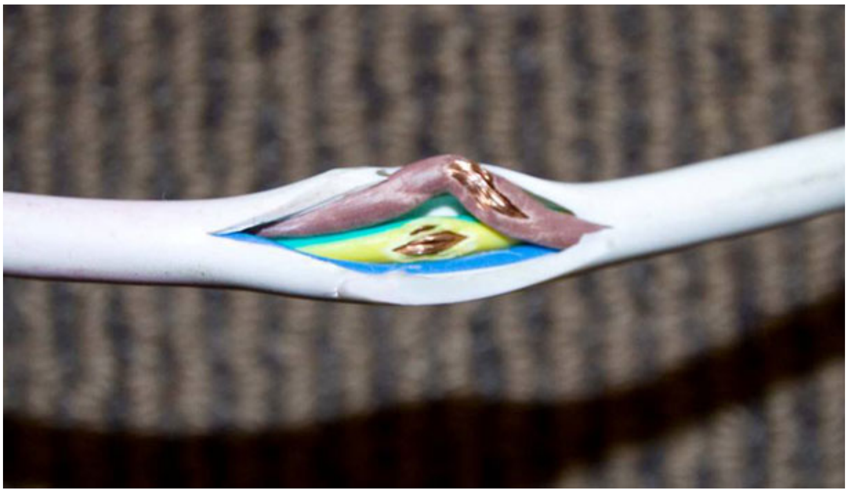

Figure 1-5. Example of cable degradation

short circuits [5]. Nevertheless, it was not until the TWA tragedy in 1996 that governments and industries started seriously looking for solutions to this problem. Generally, the main causes of degradation and appearance of defects in cables can be either of external (chemical contamination, water penetration, corrosion ans oxidation) or internal (manufacturer defects, local heating) origins [6]. An example of cable damage is shown in figure 1-5.

The most common defects are short and open circuits which are the sources of many fires or signal losses [7]. They are called ‘‘*hard faults* ”, and are characterized by the fact that they prevent any signal from going further away. ‘‘*Soft faults* ”, are the second group of wiring defects which are basically of very different kind and are usually more difficult to detect [8]. Generally, any fault which is not considered hard shall be defined as a soft one, these include insulation damage, cracks, frays, etc. Significantly, a precise knowledge of the fault’ s reflection coefficient might allow a better assessment about the type of fault: hard faults are characterized by a strong reflection coefficient while, on the other hand, a weak reflection coefficient is related to soft faults, which could make difficult to see the reflected wave.

Consequently, detection and repair of a wiring fault becomes essential especially when a wiring fault might lead to destructive consequences, from expensive, economic and human lives terms. Therefore, proper and efficient wire diagnosis tools become strongly recommended to prevent the fatal consequences that may be verified.

1.1.2 Reflectometry Based Techniques

In order to have diagnostic tools capable anticipating or detecting the occurrence of faults in wiring networks, both hard ad soft, many methods have been developed throughout the

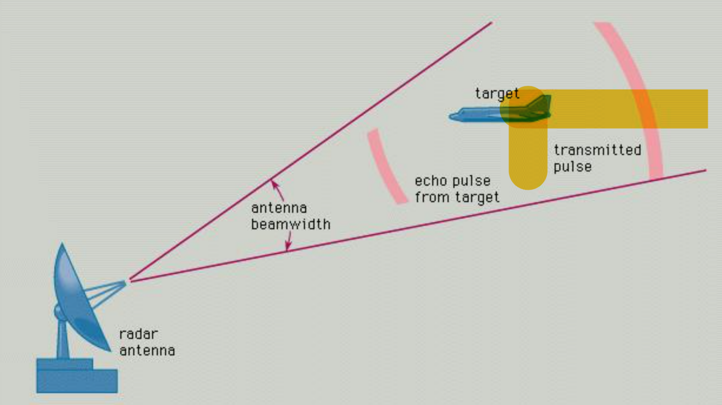

Figure 1-6. Radar systems using reflectometry principle for locating targets [3]

last few decades to test the condition of cables, most of which were devoted for locating hard faults only. Generally, such kinds of faults are easier to detect and locate as they are characterized by high reflection coefficients [9]. However, studies have reported that a wide majority of wiring defects are considered to be soft, and these types of faults are not considered dangerous since they do not posses direct consequences for a system breakdown. Nevertheless, they must not be underestimated, since a soft fault will develop sooner or later into a hard one, thus leading to devastating damages.

Two main categories of fault location techniques are common and largely used in the last decades, but in this section only the reflectometry-based techniques will be presented. The reason behind this choice is that they are the most widely used methods in this domain as they have presented effectual results compared to other traditional non-reflectometry based methods, although they also present some limitations.

Reflectometry is a high frequency technique of investigation, imaging or nondestructive testing, dated back to the late 1930's as a technique catching the attention of mainly geologists and other scientists. The basic principle is simple to implement: a probe signal is sent to the system or environment, this signal travels under the laws of propagation of the medium studied and when it encounters an obstacle a portion of its energy is reflected back to the point of injection. The analysis of this reflected signal is carried out to obtain information about the system or the environment to diagnose.

Reflectometry has found its place in many different applications starting from radar systems where it has been used extensively for detecting and measuring the distance to a target (e.g aircraft) as shown in figure 1-6. Geotechnology [10], hydrology [11] and telecommunication networks are other forms of reflectometry applications [12]. The electronic measuring instrument used for characterizing and locating faults with reflectometry in electric cables is called reflectometer. The reflectometer setup is composed of a signal generator, a coupler, an oscilloscope and the tested cable as shown in figure 1-7, where the corresponding tool used to demonstrate the results is referred to as the

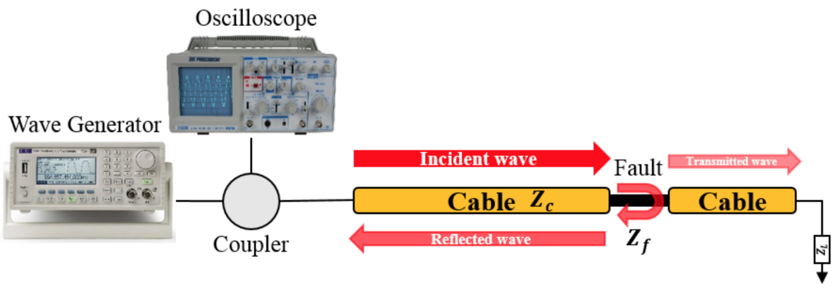

Figure 1-7. A scheme showing the principal of reflectometry

reflectogram. The process of detecting a fault can be summarized as follows: the signal generator emits for example a step-like pulse which propagates along the cable. When this pulse encounter an impedance discontinuity, i.e. fault, part will be reflected back and another will continue propagating along the cable. The reflected wave front goes back to the injection point where an oscilloscope records the signal amplitude variations over time, and consequently the analysis of the reflected signal can infer information about the system, as fault position, or the medium under consideration. The reflection coefficient Γ_f of the impedance discontinuity can also be retrieved and it gives information about the intensity of the discontinuity:

$$\Gamma_f = \frac{V_{reflected}}{V_{incident}} = \frac{Z_c - Z_f}{Z_c + Z_f}, \tag{1.1}$$

where Z_c is the characteristic impedance of the transmission line and Z_f is the impedance of the discontinuity. For instance, the reflection coefficient of an open circuit ($Z_f = \infty$) is 1, while is -1 for a short circuit ($Z_f = 0$). The time or phase delay between the incident and the reflected waves tells the distance of the fault, while the magnitude its intensity. As a matter of fact, reflectometry showed promising results when dealing with hard faults but failed when addressing soft ones depicted by weak reflectivities [13]. In order to better illustrate this point, the reflectogram of figure 1-8 showing the spread spectrum reflectometry (SSTDR) responses, where SSTDR is a type of reflectometry methods, is considered for fault impedances ranging from 20Ω to 2000Ω for a 50Ω coaxial cable [14]. It can be inferred that faults with high impedance discontinuities (20% of Zc) are relatively easy to detect and locate due to their relatively high peaks. On the other hand, fault impedances below this value become progressively more difficult to identify as their response is much smaller than even the measurement errors.

Basically, reflectometry can be divided into two main families: time domain family methods (TDR) and frequency domain family methods (FDR). However, in time domain better results are obtained and it is largely most adopted in many application fields.

In its standard form, TDR injects a short rise time voltage step as an incident signal

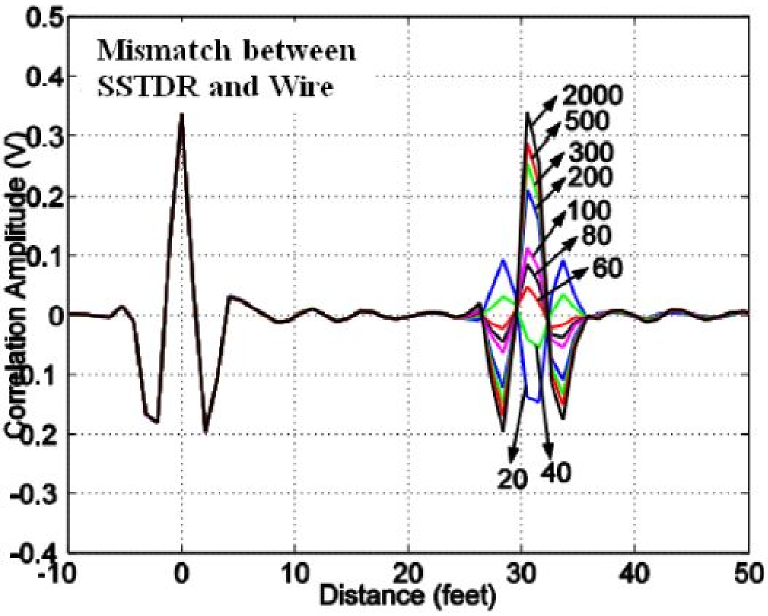

Figure 1-8. A reflectogram showing the responses of a spread spectrum reflectometry (SSTDR) for different load impedances for a 50Ω coaxial cable [14]

where reflected voltages from impedance discontinuities are also step functions. Consequently, the position of the fault d is retrieved from the round trip time delay τ between the incident and reflected waves and the velocity of wave propagation (v_p) of the cable, given by:

$$d = \frac{v_p \tau}{2}. \tag{1.2}$$

Optimal results have obtained with TDR in lossless case and when hard faults are dealt, but nevertheless several limitations arise which could jeopardize the fault detection or location. Following, some of these limitations are listed, which represent a good starting point to introduce the time reversal based methods.

Firstly, TDR methods face the so-called "*blind zone*" limitation. If the system is not matched to the intrinsic impedance of the cable, part of the energy of the injected signal is directly sent back, without even going inside the cable. This creates an additional high amplitude peak at the beginning of the reflectogram which may hide a defect close to the injection point. Distributed reflectometry [15] can be adopted to face this problem, where instead of using a single testing port as used in standard TDR techniques, multiple testing ports are used. In the single Y-junction network of figure 1-9 a standard TDR injects a single testing signal using one of the three ports (a), while distributed TDR uses all the testing ports (b). Accordingly, two important limitations can be bypassed: firstly, this new technique would be removing the *blind zone* effect by using several testing ports

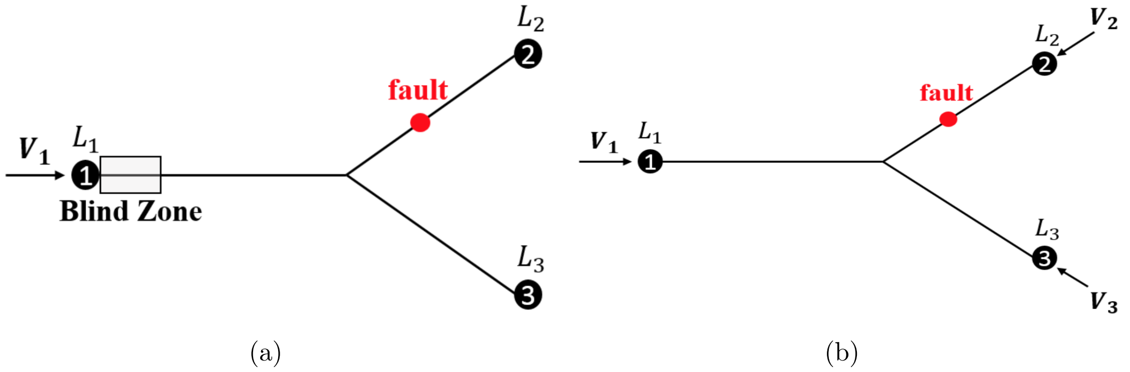

Figure 1-9. A single Y-junction network where TDR method was applied in (a) standard version using a single testing port, (d) distributed form using multiple testing ports

rather than only the affected one, and besides it is capable of eliminating any ambiguity on the fault's location with respect to the branches of the network.

Furthermore, any uncertainty on the value of v_p will decrease the accuracy about the value of defect distance since the propagation speed depends on frequency. Then, as the probe signal' s bandwidth may be quite large, it is not possible to precisely define the propagation speed for the whole signal and greater the bandwidth, worse the result is.

But the greatest problem of TDR is related to the presence of losses, since it relies on the presence of large bandwidths for obtaining a good spatial resolution for the location of the fault. However, large bandwidths are not always satisfied especially with band-limited systems or when attenuation and dispersion are introduced.

Notably, time reversal based fault detection techniques have shown a great efficiency in locating soft faults and represent a valid alternative to reflectometry. In this work one of its methodologies is developed, TR-MUSIC, which operates with a continuous wave excitation (single tone, no bandwidth). The performances comparison between the methods will be analyzed and shown in this work, under several points of view.

1.1.3 TR-MUSIC and Past Works

Studies conducted on time reversal have shown optimal results in fault detection reported by several experiments. In particular two TR methods, which share the same foundations but different way of working, have resulted in very good performances: DORT and TR-MUSIC. Both the methods are illustrated and performed in this work (see chapter 3) for the soft fault location on MV power cables, but DORT does not show any advantages with respect to TDR in our studied case (single fault, matched load) since its approach is based on time-domain too. On the contrary, TR-MUSIC has revealed interesting results and a comparison in its performances with TDR is carried out. It does not operate on time-domain but on Green function analysis: as result, the main feature of this technique is its ability of performing *super resolution* even in presence of losses and working at single frequencies. Besides, good results in noise robustness are also obtained.

The method has been introduced for the first time by R. O. Schmidt in 1979 [16] in the field of antenna applications conducted in open media. Related to this topic, many works have been carried on by C. Prada and M. Fink from 70's to 90's and the cited papers are inserted in this work.

In the recent past, this technique has been developed in guided wave propagation too, about which several studies and experiments have been conducted both from academic and industrial point of view. Specifically, many works performed by F. Rachidi and his group (École Polytechnique Fédérale de Lausanne) and by A. Cozza (Centrale Supélec) have been resulted very useful in the research and development of this technique and have been inspiration for this thesis work. Especially, prof. A. Cozza carefully supervised the results obtained in this work and three his previous works ([3], [17], [14]) have represented a good starting point. The results obtained in these cited papers were very satisfactory, referred to short lossless cables.

As a matter of fact, no works related to fault detection have been done in presence of losses and very few works on long power cables: the behavior of such a method at these conditions is studied in this work and a fine comparison with TDR is carried out. Thus, the principal purpose of this thesis is the analysis of TR-MUSIC without and with losses on power cables, in order to overcome the limitations arisen with TDR for soft fault location. A single fault and a matched line scenario is considered as hypothesis for this work.

1.2 Theory Background

In order to better understand the operational mode of different fault location methods studied in this work, understanding how an electromagnetic wave propagates in a transmission line is necessary. The aim of this section is first to position this work within the framework of the transmission line theory and then in the context of the wiring modeling techniques.

A transmission line is a system of metal conductors and dielectric insulating media that is capable of transferring energy between a generator and a load. From this point of view, a one dimensional propagation phenomenon takes place on a transmission line.

There are many types of transmission lines, as shown in figure 1-10 and they can be divided into two main categories, according to the propagation mode. If both the electric and magnetic fields are entirely transverse to the direction of propagation of the traveling wave, the transmission line is in *TEM* (Tranverse ElectroMagnetic) mode.

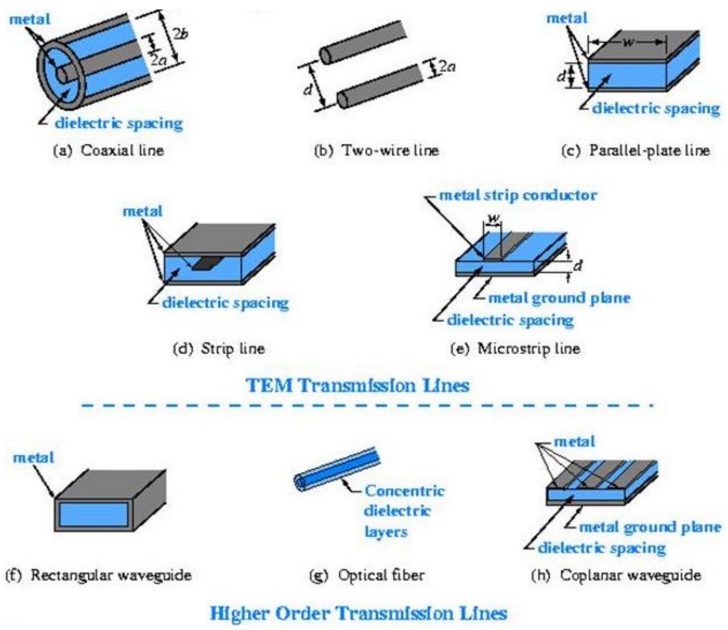

Figure 1-10. Examples of transmission lines: above the TEM mode is represented and below the higher terms mode [18]

This mode is particularly interested, since contains structures consisting of two metal conductors, such as coaxial cables, used in our numerical simulations and experimental measurements. Instead, if at least one significant field component is in throughout the direction of propagation, the transmission line is in *higher terms mode.* At low frequencies, the wavelength λ is greater than the length l of the transmission line, thus the wave is almost constant at any point on the line. In this case, it is unnecessary to introduce the concept of propagation. On the other hand, at high frequencies λ becomes less than the length l of the line and the amplitude of the wave is no longer constant throughout the line. In this case, the propagation phenomenon must be taken into account. Accordingly, the conductors shall have the same geometric shape both in length and cross-section and the electric and magnetic fields must be considered transverse at the wave direction of propagation at each point.

1.2.1 Transmission Lines: Behavior and Concepts

In this work, a coaxial cable is considered as network under test for the fault location methods' application, under the assumption that both the electric and magnetic field are transverse to the direction of propagation (TEM mode). A two-conductor line is introduced and a set of coupling partial differential equations are obtained for the transmission line considered [18]. In particular, the TEM transmission line represented in figure 1-11 with the four lumped electrical parameters is considered, R and L account for loss and energy storage in the conductors, and C and G for installation and loss in the insulator,

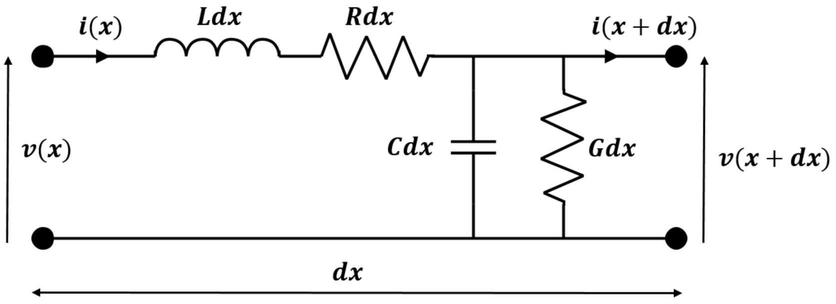

Figure 1-11. Equivalent circuit of a small of a transmission line, showing the per-unit-length parameters R, L, C, and G [18]

which are explained as follows:

(1) the per unit length resistance R in (Ω/m). This resistance varies with frequency due to the skin and proximity effects;

(2) the per unit length inductance L in (H/m). This inductance depends on the diameter of the conductors, the spacing between the two conductors and permeability of materials;

(3) the per unit length capacitance C in (F/m). This capacitance depends on the permittivity of the dielectric located between the conductors;

(4) the per unit length conductance G in (S/m) which reflects the losses due to the dielectric. This conductance depends on the distributed capacitance and dielectric loss angle tanδ.

Applying the Kirkhhoff's laws to the transmission line before introduced the following equations are found:

$$\frac{\partial v(x,t)}{\partial x} = -Ri(x,t) - L\frac{\partial i(x,t)}{\partial t}, \tag{1.3}$$

$$\frac{\partial i(x,t)}{\partial x} = -Gv(x,t) - C\frac{\partial v(x,t)}{\partial t}. \tag{1.4}$$

Considering a lossless line (R=G=0) and differentiating one equation with respect to x and the other one with respect to t, the Telegraph's equations are obtained as follows

$$\frac{\partial^2 v(x,t)}{\partial x^2} = -LC\frac{\partial^2 v(x,t)}{\partial t^2}, \tag{1.5}$$

$$\frac{\partial^2 i(x,t)}{\partial x^2} = -LC\frac{\partial^2 i(x,t)}{\partial t^2}. \tag{1.6}$$

The solutions of the Telegraph's equations given by 1.5 and 1.6 can be obtained by the analysis in time and frequency domain [19].

Time domain analysis allows to analyze the propagation of the signals in a network. There exist many commercial full Maxwell solvers, such as CST MicroWave Studio [20], that permit to simulate wire networks using different circuit analysis methods such as matrix formulation, state variable, etc [21]. The time domain analysis is today' s one of the most popular techniques for the solution of electromagnetic problems [22]. In fact, it allows to obtain a short development time and an easy of understanding the procedure, due to a simple discretization procedure. However, it presents also some disadvantages, which can be listed as follows:

(1) *stair-stepping edges*, the orthogonal grid structure of the TD method implies that edges of structures within the simulation have edges that follow the grid structure;

(2) *computational time*, for simulations with large spaces or multiple scales (largely varying wavelengths), this means the simulation must be run for a very long time.

Accordingly, it is easier to start the analysis in frequency domain and switching back in time domain afterwards.

Given the circuit of figure 1-12, and let *V(x,t)* and *I(x,t)* the voltage and the current at any position x of the transmission line, it is possible to express them in their phase notation, in time domain, taking the form of single-tone sinewaves:

$$V(x,t) = \Re\boldsymbol{e}(V(x)e^{j\omega t}) \tag{1.7}$$

$$I(x,t) = \Re\boldsymbol{e}(I(x)e^{j\omega t}), \tag{1.8}$$

The voltage and current at the position x can be found by solving the two wave equations:

$$\frac{\partial^2 V(x,t)}{\partial x^2} = ZYV(x) = \gamma^2 V(x), \tag{1.9}$$

$$\frac{\partial^2 I(x,t)}{\partial x^2} = ZYI(x) = \gamma^2 I(x), \tag{1.10}$$

where $Z=R+j\omega L$ is the impedance in Ω/m, $Y=G+j\omega C$ is the admittance in S/m, and γ is the complex propagation constant given by:

$$\gamma = \sqrt{(R+j\omega L)(G+j\omega C)} = \alpha + j\beta, \tag{1.11}$$

with α and β being the attenuation constant in Nepers/m and the phase constant in radians/m, respectively.

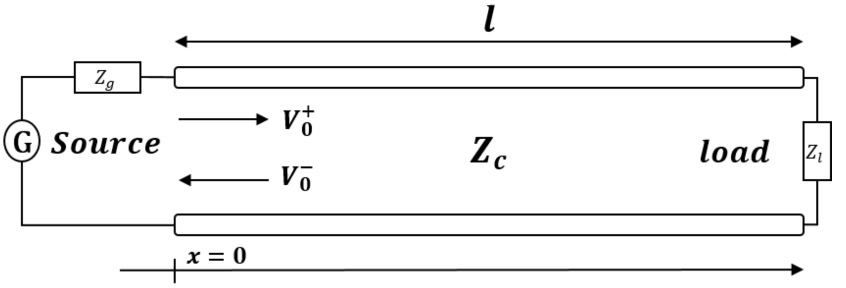

Figure 1-12. Two Conductor Transmission Line of characteristic impedance Z_c and terminated by a load of impedance Z_l [18]

For the transmission line of figure 1-12 , the solution of the second order ordinary differential wave equations 1.9 and 1.10 results in

$$V(x) = V_0^+ e^{-\gamma x} + V_0^- e^{\gamma x}, \tag{1.12}$$

$$I(x) = I_0^+ e^{-\gamma x} + I_0^- e^{\gamma x}, \tag{1.13}$$

where $V_0^+ e^{-\gamma x}$ and $I_0^+ e^{-\gamma x}$ are the forward propagating voltage and current waves, while $V_0^- e^{\gamma x}$ and $I_0^- e^{\gamma x}$ are the backward propagating voltage and current waves. The terms V_0^+, V_0^- , I_0^+, and I_0^- are complex constants depending on the terminal conditions at the two ends of the line. As a matter of fact, the current along the line can be written as a function of the voltage in the form of

$$I(x) = \frac{V_0^+}{Z_c} e^{-\gamma x} + \frac{V_0^-}{Z_c} e^{\gamma x}, \tag{1.14}$$

where Z_c is the characteristic impedance of the line. Specifically, Z_c is the limit towards which the input impedance of an infinitely long line tends to, i.e., a line on which a signal propagates without ever being reflected towards the entrance. So at any point x in this infinite line, the ratio of the voltage and current of a wave traveling along the line is its corresponding characteristic impedance given as follows:

$$Z_c = \frac{V(x)}{I(x)} = \sqrt{\frac{Z}{Y}} \quad [\Omega], \tag{1.15}$$

and for a lossless transmission line

$$Z_c = \sqrt{\frac{L}{C}}. \tag{1.16}$$

The existence of a reflected wave on a line can be explained by the presence of an impedance discontinuity along the line. This parameter is very important when studying

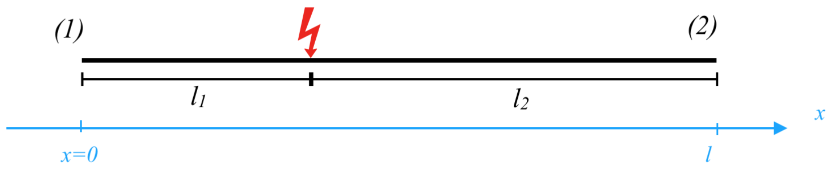

Figure 1-13. Two-port transmission line with characteristic impedance Z_c and faulty characteristic impedance Z_f at distance l_1 from the testing port *(1)*

fault detection and location methods. For instance, for a uniform transmission line of characteristic impedance Z_c ending by an impedance load Z_l, the incident wave will be reflected at the load. To quantify this reflection, a reflection coefficient is defined, which is given by the ratio of the forward propagating to backward propagating traveling waves at each point x as:

$$\Gamma(x) = \frac{V_{reflected}}{V_{incident}} = \frac{V_0^- e^{\gamma x}}{V_0^+ e^{-\gamma x}}, \tag{1.17}$$

and for a lossless transmission line, where $\alpha = 0$:

$$\Gamma(x) = \frac{V_0^-}{V_0^+} e^{j2\beta x} = \Gamma(0) e^{j2\beta x}. \tag{1.18}$$

Significantly, the reflection coefficient Γ_f at any discontinuity Z_f along the line is given by:

$$\Gamma_f = \frac{Z_f - Z_c}{Z_f + Z_c}. \tag{1.19}$$

It is therefore important to point out that faults are characterized by this reflection coefficient. Certainly, hard faults whether open or short circuits result in an absolute reflection coefficient equal to 1 ($|Z_f| = 1$), whereas any other kind of defect will result in a $|Z_f\ | < 1$. Consequently, the smaller Γ_f, softer the fault becomes. If the line is matched, $Z_c = Z_f$ and, consequently, Γ_f is zero.

Given the simple transmission line represented in the figure 1-13 where the fault is characterized by the different characteristic impedance $Z_f \neq Z_c$, the reflection coefficient at the discontinuity Z_f along the line is given by a ratio between the two characteristic impedances, according to the equation 1.19. If the difference between Z_c and Z_f is small, the reflection coefficient at the fault position will be small and, consequently, the time domain reflected wave will be small in amplitude. This is the reason why the time domain methods (included TDR) may struggle to see the fault location in case of soft fault. What it is interesting now is knowing the reflection coefficient at the testing ports, and according to the equation 1.18:

$$\Gamma(0) = \Gamma_1 = \Gamma_f e^{-j2\beta l_1} \tag{1.20}$$

$$\Gamma_2 = \Gamma_f e^{-j2\beta(l-l_1)} \tag{1.21}$$

where Γ_1 and Γ_2 are the reflection coefficients seen from the testing port 1 and 2, respectively, and l_1 and l_2 the distances between respective testing port and fault. The direction of propagation is chosen positive from the testing port 1 to the fault, and thus $x = 0$ corresponds to the testing port 1 and the fault is represented here, for sake of simplicity, as a discrete point fault.

However, the representation on 2-port-networks cannot be measured at high frequency, in particular above some hundreds of MHz. Different problems in fact can arise:

(1) the measurement of Z and Y parameters, according to the definition, needs the measurement of open circuit voltages and short-circuited currents, often on very small devices. It means that for high frequency it is impossible to directly choose the desired closure;

(2) in a microwave circuit, voltages and currents vary in a very rapid way: thus, it is not signicative to measure separately voltages and currents but it is better to measure parameters such power which depends on the linear combination between them and which not varies significantly along the line;

(3) for measurement of active circuits, short-circuit and open-circuit conditions often correspond to region of potential instability of the device, so they could not be measured.

In order to solve these problems, for high frequency networks there is the necessity to measure parameters related to the reflected and incident waves (voltage and current): the so-called *scattering parameters*.

1.2.2 Scattering Parameters Modeling of Wiring Networks

Scattering parameters (S-parameters) which usually form what is referred to the scattering matrix denoted as S, have been widely used in microwave applications where the scattering analysis has proved to be a very powerful tool that provides the system parameters of an N-port network [23, 24]. In the S-parameter approach, an electrical network is regarded as a "black box" containing various interconnected basic electrical circuit components or lumped elements such as resistors, capacitors, inductors and transistors, which

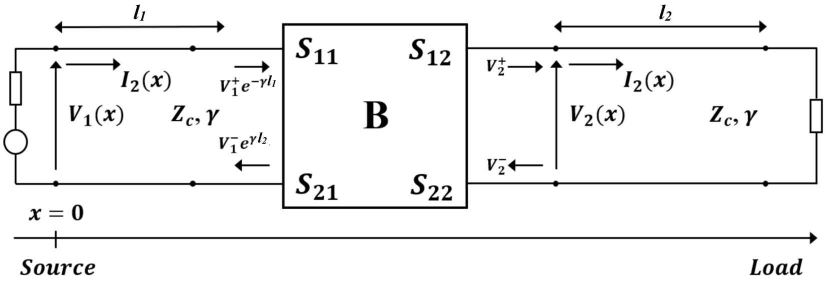

Figure 1-14. A two conductor transmission line containing a discontinuity represented as a block (B) whose length is null [18]

interacts with other circuits through ports. The network is characterized by a square S matrix of complex numbers, which can be used to calculate its response to signals applied to the ports. To better illustrate this approach, figure 1-14 is considered where the transmission lines are characterized by a characteristic impedance Z_c, each of length l_i, a propagation constant γ , and connecting a null length discontinuity considered as a black box B. In order to define the scattering parameters, first, the power waves a and b shall be introduced, representing the incident and reflected waves, respectively, as shown in figure 1-15. The power waves a and b, measured in $[W^{1/2}]$, are defined as follows:

$$a = \frac{V^+}{\sqrt{Z_c}} \tag{1.22}$$

$$b = \frac{V^-}{\sqrt{Z_c}} \tag{1.23}$$

Along a line the magnitudes of a and b are unchanged, but not he phase terms. Exploiting voltage and current it is possible to define the power waves as a sum or difference by voltage and current:

$$a = \frac{V + Z_c I}{2\sqrt{Z_c}} \tag{1.24}$$

$$b = \frac{V - Z_c I}{2\sqrt{Z_c}} \tag{1.25}$$

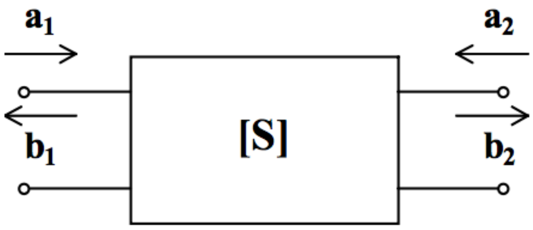

Figure 1-15. Power waves representation in the 2-port network of figure 1-14

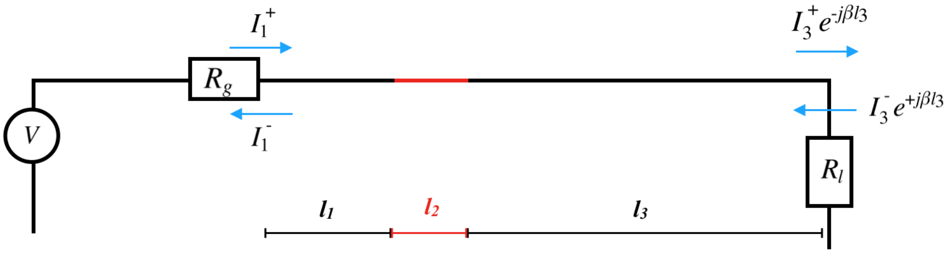

Figure 1-16. Circuit representation and modal currents in case of fault with length l_2

where it is evident that the relationship between a and b can be seen as a reflection coefficient Γ:

$$\Gamma = \frac{b}{a} = \frac{V - Z_c I}{V + Z_c I} \tag{1.26}$$

If the network is linear, it is possible to define the reflected power wave b as function of the incident power wave a, by means of the S parameters:

$$b = \begin{bmatrix} b_1 \\ b_2 \end{bmatrix} = \begin{bmatrix} S_{11} & S_{12} \\ S_{21} & S_{22} \end{bmatrix} \begin{bmatrix} a_1 \\ a_2 \end{bmatrix} \tag{1.27}$$

The measurement of the S matrix parameters is given by:

$$\begin{aligned} S_{11} &= \left.\frac{b_1}{a_1}\right|_{a_2=0} & S_{12} &= \left.\frac{b_1}{a_2}\right|_{a_1=0} \\ S_{21} &= \left.\frac{b_2}{a_1}\right|_{a_2=0} & S_{22} &= \left.\frac{b_2}{a_2}\right|_{a_1=0} \end{aligned} \tag{1.28}$$

where S_{ii} represent the reflection coefficient and S_{ij} the transmission coefficients.

In our case, the measurement of the S parameters is necessary in order to apply the time reversal fault location methods introduced in chapter 3. A Matlab model of the NUT has been built and the computation of the modal currents is done. The *PSpice* numerical tool has been adopted for the construction of the model, where a 1V voltage source and a matched load R_l are inserted in the network, as represented in figure 1-16. The model built is made up of three transmission lines, where the one in the middle represents the fault and its characteristic impedance is Z_f while the other two lines represent the healthy ones with characteristic impedance Z_c. The scattering matrix theory is considered, where S_{11} and S_{21} are computed exciting the network from the left side whereas S_{12} and S_{22} from the right side, starting from the computation of the modal currents. Consequently, the S

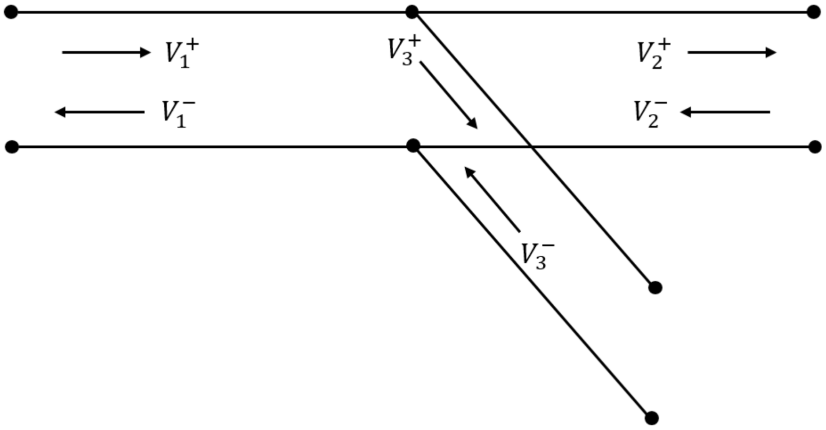

Figure 1-17. Y-branched structure

parameters are obtained and the whole scattering matrix is computed at each frequency:

$$\begin{aligned} S_{11} &= \frac{I_1^-}{I_1^+} & S_{12} &= \frac{I_1^-}{I_3^- e^{+j\beta l_3}} \\ S_{21} &= \frac{I_3^+ e^{-j\beta l_3}}{I_1^+} & S_{22} &= \frac{I_3^+}{I_3^- e^{-j2\beta l_3}} \end{aligned} \tag{1.29}$$

The reflection coefficient S_{11} corresponds to the reflection coefficient of the first testing port Γ_1, since:

$$S_{11} = \left.\frac{b_1}{a_1}\right|_{a_2=0} = \frac{I_1^-}{I_1^+} = \Gamma_1 \tag{1.30}$$

and thus

$$S_{11} = \Gamma_1 = \Gamma_f e^{-j2\beta l_1}. \tag{1.31}$$

Similarly, considering the testing port 2:

$$S_{22} = \Gamma_2 = \Gamma_f e^{-j2\beta(l-l_1)}, \tag{1.32}$$

where l is $l_1 + l_2 + l_3$.

For the case of a Y-branched structure, the voltage and current continuity laws must be verified at each junction along the line. For this purpose, considering figure 1-17:

$$V_1^+ + V_1^- = V_2^+ + V_2^- \tag{1.33}$$

and

$$V_1^+ + V_1^- = V_3^+ + V_3^-. \tag{1.34}$$

The current continuity condition at the junction, or Kirchhoff’ s nodal law, implies that the sum of the currents flowing into the junction is equal to the sum of currents flowing out of the junction. If expressed in terms of the voltage waves, the condition is:

$$\frac{V_1^+}{Z_c} - \frac{V_1^-}{Z_c} = \frac{V_2^+}{Z_c} - \frac{V_2^-}{Z_c} + \frac{V_3^+}{Z_c} - \frac{V_3^-}{Z_c}, \tag{1.35}$$

and thus the matrix S relationship can be obtained:

$$\begin{bmatrix} V_1^- \\ V_2^+ \\ V_3^+ \end{bmatrix} = S \begin{bmatrix} V_1^+ \\ V_2^- \\ V_3^- \end{bmatrix}. \tag{1.36}$$

Since the network under test to be studied is a very long cable, as presented in the next chapter, it is not possible to measure the transmission coefficients S_{ij} since there is impossibility of injecting signals in both the terminations due to the great distance between them. Therefore, the reflection coefficients only S_{ii} are taken into account and the analysis of the fault detection methods will include only the study of these parameters. As a matter of fact, the S-matrix formulation is the method adopted in our numerical simulations, performed throughout the multi-paradigm numerical computing software Matlab. Our simulation code was made up of two main parts.

The first, an RSIM simulation tool is adopted which was originally designed for the simulation of railway systems [25]. In fact, RSIM afforded an efficient design and implementation of different complex wiring networks, allowing the computation of both the modal voltages and currents at each position of the network. The importance of this simulation tool is its easy interface with Matlab which make the results observation easier. Besides, it is capable of returning only beneficial data necessary to compute the scattering matrices compared to heavier uninteresting data produced by other commercial tools as the full wave simulators.

As for the second part, it is based on the transmission line theory which allowed computing the characteristic impedance, propagation constant and modal currents (adopted for the scattering parameters computation) at any point along the branches composing the studied networks, which in turn permitted calculating the corresponding scattering matrix S. The electrical parameters of the lines are obtained by considering the real values of the NUT, in our case the MV power cable.

1.3 Content of Work

The principal purpose of the work is to evaluate and apply an innovative time reversal based techniques for soft fault location in quite long power cables, also in presence of losses. In fact, the most common fault location technique adopted nowadays is the time domain reflectometry (TDR) technique, and despite shows good results, several limitations arise above all when losses are introduced. Port MUSIC is a particular version of TR-MUSIC, a time reversal based method, which is theoretically introduced in this work and compared in its performances with TDR.

In this chapter an introduction on electrical cables, types of wiring faults and reflectometry technique is presented, together with a theory background on transmission lines in order to fully understand the next chapters of the work.

In chapter 2, the structure and the parameters of the NUT considered in the work are discussed. In particular, a medium voltage power cable is studied and an interesting analysis of its losses in frequency is carried out. This last part will be very useful when losses are introduced in the line.

The time reversal technique is introduced in chapter 3 and different methodologies studied. Firstly, DORT is considered but due to some limitations TR-MUSIC is then evaluated in its different versions. After a deep analysis on them, the so-called Port MUSIC technique shows great advantages in fault location than other methods and a comparison in its performances with TDR is carried out starting from chapter 4.

Chapter 4 adopts a single lossless line as NUT, where an interesting study on precision and accuracy estimation of both the methods is done. Spatial resolution and noise robustness are evaluated also through a metrological analysis with Monte Carlo simulations.

In chapter 5 losses are introduced and all the limitations of TDR arise. Performances of Port MUSIC in such a condition are studied with also experimental validations with VNA.

Finally, in chapter 6 a Y-branched structure is considered as NUT and the effect of the junction investigated in both the methods. The *baselining concept* here introduced and well explained is fundamental.

Conclusions and perspectives are then summed up for future possible developments.

Chapter 2

Power Cable and Analysis of Losses

In this chapter, the medium voltage power cable is introduced in its structure and characteristics, since it is adopted as NUT in our numerical simulations. Its electrical and dimensional parameters are analyzed in frequency, both in lossless and lossy cases. In particular, the analysis of its losses is carried out with an interesting study of them in frequency which will result very useful in the next chapters. A mapping between them and fixed attenuation values is implemented in order to retrieve the maximum frequency for given attenuation values.

2.1 Cable Structure and Parameters

The comparison between different soft fault location techniques is studied on guided wave propagation. As first step a lossless transmission line is considered, where R and G are nil. Then, since it represents a realistic cable, all the effects that influence the cable parameters must be taken into account, included the presence of losses. The line simulates a medium voltage (12/20kV) power cable, typically used for energy distribution with a 10km length. This choice is given by the fact that EDF (Electricité de France) wanted to test the time reversal soft fault detection methods on these cables typically used in ducts, trays or directly burial for energy transmission (figure 2-1).

The MV cable is a coaxial cable made up of six main layers, as shown in figure 2-2, and listed below:

(1) *a plain circular compacted copper (or aluminum) conductor*, composed of many smaller diameter conductors in order to reduce the skin effect;

(2) *a conductor screen which is an extruded semi conductive compound.* In power cables, conducting carbon black (CB)-filled ethylene copolymers, such as ethylene-butyl acrylate, ethylene vinyl acetate and ethylene thy acrylate, are commonly used as a

Figure 2-1: Power cables tested in our numerical simulations, EDF Lab Les Renardières, Seine-et-Marne, France

semiconducting layer. In the cable we consider for our analysis, the semiconductive materials used are ethylene-butyl acrylate copolymers. Researches on semiconductive shields has been playing an important role in the development of electric power cables. Their important functions can be summed up:

(a) preventing partial discharge at the interfaces between the insulation and the conductor and between the insulation and the external shielding layer;

(b) moderating the electrical stress in the insulation layer by providing a uniform electric field with reduced potential gradient;

(c) providing protection during short-circuits against damages caused by heating of the conductor. It is known that the semi conductive layers can influence the loss tangent of power cables;

(3) *insulation layer*, generally composed by XLPE (cross linked polyethylene). XLPE is a semicrystalline polymer that has good electrical properties [26, 27], such as low dielectric constant, low dielectric loss and high breakdown strength, together with other desirable properties such as mechanical toughness and flexibility, good resistance to chemicals, easy processing and low costs [28]. The maximum operational temperature is around 90 ℃, the emergency temperature 130 ℃, and the short-circuit maximum temperature 250 ℃. An important advantage of XLPE as insulation for medium and high voltage cables is their low dielectric loss [29, 30, 31]. The dielectric loss factor is about one decimal power lower than that of paper in-

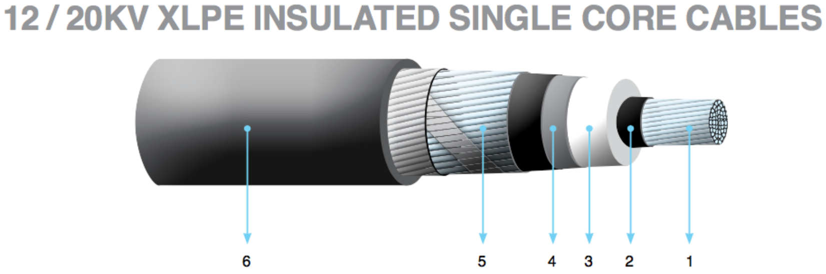

Figure 2-2: Power cable structure with the six different layers: (1) inner conductor, (2) first semiconductor, (3) insulation, (4) second semiconductor, (5) external conductor, (6) outer sheath [32]

sulated cables and about two decimal powers lower than that of PVC-insulated cables;

(4) *insulation screen*, composed by an external extruded semi conductive layer;

(5) *metallic screen*, composed by many twisted pair copper conductors which form a metallic layer. This layer is very important because it works as a screen in order to avoid external and internal interferences;

(6) *outer sheath*, its main function is the protection of the layers by external agents, like moisture, temperature, pressure and contacts. It is made up by PVC (PolyVinyl Chloride) which comes in two basic forms: rigid and flexible. The one used as protection of these cables is the latter one, obtained by the addition of plasticizers. It is used in this form in many applications to replace rubber.

The considered cross-section is $240mm$, since for the energy transmission, in the first kilometers (up to 10km) this kind of section is adopted, while $150mm$ of section after that. The internal conductor and the metallic crew are made up of copper. From the data sheet (furnished by EDF), the dimensions of the cable and its electrical parameters are given, as shown in the tables 2-1, 2-2 and 2-3 [32]: However, the electrical parameters are given at nominal frequency (50Hz) only. It is known that increasing the frequency some effects arise and modify the cable R, L, C and G parameters, in particular:

(1) *skin effect*, for which at high frequencies the current flows only in the external depth (skin depth) since the total flux is reduced. This is the reason why the resistance and the inductance of the internal and external conductors are reduced as frequency increases. In order to mitigate this effect, the two conductors are made up by many smaller conductors (litz wires);

(2) *proximity effect*, which refers to the influence of alternating current in one conductor on the current distribution in another, nearby conductor;

Table 2-1: General characteristics of the cable

Shape of the section	Circular
Insulation	XLPE
Nominal voltage	12/20kV
Cable length	10km
Insulation relative permittivity	2.5
Nominal tanδ	$5 \cdot 10^{-4}$
Maximum tanδ	$40 \cdot 10^{-4}$
Copper permeability	$1.25 \cdot 10^{-6}$
Copper conductivity	$5.8 \cdot 10^{7}$
Nominal cable temperature	40 ℃
Maximum cable temperature	90 ℃
Maximum cable temperature, sc	250 ℃

Table 2-2: Dimensional characteristics of the cable

Section [mm^2]	Inner conductor diameter [mm]	Insulation diameter [mm]	Outer conductor diameter [mm]
150	14.3	26.5	33.6
240	18.4	30.6	37.9

Table 2-3: Electrical characteristics of the cable at 50Hz

Section [mm^2]	P.u. capacitance [μF/km]	P.u. inductance diameter [mH/km]	Resistance at 90 diameter [Ω/km]
150	0.24	0.35	0.159
240	0.29	0.33	0.098

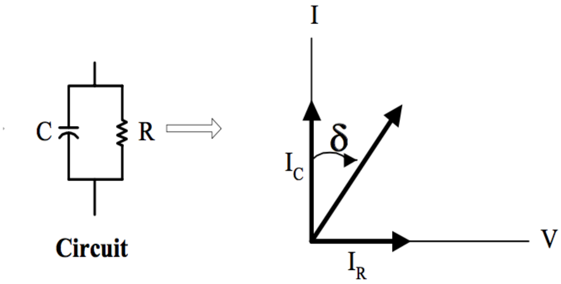

Figure 2-3: Voltage and current displacement in a cable and particular of δ angle [33]

(3) *loss tangent (or tanδ) variation*, a diagnostic method of testing cables to determine the quality of the cable insulation. This is done to try to predict the remaining life expectancy and in order to prioritize cable replacement and/or injection. It is also useful for determining what other tests may be worthwhile. If the insulation of a cable is free from defects, like water trees, electrical trees, moisture and air pockets, etc., the cable approaches the properties of a perfect capacitor. In this case, the voltage and current are phase shifted 90 degrees and the current through the insulation is capacitive. If there are impurities in the insulation, like those mentioned above, the resistance of the insulation decreases, resulting in an increase in resistive current through the insulation, as shown in figure 2-3. The current and voltage will no longer be shifted 90 degrees but something less than 90 degrees. The extent to which the phase shift is less than 90 degrees is indicative of the level of insulation contamination, and this "loss angle" is measured and analyzed. Tanδ is not constant in frequency but it varies, according to different processes, as the presence of semiconductive layers which increases its value in frequency due to its additional series resistance (figure 2-4); in particular, the determination of tanδ is related to the permittivity and conductivity of the insulation material, given by:

$$tan\delta = \frac{\varepsilon''}{\varepsilon'}, \tag{2.1}$$

where,

$$\varepsilon' = \varepsilon \qquad\qquad \varepsilon'' = \frac{\sigma}{\omega}, \tag{2.2}$$

in which ε' and ε'' are the real and the imaginary part of the complex permittivity of XLPE and σ its conductivity [111].

In case of lossless line R and G are nil and only L and C are present in the cable. Knowing the value of L and C at nominal frequency, their values at different frequencies can be computed and their behavior in frequency analyzed.

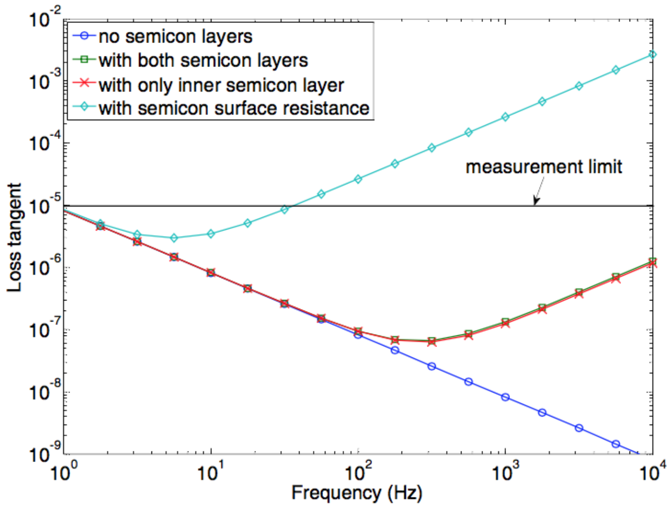

Figure 2-4: Behavior of tanδ frequency in presence of semiconductor layers in a cable [34]

2.2 Lossless Line

Considering figure 1-11, if the transmission line is lossless only L and C are present in the line. In this section, the equations describing their behavior in frequency are presented.

2.2.1 Inductance Estimation

At low frequencies the current flows uniformly all over the section. Thus, considering the figure 2-5 the concatenated magnetic flux integration is made from 0 to the radius a, for the internal conductor, and from b to c for the external conductor. Increasing the frequency, current starts flowing on the skin of the conductor section which is more and more smaller as frequency increases. This conductor section through which current flows is called *skin depth* δ and depends on frequency, copper permeability μ and conductivity

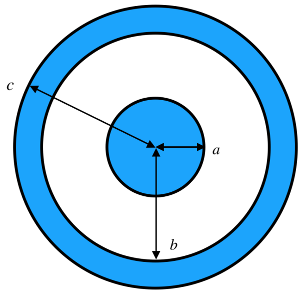

Figure 2-5: Cross-section of the coaxial cable, where the conductors are represented in blue and the insulation in white

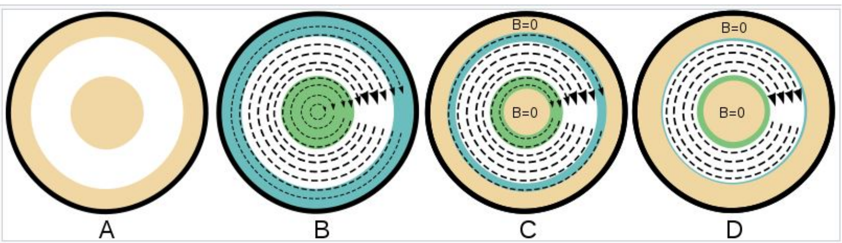

Figure 2-6: Current flowing increasing the frequency

σ, given by:

$$\delta = \frac{1}{\sqrt{\mu \pi \sigma f}}, \tag{2.3}$$

At higher frequencies, the integration is made from a-δ to a for the internal conductor and from b to b+δ for the external conductor. When the skin depth is very low, the values L_{int} and L_{ext} can be neglected and just the inductance between the two conductors (which is constant) is considered as result. Consequently, the total inductance L of a coaxial cable decreases in frequency, as shown in figure 2-6. The internal inductances of the cable can be computed using the Bessel functions and they result as:

$$L_{int} = \frac{1}{2\pi a}\sqrt{\frac{\mu}{2\omega\sigma}}, \tag{2.4}$$

$$L_{XLPE} = \frac{\mu}{2\pi}\ln\frac{b}{a}, \tag{2.5}$$

$$L_{ext} = \frac{1}{2\pi b}\sqrt{\frac{\mu}{2\omega\sigma}}, \tag{2.6}$$

where L_{int}, L_{XLPE} and L_{ext} represent the inductance of the inner conductor, insulation and outer conductor, respectively. The frequency at which L_{int} and L_{ext} can be neglected is around 1MHz, value from which a $> 2\delta$.

2.2.2 Capacitance Estimation

The capacitance of a coaxial cable can be considered constant for a wide range of frequencies. In fact, it depends only on the real permittivity ε' which is constant for frequencies up to 1GHz, at different temperatures, as shown in figure 2-7. Since in our simulations the frequency range of the cable is lower than 1GHz, C can be considered constant. From the mathematical point of view, C is given by:

$$C = \frac{2\pi\varepsilon_0\varepsilon_r}{\ln\frac{b}{a}} = \frac{2\pi\varepsilon}{\ln\frac{b}{a}} = \frac{2\pi\varepsilon'}{\ln\frac{b}{a}}. \tag{2.7}$$

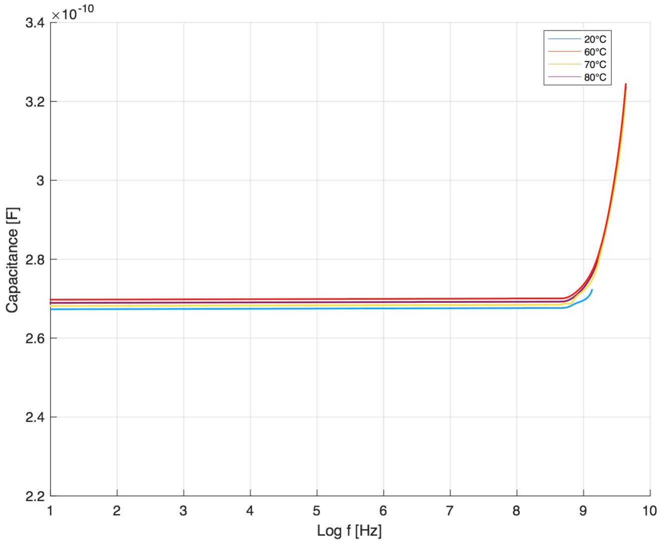

Figure 2-7: Capacitance in function of frequency at different temperatures [35]

2.3 Lossy Line

If losses are present in the transmission line, also R and G are included. In this section, the general estimation of these parameters for a coaxial cable is presented. After that, the analysis of losses introduced by R and G for the considered NUT is carried out, both series R/L and shunt admittances G/C.

2.3.1 Resistance Estimation

As frequency increases resistance changes. Skin effect in fact reduces the section in which the current flows and at high frequencies the section (*skin depth*) is very thin. Since the section decreases, the resistance increases [36]. In a coaxial cable the value of resistance in frequency is related to the surface resistance, given by:

$$R_s = \sqrt{\frac{\omega\mu}{2\sigma}}, \tag{2.8}$$

and the total resistance is

$$R = \frac{R_s}{2\pi a} + \frac{R_s}{2\pi b}, \tag{2.9}$$

obtained applying the Bessel functions, where μ and σ always represent the permeability and conductivity of copper. As result, the resistance increases in frequency as $\sqrt{f}$.

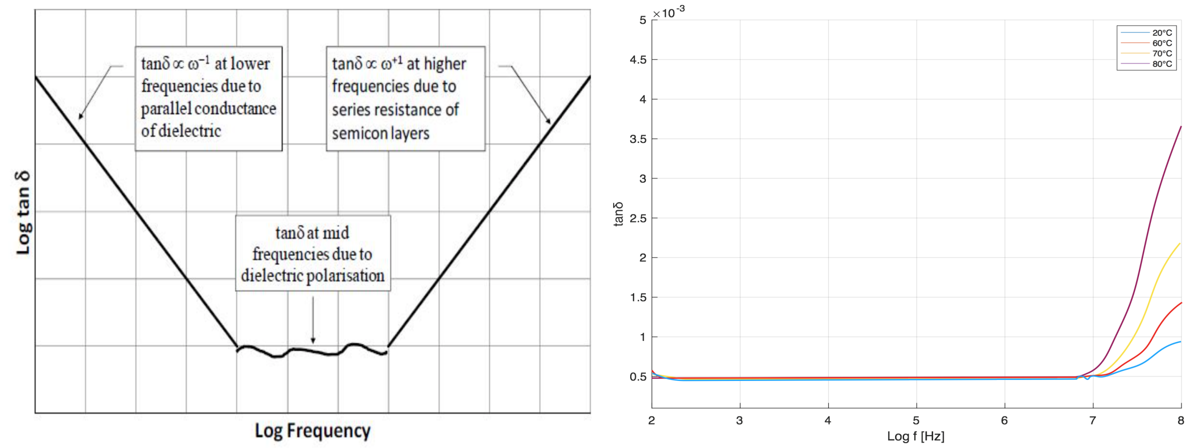

(a) *Generic dielectric behavior* (b) *XLPE tanδ at different temperatures*

Figure 2-8. Tanδ behavior in frequency [35]

2.3.2 Conductance Estimation

The conductance G is the electrical parameter responsible of the dielectric losses. These losses can be divided into two categories: *polarization losses*, due to the molecular resonances of the dielectric material, and *conduction losses*, due to the conductivity σ of the dielectric material [37, 38, 33, 34]. The conductance is related to $tan\delta$ previously introduced. In particular,

$$G = \frac{2\pi\sigma}{\ln\frac{b}{a}}, \tag{2.10}$$

and dividing by ωC,

$$\frac{G}{\omega C} = \frac{\sigma}{\omega\varepsilon} = tan\delta. \tag{2.11}$$

XLPE is commonly used in power cables above all for the very low tanδ and its variation in frequency very slow. In fact, for XLPE tanδ can be considered constant for a very wide range of frequency, up to 10MHz [35]. As shown in figure 2-8, where different temperatures are considered, at 40 °Ctanδ is constant up to 10MHz and its value is around $5{\cdot}10^{-4}$, while its maximum value (the worst value in case of lossy fault) is $40{\cdot}10^{-4}$, as shown in the table 2-1. Therefore, since C is constant in frequency, G increases linearly. The values of the electrical parameters in frequency of our specified NUT have been estimated throguh the equations introduces, and are shown in table 2-4. From these values it is possible to derive the values of series (R/L) and shunt admittance (G/C) losses of the cable at different frequencies, as shown in table 2-5.

Starting from these values, an analysis of cable's losses in frequency can be carried out.

Table 2-4: Electrical characteristics of the cable at different frequencies

Frequency [Hz]	R [Ω/m]	L [H/m]	C [F/m]	G [S/m]
50	$5.43 \cdot 10^{-5}$	$2.61 \cdot 10^{-7}$	$0.273 \cdot 10^{-9}$	$4.29 \cdot 10^{-11}$
10^4	$2.4 \cdot 10^{-3}$	$1.018 \cdot 10^{-7}$	$0.273 \cdot 10^{-9}$	$8.59 \cdot 10^{-8}$
10^5	$7.7 \cdot 10^{-3}$	$1.015 \cdot 10^{-7}$	$0.273 \cdot 10^{-9}$	$8.59 \cdot 10^{-7}$
10^6	$2.4 \cdot 10^{-2}$	$1.013 \cdot 10^{-7}$	$0.273 \cdot 10^{-9}$	$8.59 \cdot 10^{-6}$
10^7	$7.7 \cdot 10^{-2}$	$1.012 \cdot 10^{-7}$	$0.273 \cdot 10^{-9}$	$8.59 \cdot 10^{-5}$
10^8	0.24	$1.012 \cdot 10^{-7}$	$0.273 \cdot 10^{-9}$	$8.59 \cdot 10^{-4}$
10^9	0.77	$1.012 \cdot 10^{-7}$	$0.273 \cdot 10^{-9}$	$8.59 \cdot 10^{-3}$

Table 2-5: Series (R/L) and shunt admittance (G/C) losses at different frequencies

Frequency [Hz]	R/L	G/C
50	207	0.0314
10^4	$6.8 \cdot 10^3$	6.28
10^5	$2.31 \cdot 10^4$	62.8
10^6	$7.49 \cdot 10^4$	628
10^7	$2.39 \cdot 10^5$	$6.28 \cdot 10^3$
10^8	$7.57 \cdot 10^5$	$6.28 \cdot 10^4$
10^9	$2.39 \cdot 10^6$	$6.28 \cdot 10^5$

2.4 Analysis of Losses

Known the values of losses for the studied cable at different frequencies, it is possible to relate them with the attenuation, and from the derived relationship find out the maximum frequency associated to fixed attenuation values. In fact, in case of losses, attenuation and dispersion are introduced and may distort the signal response, both in amplitude and phase. In such cases, limitations in frequency derive from the attenuation presence and it is not possible to choose any arbitrarily bandwidth, but a maximum frequency shall be computed in order to have low attenuation values. In other words, higher the frequency, more attenuation is: if large bandwidth are taken into account, large attenuation values influence the signal amplitude and it becomes very hard to find out the exact fault position [39]. Considering a 2-port transmission line, as shown in figure 2-9, an arbitrarily 20dB attenuation value at the testing port (1) is chosen, and thus 10dB at the fault position, represented by the red arrow. Starting from equation 1.11, attenuation and

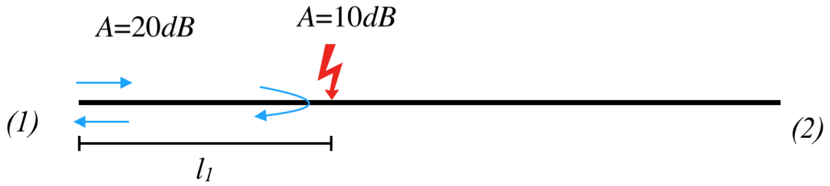

Figure 2-9: Lossy transmission line with arbitrarily chosen 10dB of attenuation at the fault position

phase constants can be exploited as function of losses R/L and G/C:

$$\alpha = \omega \frac{LG + RC}{2\beta}, \tag{2.12}$$

$$\beta = \frac{1}{\sqrt{2}}[-RG + \omega^2 LC + \sqrt{(R^2 + \omega^2 L^2)(G^2 + \omega^2 C^2)}]^{1/2}. \tag{2.13}$$

At high frequencies:

$$\omega^2 L^2 >> R^2 \qquad \omega^2 C^2 >> G^2, \tag{2.14}$$

verified for frequencies around 750kHz÷1MHz. Then, after some mathematical operations:

$$\alpha = \frac{\frac{R}{L} + \frac{G}{C}}{2} \sqrt{LC} = \frac{\frac{R}{L} + \frac{G}{C}}{2} \cdot \frac{1}{v}, \tag{2.15}$$

$$\beta = \omega \sqrt{LC} = \frac{\omega}{v}, \tag{2.16}$$

with the propagation velocity constant at $1.9044 \cdot 10^8$ $[m/s]$, corresponding to the high frequency velocity. From equations 2.15 and 2.16 the attenuation constant α depends on losses and is independent on frequency at high frequencies. Besides, α is related to the attenuation A, measured in dB:

$$\alpha = \frac{\ln 10^{\frac{A}{20}}}{l_1}, \tag{2.17}$$

with l_1 the distance between the testing port and the fault position. Considering the case of A=*10dB*:

$$\alpha = \frac{\ln \sqrt{10}}{l_1} = \frac{1.1513}{l_1}, \tag{2.18}$$

and exploiting losses:

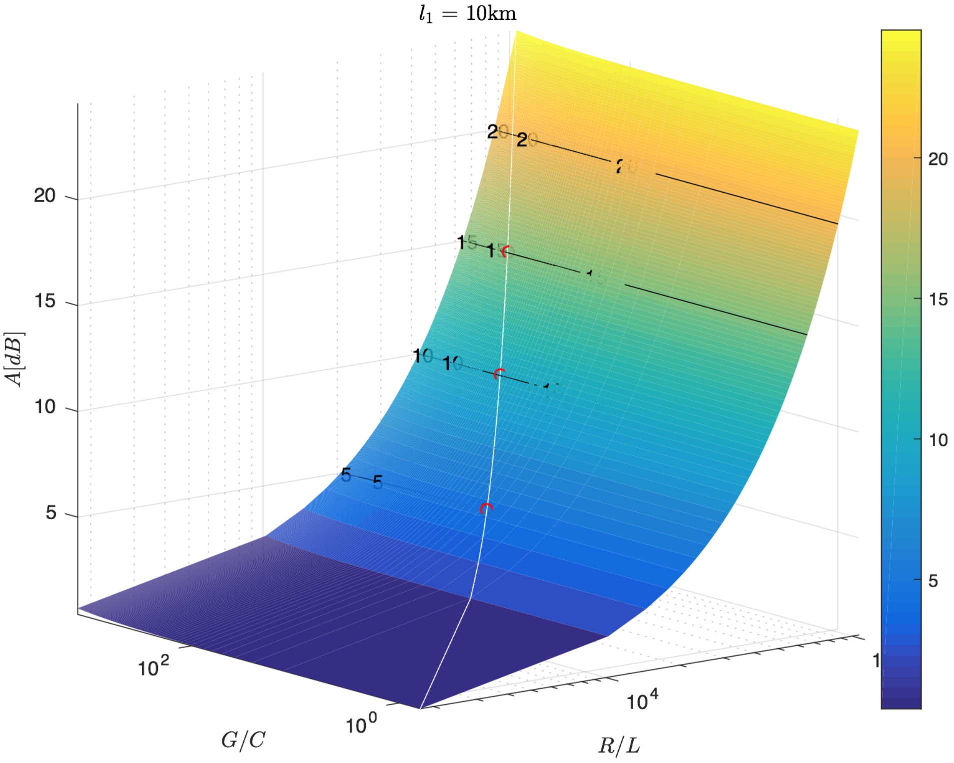

Figure 2-10: Three dimensional mapping of the cable losses and attenuation for l_1=10km

$$\frac{R}{L}(f) + \frac{G}{C}(f) = 2\alpha v = \frac{4.38 \cdot 10^8}{l_1}. \tag{2.19}$$

According to equation 2.19, it is possible to plot in a three-dimensional way the losses and the attenuation A. In fact, these three parameters depend on frequency and fixing different attenuation values a mapping of losses is carried out. In figure 2-10 the case l_1=10km is figured out, where the white line corresponds to the "*losses curve* " of the cable, the black lines different contour values of fixed attenuations and the red points the intersection between the curves. The region of different values of attenuation is better shown with a colormap on the right. Considering the 10dB contour of attenuation, the corresponding losses are found and, consequently, the associated *maximum frequency*, shown in figure 2-11.

Once the maximum frequency is estimated, the spatial resolution can be derived and applied for the time-domain methods. Particularly, it is given by:

$$\Delta s = v \cdot \Delta t = \frac{v}{f_{max}}. \tag{2.20}$$

Different fault positions are considered and mapped, over a 10km line length, and the correspondent *maximum frequency* and *spatial resolution* are found out.

The table 2-6 and the figure 2-12 show the limitations of the time-domain techniques

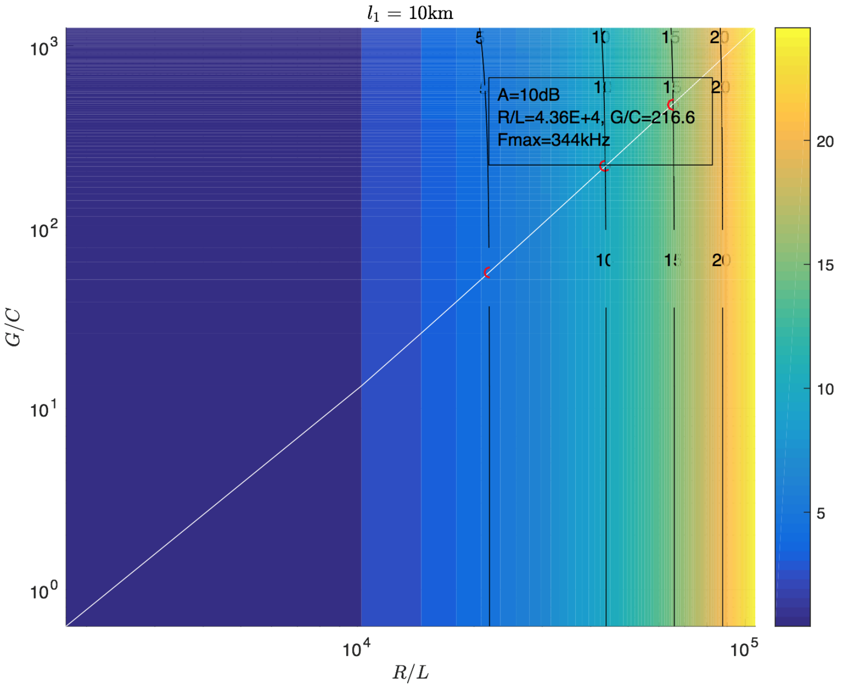

Figure 2-11: Mapping of the cable losses with 10dB of attenuation and correspondent frequency

Table 2-6: Frequency and spatial resolution estimation for different fault positions over a 10km transmission line length with a fixed 10dB attenuation value

l_1 $[m]$	R/L	G/C	Frequency $[Hz]$	Spatial Resolution $[m]$	% Spatial Resolution
10000	$4.36{\cdot}10^4$	216.6	$3.44{\cdot}10^5$	553.6	5.53
7500	$5.8{\cdot}10^4$	379.7	$6.04{\cdot}10^5$	315.3	3.15
5000	$8.68{\cdot}10^4$	841.4	$1.34{\cdot}10^6$	142.1	1.42
2500	$1.72{\cdot}10^5$	$3.27{\cdot}10^3$	$5.21{\cdot}10^6$	36.6	0.36
1000	$4.19{\cdot}10^5$	$1.93{\cdot}10^4$	$3.07{\cdot}10^7$	6.2	0.062
100	$3.24{\cdot}10^6$	$1.15{\cdot}10^6$	$1.82{\cdot}10^9$	0.1	0.001

about the precision on fault detection. More the fault is far from the testing port, less the frequency is, and consequently worse spatial resolution are obtained. Therefore, in order to reduce the attenuation in lossy cases, a limited maximum frequency must be considered and according to the equation 2.20 the time domain methods (as TDR) show bad resolutions.

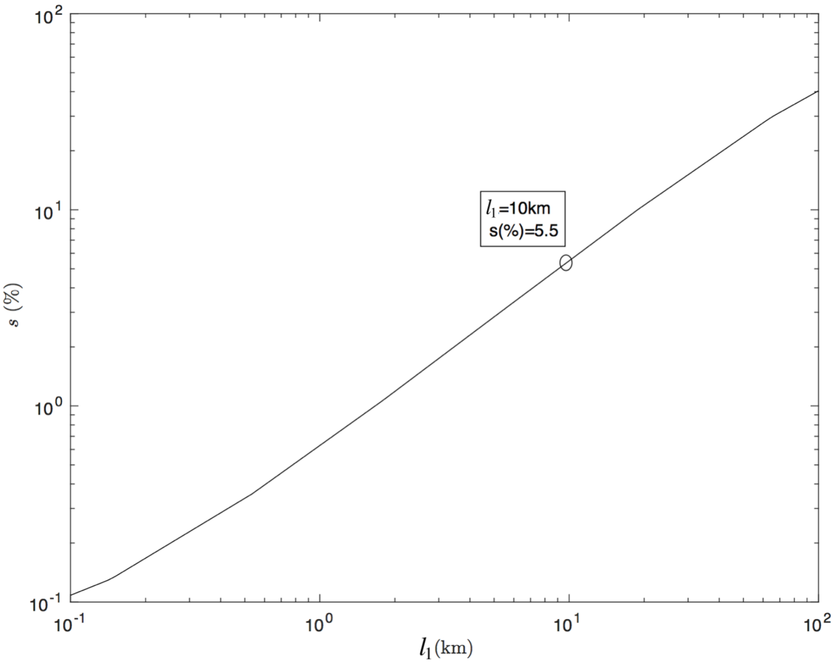

Figure 2-12: Spatial resolution (%) as function of line length

2.5 Summary

In this chapter the structure of the studied NUT is analyzed and its electrical parameters in function of frequency are estimated. All the effects influencing the electrical parameters are presented and considered in the study. Accordingly, knowing the cable parameters, the analysis of losses is carried out and a mapping at given attenuation values is figured out. In particular, fixing the attenuation at *10dB* at the fault position, the maximum frequency in presence of losses is estimated and, consequently, the spatial resolution. As a result, the time domain method, included TDR, show several limitations in presence of losses, since for reducing the attenuation value a limited maximum frequency must be taken into account.

Therefore, different techniques for soft fault location able to improve these limitations shown in TDR are needed. In the next chapter, interesting fault location methods based on time reversal are introduced and illustrated: DORT (Décomposition de l’ Opérateur de Retournement Temporel) and TR-MUSIC (Time Reversal - MUltiple SIgnal Classification).

Chapter 3

Time Reversal: DORT and TR-MUSIC analysis

The main principle of *time reversal* is the focusing of the waves back towards the source of its origin generating waves behaving as if they were propagating backward in time. The availability of the scattering matrix S of the wiring network represents the main difference with respect to TDR, in which the analysis of reflected waves in time-domain allows the knowledge of the fault position.

In this chapter, two of the most common TR methodologies, ‘‘Decomposition of the Time Reversal Operator” (DORT), and ‘‘TR-MUltiple SIgnal Classification” (TR-MUSIC), will be presented, their wide range of applications and the respective advantages and disadvantages. Namely, they share the same foundations related to the decomposition of S but follow two different ways to translate it into the fault position. DORT adopts a subspace approach in defining signals that, once fed into a numerical model of the network, focuses back to the fault position in time-domain. Thus, most of the limitations of any other time-domain method, included the need for large bandwidth to create spatial resolution, still occur. On the contrary, TR-MUSIC, operates on a different subspace approach based on the Green function of the network; the phase patterns provided by the Green function are the mean of identifying positions.

Main concepts and background of time reversal are presented in the first part of the chapter, and then the way of working of DORT and TR-MUSIC are illustrated, both in open media and in guided wave propagation.

3.1 Background and Motivation

A gunshot is fired at night in an area with several tall buildings. Soon afterward a location is detected and displayed on screen at the emergency department of the nearest

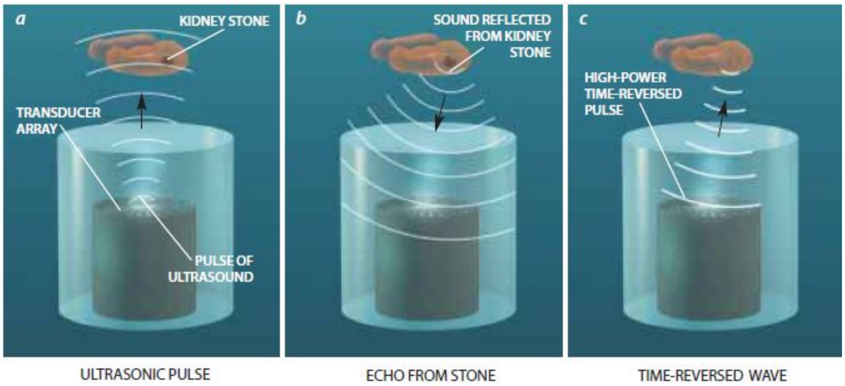

Figure 3-1: Example of TR application for the kidney stones detection [48]

hospital and also in a patrol car near by. As a matter of fact, the sound from the gunshot is recognized by microphones placed on the surrounding buildings and in a computer simulation projected back to the source. This is referred to as *time reversal*; it is a method that adopts backward propagation of waves to focus wave energy onto a specific location in space and time. The first experiments performing TR methods dates back in 1965, when Parvulescu and Clay [40] time reversed the received signal and broadcast it from the source to the receiver again, proving that the matched signal technique was able to focus the arrival of the waves in space. Many studies and researches in this field show improvements and more and more better results until the advances in microelectronics and array technologies during the beginning of the 1990s, which led to the development of the acoustic Time Reversal Mirror (TRM) by Fink and collaborators at the University of Paris VII, Laboratoire Ondes et Acoustique (LOA) [41, 42, 43, 44]. The list of the possible applications of TR methodologies is very wide: it goes from automatic processes [45, 46] to ultrasonic focusing, from avionic and space to undersea applications, from geology for seismic imaging [47] to medical problems as the detection of breast cancer or kidney stones [48], as shown in figure 3-1.

Thus, time reversal is a process of recording the signal from a remote source, time-reversing and back-propagating it to retro-focus around the source [49]. Consequently, the received signals are time reversed and re-broadcast into the media, experiencing similar multipaths and scattering as those they have undergone in the forward direction. They finally focus on the position of the initial source, a process similar in concept to playing a movie backwards.

3.2 Time Reversal in Open Media

Time reversal is firstly introduced in open media and, in order to better understand its functional concepts, an experiment in the acoustic field is presented. In particular, a

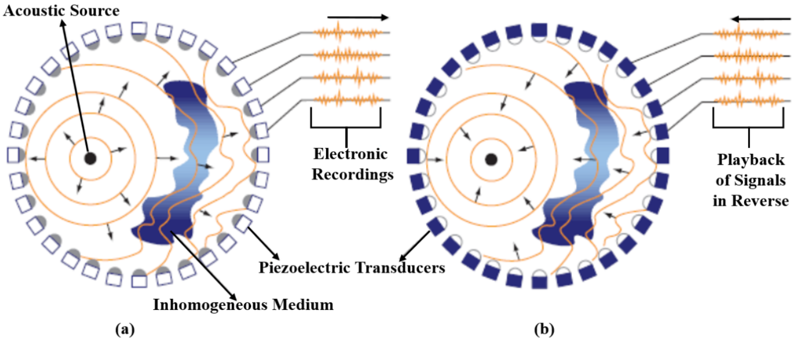

Figure 3-2: Acoustic TR of the TR cavity, where both the recording (a) and time reversal steps (b) are represented [3]

source radiates a short pulse which is transmitted into the inhomogeneous medium (figure 3-2(a)). Attenuation and distortion are generated due to the presence of discontinuities and inhomogeneities in the medium. At the end, they encounter a set of transducers surrounding the source, better known as the *TR cavity*, where each of them records the signal [49]. This is the first step of the procedure, known as the *recording step*. In the second step, called *time reversal step* and shown in figure 3-2(b), each transducer plays back its sound signal in reverse. Re-creation of the initial wave occurs but traveling backward and refocusing on the original source point. Practically, a closed TR cavity is difficult to be realized and a need of a new operational way is fundamental. This is the reason why the Time Reversal Mirror (TRM) has been introduced. It is made up by several transducers, each one having its own electronics. As in the TR cavity case, the transducers act both in passive (*echo*) and active (*transmit*) modes, since they record and re-transmit the time reversed signal. The TRM operational mode consists in three main steps, as shown in figure 3-3: in (a) the *transmitting step* is presented where the TRM emits pulses into the inhomogeneous medium towards the target. The scatterer will create a backscattered field which will be recorded by the TRM as shown in step (b), better known as the *recording step*. In the final step (c), a time reversed field will be re-transmitted into the medium leading to a focusing on the position of the target.

Based on the time reversal concepts, two methods are presented in this work starting from the next section, DORT and TR-MUSIC. In this chapter, the concepts and the theory derivation are introduced, both in open media and transmission line propagation, and their advantages and limitations are shown, in order to make a reliable comparison with TDR, presented in the next chapters. Particularly, they are known as ‘‘subspace” TR imaging techniques since based on subspace analysis of the scattering matrix. In fact, both the methods derive from the singular value decomposition (SVD) of the faulty scattering matrix of the line and differ from the adopted matrix subspace: the *signal subspace* $\mathcal{S}$ for DORT and the *noise subspace* $\mathcal{N}$ for MUSIC.

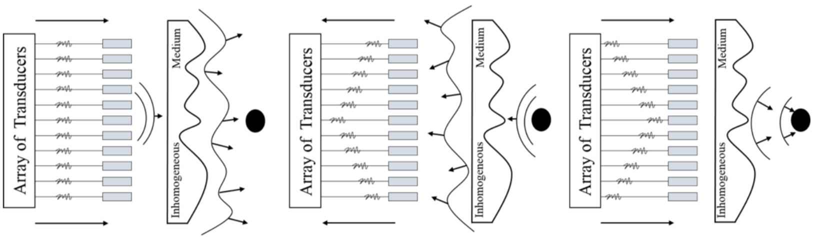

(a) (b) (c)

Figure 3-3: The TR process using the TRM where the three steps are presented in presence of an inhomogeneous medium [3]

3.2.1 The DORT Method

As introduced in the previous section, DORT consists in a subspace analysis deriving from the the scattering matrix decomposition. Based on the theoretical analysis of time reversal mirrors, it relies on the matrix formalism used to describe a transmit-receive process [50, 51, 52]. Given an array of L transducers as the one shown in figure 3-3, the general idea is to express the received signals as a function of the transmitted ones. First, the inter-element impulse response k_{lm}(t) is introduced in order to better understand the functional principle of DORT. In particular, k_{lm}(t) is the signal applied from the element m and received to the element l after a temporal Delta function. According to the reciprocity theorem known for propagation in inhomogeneous medium, the inter-element impulse response from m to l is equal to the inter-element impulse response from l to m, so that k_{lm}(t) is equal to k_{ml}(t) [53]. The repetition of the process for each pair *(m, l)* of transmitting and receiving elements leads, at a given frequency, to the transfer matrix $S(\omega)$, with dimensions [L×L]. In general, if the medium contains N pointlike scatterers, S can be written as the product of three matrices:

$$S = U \Lambda V^{\dagger}, \tag{3.1}$$

where U is the matrix describing the transmission and propagation from the L transducers to the N scatterers, Λ is the diagonal matrix describing the reflectivities of the scatterers on the S matrix, and V is a transpose conjugate matrix which describes the back-propagation process from the N scatterers towards the L transducers. As a matter of fact, the formulation represented in equation 3.1 is equivalent to the singular value decomposition of the scattering matrix, where Λ is a real diagonal matrix of the singular values while U and V are unitary matrices whose columns are the left-singular vectors and right-singular vectors of S, respectively [54]. What it is very important in the DORT procedure is the Time Reversal Operator K and the decomposition of it, as the acronym DORT suggests, and it is given by:

$$K = SS^{\dagger}. \tag{3.2}$$

According to the reciprocity theorem, the transfer matrix S(ω) is symmetric and therefore K is Hermitian. Since K is Hermitian, for the Hermitian matrix properties, it can be diagonalized. The decomposition on eigenvalues and eigenvectors is therefore accomplished. In fact, the SVD of S is equivalent to the eigenvalue decomposition of K, where

$$K = V\Lambda^2 V^{\dagger}, \tag{3.3}$$

with Λ^2 being a real diagonal matrix of the eigenvalues, and V being the eigenvectors matrix. In particular, the eigenvector matrix V can be divided into a signal space $\mathcal{S}$ and a noise space $\mathcal{N}$. $\mathcal{S}$ is formed by the eigenvectors with nonzero eigenvalues whereas $\mathcal{N}$ is formed by the remaining eigenvectors having almost zero eigenvalues. Consequently, $\mathcal{S} = span\{v_i : \lambda_i^2 > 0\}$, while $\mathcal{N} = span\{v_i : \lambda_i^2 \approx 0\}$, where v_i are columns of the unitary matrix V, and written in a matricial form, considering *L=2*:

$$K = \left[\begin{array}{c|c} \underline{v}_1 & \underline{v}_2 \end{array} \right] \begin{bmatrix} \lambda_1^2 & 0 \\ 0 & \lambda_2^2 \end{bmatrix} \left[\begin{array}{c|c} \underline{v}_1^{\dagger} & \underline{v}_2^{\dagger} \end{array} \right] \tag{3.4}$$

If there is only one scatterer, only the first eigenvalue λ_1 is significant while λ_2 is close to zero. In general, the number of scatterers N is equal to the number of nonzero eigenvalues obtained through the SVD of the scattering matrix S. The eigenvectors associated to the significant eigenvalues represent the *signal subspace* $\mathcal{S}$, in this case $\underline{v}_1$, while the eigenvectors associated to the non-significant eigenvalues represent the *noise subspace* $\mathcal{N}$, in this case $\underline{v}_2$. It is important to note that in presence of multiple scatterers, the correspondent eigenvalues in the Λ^2 matrix are ordered by intensity, i.e., the eigenvalue λ_1 represents the strongest scatterer [55]. Consequently, in presence of a single scatterer the eigenvalue λ_1 is the only one different from zero. In the example of figure 3-4, the diagonalization of K results into two significant eigenvalues, denoted as λ_1 and λ_2 (with $\lambda_1 > \lambda_2$) corresponding to the two targets A and B, and *L-2* eigenvalues close to zero. So, focusing on the weaker target (B), the eigenvector $\underline{v}_2$ corresponding to λ_2 is propagated in space and time. The result is a wave focusing on the target B; a similar result is also obtained propagating the eigenvector $\underline{v}_1$ corresponding to λ_1 in order to focus on the target A [56, 57, 58]. With this example, one of the advantages of DORT is shown: in fact, selective focusing is achieved using the DORT method, and in presence of multiple scatterers it is possible to inject the correspondent eigenvectors and selectively focusing the attention on it. As a matter of fact, DORT works well in presence of multiple scatterers and is able to individually select them [59, 60, 61].

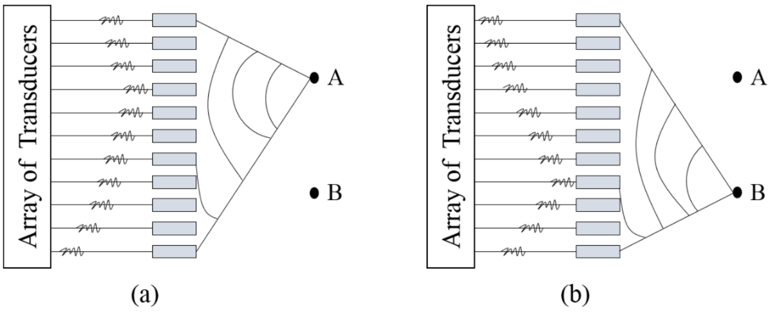

Figure 3-4: Selective focusing accomplished by DORT method in presence of two scatterers [3]

3.2.2 The TR-MUSIC Method

MUltiple SIgnal Classification (MUSIC) was first introduced by R. O. Schimdt in 1979 [16] as a method used to provide asymptotically unbiased estimates of a general set of multiple wavefronts arriving at an antenna array. For this reason, MUSIC is considered as a DOA estimation method, where DOA (Direction Of Arrival) denotes the direction from which a propagating wave arrives at a certain point. Many fields include the MUSIC method, especially radar, sonar, electronic surveillance and telecommunication applications. As DORT, it is born in open media applications and only recently has been adopted as fault detection method in wiring networks [62, 63]. The basic idea is equivalent to DORT, since also MUSIC derives from the SVD of the scattering matrix S or, equivalently, from the EVD of the TRO K. However, it is completely different with respect to DORT since it does not adopt the *signal subspace* $\mathcal{S}$ in the operational procedure but, on the contrary, the *noise subspace* $\mathcal{N}$, where $\mathcal{S} \perp \mathcal{N}$. This implies high spatial resolution results: as better shown and explained in section 3.4, considering the noise subspace instead of the signal subspace can bring many advantages in several applications, by studying accuracy and precision of the methods [64, 65]. These two orthogonal subspaces are used to construct a spectrum function, be got though by spectral peak search and detect DOA signals. In MUSIC this function is called *Pseudo-spectrum* $\Phi(x)$, able to find peaks at the position of the scatterer at any frequencies. In fact, one of the great advantages of MUSIC is that it is able to localize the target at single frequencies, adopting mono-chromatic waves. When the Pseudo-spectrum function tends to infinite, a peak is detected and it represents the scatterer position, at any arbitrarily chosen frequency. Now the question is: when the Pseudo-spectrum function tends to infinite and in which way does MUSIC operate?

MUSIC operates through a projection procedure, involving the noise subspace $\mathcal{N}$ and the *Green function g(x)* phase patterns, computed at any position x of the medium. Therefore, a certain number of discrete points in the space must be chosen and their Green functions calculated. A Green function is a complex mathematical tool which represents

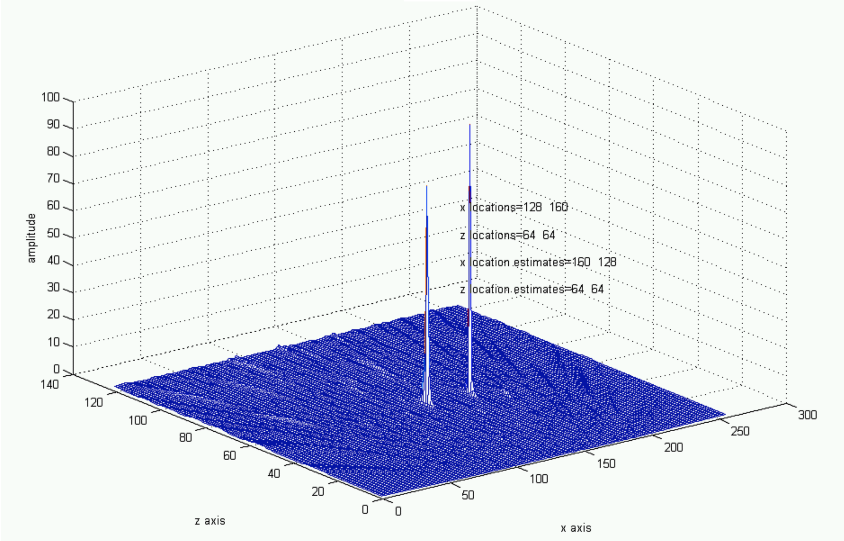

Figure 3-5: Mesh plot of the Pseudo-spectrum of scatterers present in an open medium

a wave varying both in time and space. In other words, it represents a propagating wave from a certain point to another one where only the phase pattern of the wave is taken into account [66, 67]. Going back to the functional procedure of MUSIC, the Pseudo-spectrum function $\Phi(x)$ can be represented as follows:

$$\Phi(x) = \frac{1}{\sum\limits_{\lambda_i^2 \approx 0}^{L-N} |<\underline{v}_i, \underline{g}(x)>|^2}, \tag{3.5}$$

where $\underline{v}_i$ represent the L-N orthogonal vectors to the signal subspace vectors, for the L-N eigenvalues equal to zero. Since $\mathcal{S} \perp \mathcal{N}$, it represents the noise subspace. Both $\underline{v}_i$ and $\underline{g}(x)$ are vectors since the Pseudo-spectrum function is computed at any frequency of the considered bandwidth. As shown in the equation 3.5, at the x position in which the projection between such vectors is zero, $\Phi(x)$ is maximum and at any frequency peaks are found. In order to clarify this point, the example in figure 3-5 is presented, where the Pseudo-spectrum is maximum in two points corresponding to the locations of two scatterers present in an open medium. As observed in this example, two *well-resolved* peaks are detected given by the projection procedure. This "*well-resolvedness*" result is obtained by the fact that MUSIC adopts the $\mathcal{N}$ subspace and allows the determination of singular points for detecting the scatterers [68, 69].

Generally speaking, it was shown that the MUSIC Pseudo-spectrum computed using the Green function as a steering vector yields accurate estimates of the target locations while achieving a sub-wavelength resolution. More importantly, this result pushed forward towards practical implementation for applications not limited to open media, but also in guided wave propagation represents by transmission lines [70, 71].

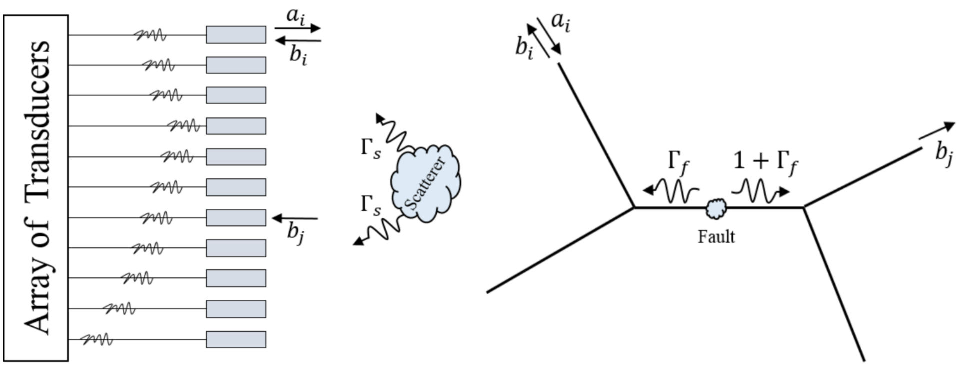

(a) *Open media* (b) *Wiring network*

Figure 3-6. DORT procedure [3]

3.3 DORT Method in Guided Wave Propagation

Conceptually, a fault in a wiring network is nothing else than a discontinuity. This simple observation implies that locating a fault in a transmission line is essentially the same problem as a scatterer in an open medium. A different approach to fault location has been adopted from the acoustics to the case of guided wave propagation along transmission lines and has shown to be efficient in locating a single soft fault. It is important to note that in our work the hypothesis of single soft fault is done and the line is matched at all the testing ports [72]. As a matter of fact, important differences exist in DORT between the open media and the guided wave propagation cases. First, in free space, a generated wave from an array of transducers is equally reflected in all directions of a point-like scatterer. The reflection coefficients are the same in all the considered directions and corresponds to the Γ_s of the scatterer; the target in this case acts as a secondary isotropic source. On the other hand, for the case of transmission lines, when a propagating wave encounters a fault, a reflected wave (in the opposite direction of propagation) and a transmitted wave (in the same direction of propagation) are generated; in particular, the first one is factorized by the reflection coefficient Γ_f of the fault while the transmitted one by $(1+\Gamma_f)$, and thus the reflection coefficients weighting the generated waves from the fault are not equal. To better understand the concept an example is shown in figure 3-6. Beside, while in open media the signal received at the *jth* port is only made up by the reflected wave generated from the scatterer, in transmission line the reflected and transmitted waves are intrinsically mixed up and different weights are included. This situation has no analogy in open media, making the use of the DORT method in guiding media different and more critical [73].

DORT is a time-domain based method which is able to synthesize signals aimed to focus at the fault position. It operates maximizing the energy at that position, when a

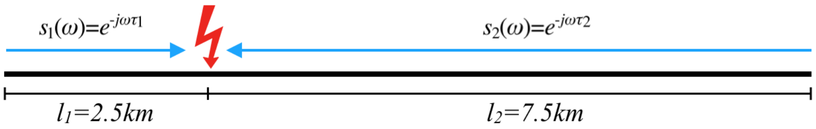

Figure 3-7: Frequency-domain signals focusing at the fault position in a 2-port transmission line

discontinuity in a transmission line occurs, and even in presence of low SNR values it can localize the fault precisely. Considering a 2-port transmission line with a single soft fault, the EVD is applied, where $\underline{v}_1$ represents the eigenvector associated to the "faulty" nonzero eigenvalue λ_1 and $\underline{v}_2$ the eigenvector associated to the "healthy" nil eigenvalue λ_2. As already introduced in section 3.2.1, DORT is an imaging method operating in the signal subspace and thus the eigenvector $\underline{v}_1$ is considered in the procedure. In particular, the components of such eigenvector are injected from the both ports of the transmission line, in time-domain, and they focus at the fault position maximizing the energy at that point [74]. Considering the 10km line in figure 3-7, the frequency-domain signals $s_1(\omega)$ and $s_2(\omega)$ are injected in the line and focus at the fault position, situated at 2.5km from the testing port (1). If the fault is a discrete point, it is known from the transmission line theory that the reflection coefficient of an injected wave is $\mathit{\Gamma}_f$ while the transmission coefficient is 1+$\mathit{\Gamma}_f$. In this case, the S_f matrix of the faulty line is given by:

$$S_f = \begin{bmatrix} \Gamma_f e^{-j2\omega\tau_1} & (1+\Gamma_f)e^{-j\omega(\tau_1+\tau_2)} \\ (1+\Gamma_f)e^{-j\omega(\tau_1+\tau_2)} & \Gamma_f e^{-j2\omega\tau_2} \end{bmatrix}. \tag{3.6}$$

Instead, if the the fault is not a discrete point but it has a finite line length, the transmission coefficient is different from 1+Γ_f. Considering the figure 3-8, the line has a fault given by an impedance discontinuity with length w, where the reflection coefficients seen by the fault Γ_0 and seen by the testing port (1) Γ_f are given by the following equations:

$$\Gamma_0 = \frac{Z_f - Z_c}{Z_f + Z_c}, \tag{3.7}$$

$$\Gamma_f = \Gamma_f(\Gamma_0). \tag{3.8}$$

In this case, the S_f matrix is given by:

$$S_f = \begin{bmatrix} \Gamma_f e^{-j2\omega\tau_1} & (1-\Gamma_f^2)e^{-j\omega(\tau_1+\tau_2)} \\ (1-\Gamma_f^2)e^{-j\omega(\tau_1+\tau_2)} & \Gamma_f e^{-j2\omega\tau_2} \end{bmatrix}. \tag{3.9}$$

Approximating the transmission coefficient magnitude term to 1, it is possible to neglect

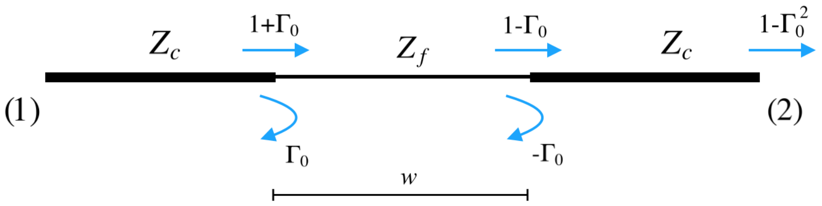

Figure 3-8: Reflection coefficients in a 2-port transmission line with a fault represented by a finite line length

it and consequently:

$$S_f = \begin{bmatrix} \Gamma_f e^{-j2\omega\tau_1} & e^{-j\omega(\tau_1+\tau_2)} \\ e^{-j\omega(\tau_1+\tau_2)} & \Gamma_f e^{-j2\omega\tau_2} \end{bmatrix}, \tag{3.10}$$

and normalizing the reflection terms,

$$S_f = \begin{bmatrix} e^{-j2\omega\tau_1} & e^{-j\omega(\tau_1+\tau_2)} \\ e^{-j\omega(\tau_1+\tau_2)} & e^{-j2\omega\tau_2} \end{bmatrix}. \tag{3.11}$$

Multiplying it by its transpose conjugate matrix $S_f^\dagger$, the TRO K is given by:

$$K = S_f S_f^\dagger = 2 \begin{bmatrix} 1 & e^{j\omega(\tau_2-\tau_1)} \\ e^{-j\omega(\tau_2-\tau_1)} & 1 \end{bmatrix}. \tag{3.12}$$

Applying the EVD to the matrix K, as in the equation 3.4, the eigenvector $\underline{v}_1$ is the one associated to faulty eigenvalue λ_1. After some mathematical operations, the vector $\underline{v}_1$ can be exploited in its two components,

$$\underline{v}_1 = \begin{bmatrix} e^{-j\omega\tau_1} \\ e^{-j\omega\tau_2} \end{bmatrix} = \begin{bmatrix} s_1(\omega) \\ s_2(\omega) \end{bmatrix}, \tag{3.13}$$

which correspond exactly to the injecting signals $s_1(\omega)$ $s_2(\omega)$ focusing on the fault, as represented in figure 3-7. After having computed the Fourier anti-transform of $s_1(\omega)$ $s_2(\omega)$, the two time-domain components (for a 2-port transmission line) or the n components (for a n-port transmission line) of the eigenvector associated with the "faulty" eigenvalue are injected along the line, and a focusing is obtained at the meeting point founded by its intersection both in space and time. In other words, when the components of such eigenvector cross each other the energy is maximized at that point and the fault position is detected. The DORT graphical representation which figures out these concepts is called "*Space-Time*" plot and it is shown in figure 3-9, referred to the transmission line of figure 3-7. In particular, at the instant *t=0* the first time-domain component of $\underline{v}_1$ (yellow line) is injected from the testing port (1) along the line while its second component (blue

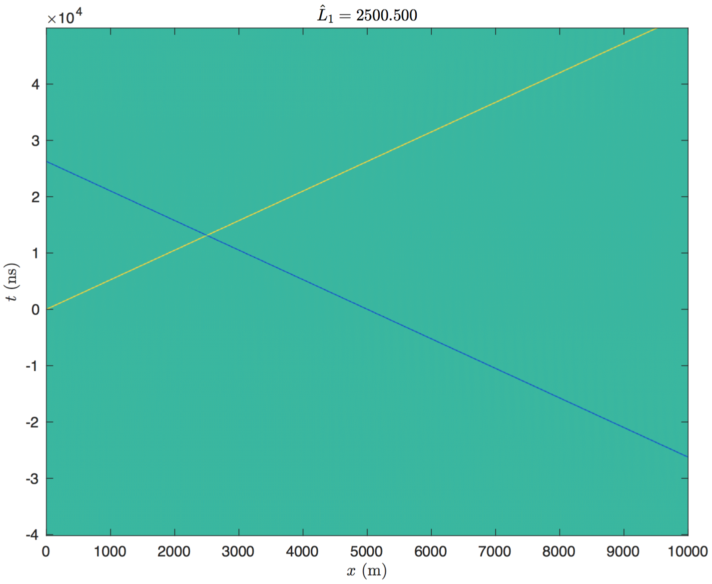

Figure 3-9: Space-Time plot representing the eigenvector components for a two-port transmission line in presence of a single fault

line) is injected from the testing port (2) with a time delay ($\tau_2 - \tau_1$), corresponding to the phase of the transmission coefficients of matrix K. According to the figure 3-7, the meeting point between the two components is exactly at the fault position, l_1=2.5km. It is important to consider that in our simulations, as will be better shown in the next chapters, the fault is considered as an impedance discontinuity with w=*1*, and this is the reason why in figure 3-9 the fault is localized at 2500.5m.

The operational concepts of DORT have been explained in this section and its ability to localize the fault is shown. It is a very interesting method which allows to make a fault location and detection through a simple SVD or EVD decomposition. With respect to TDR, a model must be known a priori and inserted into the simulation software, in our case Matlab. The RSIM code has been adopted with the faulty line model and the measurements implemented in the code. This allows an easier measurement procedure since all the computational work is done by the software. It is able to localize the fault efficiently at different conditions, but shows great advantages in particular in two cases:

(1) *open- or short- circuited lines* (figure 3.10(a)), when multiple reflections are present, since its ability to maximize the energy at the fault position makes the focusing level higher, even than quite low SNR values;

(2) *multiple faults* (figure 3.10(b)), due to its ability to selectively individuate a precise eigenvalue associated to a fault.

However, it is not our cases since as hypotheses of this work a single soft fault is considered and the transmission line is matched-end at all its terminations. Therefore,

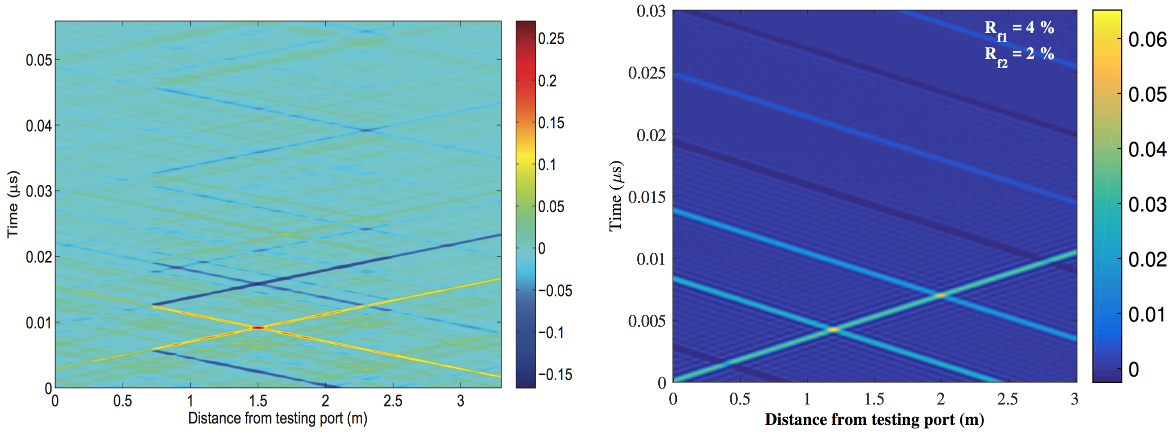

(a) *Multiple reflections*

(b) *Multiple faults*

Figure 3-10: Space-Time diagrams

no other reflections are present due to the testing ports but only the one generated by the fault. Moreover, it is a time-domain method and thus the spatial resolution problems arisen with TDR in presence of losses (see chapter 2) still occur in DORT. A development of a new method to overcome these problems is needed and, as shown in the next section, TR-MUSIC in wiring networks is developed.

3.4 MUSIC Method in Guided Wave Propagation

TDR and DORT methods are essentially based on a time-domain approach, and thus rely on the availability of potentially large bandwidths in order to create the conditions for good spatial resolutions. In fact, the spatial resolution $\varDelta s$ shown in the equation 2.20 is inversely proportional to the bandwidth and in presence of losses it is limited, resulting in bad resolutions. In this section, MUSIC is introduced in wiring networks. Differences with respect to the open media case are considered and different versions are proposed and discussed.

3.4.1 Standard MUSIC Method

In section 3.2.2, a general idea of MUSIC in free space has been presented where the concepts of *Pseudo-spectrum* and *Green function* are introduced. Standard MUSIC is the method introduced by Schmidt in the acoustic field: here, the same concepts will be illustrated in a faulty transmission line and they will be shown in a deeper way. Standard MUSIC is based on a projection procedure between the Green functions $\underline{g}(x)$ at each line position x and the eigenvectors $\underline{v}_i^{\perp}$ (from now on marked with $\perp$ to make intuitive their belonging in $\mathcal{N}$, related to $\lambda_i^2 \approx 0$). To better understand the role of the

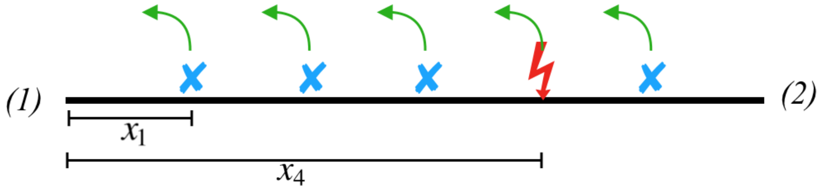

Figure 3-11: Green function generation from five different line positions

Green functions and the projection operations, an example is shown in figure 3-11. Five different line positions are considered, included the real fault position $\tilde{x}$ (in the example corresponding to x_4) which is distant l_1 from the testing port (1). Each position is a good candidate for the detection of the fault position since the exact position of the fault is not known a priori. MUSIC operates analyzing the phase patterns of different functions and comparing the phase of the noise space eigenvectors derived from the measured scattering matrix with the phase of the Green function vector at each position of the line. The green arrows in the figure represent the Green functions generated from each candidate position. Ideally, exciting every point of the line, the Green function of such a point represents the propagation function generated from this point to the testing ports, along the line. As matter of fact, the Green function is no more than a transfer function, considered at different line positions. From a mathematical point of view, it is given by:

$$\underline{g}(x) = \begin{bmatrix} e^{-j\beta x_1} \\ e^{-j\beta x_2} \\ \vdots \\ e^{-j\beta x_p} \end{bmatrix} = \begin{bmatrix} e^{-j\omega\tau_1} \\ e^{-j\omega\tau_2} \\ \vdots \\ e^{-j\omega\tau_p} \end{bmatrix}, \tag{3.14}$$

where in this example p=*5*. Considering go and back from the testing port (1) to the x_k position, the Green function vector becomes:

$$\underline{g}(x) = \begin{bmatrix} e^{-j2\beta x_1} \\ e^{-j2\beta x_2} \\ \vdots \\ e^{-j2\beta x_p} \end{bmatrix} = \begin{bmatrix} e^{-j2\omega\tau_1} \\ e^{-j2\omega\tau_2} \\ \vdots \\ e^{-j2\omega\tau_p} \end{bmatrix}. \tag{3.15}$$

According to equation 3.5, when the Green function at position x_k gets zero projection onto the noise subspace $\mathcal{N}$ eigenvector, and thus when the two phase patterns coincide ($x_k = \tilde{x}$), the Pseudo-spectrum function $\varPhi(x)$ is maximum and a peak is detected at that fault position. Graphically shown in figure 3-12, some considerations are intuitive looking at this figure. First of all, it is important to observe that a 2-dimensional vectorial space is considered since a 2-port line is taken into account in this case. The Green

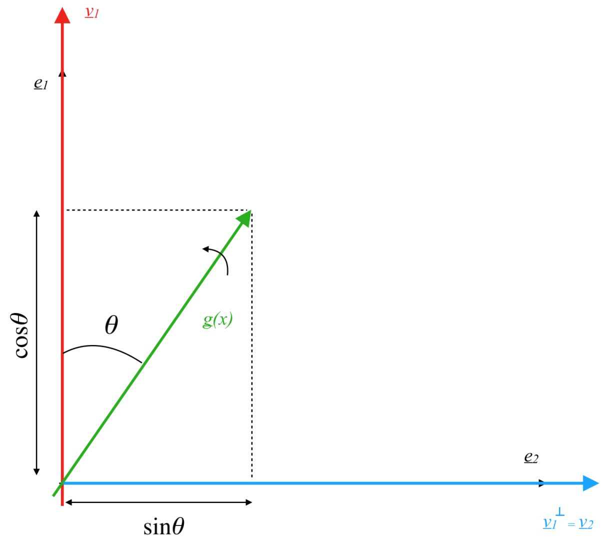

Figure 3-12: Projection operation in standard MUSIC

function vector rotates in such a 2-dimensional space and when the projection between it (green vector) and the noise subspace eigenvector (blue vector) is maximum, the Pseudo-spectrum function $\Phi(x)$ tends to infinite. In this case $\underline{g}(x)$ is exactly orthogonal to the signal subspace eigenvector $\underline{v}_1$, due to the fact that $\mathcal{S} \perp \mathcal{N}$. The noise subspace is taken into account in the projection procedure since the zero point of $sin\vartheta$ and not the maximum of $cos\vartheta$ is detected. As a matter of fact, MUSIC is a DOA estimation method and it is going to estimate the direction of arrival (ϑ) of a signal with respect to another one and in guided wave propagation that angle is nothing else than the displacement between $\underline{g}(x)$ and $\underline{v}_1$. The research of the zero points of $sin\vartheta$ is advantageous since, as shown in figure 3-13, the projection is represented by a sinewave in function of ϑ, due to the Green function vectorial rotation. It is easy to observe that the cosine function (blue line) is quite smooth around its maximum and it is quite hard to identify the exact maximum value of $\cos\theta$. On the other hand, since the behavior of the sinusoidal function (red line) around its zero points is sharper, the and the Green functions $\underline{g}(x)$ at each line position "*well-resolvedness*" criterion is verified and a better resolution obtained.

In noiseless case standard MUSIC is very accurate, but in presence of noise the vector $\underline{v}_1^{\perp}$ is particularly subject to noise and over a certain number of realizations the accuracy deteriorates. Briefly speaking, considering the figure 3-12, in presence of noise the vector $\underline{v}_1^{\perp}$ (which in the 2-port case is equal to $\underline{v}_2$) rapidly moves around its starting position and the projection procedure with $\underline{g}(x)$ is getting worse. Accordingly, a new version of MUSIC is shown in the next section where the same operational procedure is kept, but the noise subspace is no more considered, aimed to improve the accuracy.

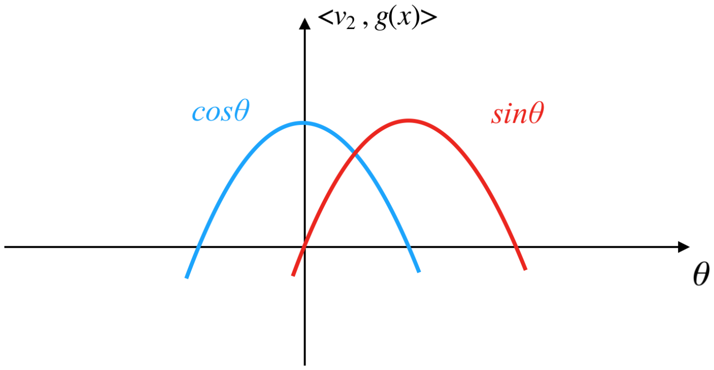

Figure 3-13: Projection function

3.4.2 Inverted MUSIC Method

The ability of TR-MUSIC to provide a super-resolution performance is one of its strengths which makes it interesting and advantageous with respect to other fault location methods. When the projection between $\underline{g}(x)$ and $\underline{v}_1^{\perp}$ is maximum ($min\ sin\vartheta$), it wll be minimum onto $\underline{v}_1$ ($max\ cos\vartheta$). Therefore, a necessary condition for obtaining the super resolution is to make $sin\vartheta$ nil. In standard MUSIC (see 3.4.1), what allows to obtain this super resolution is the orthogonality between the signal and the noise subspace. However, this condition can also be verified considering the inversed procedure; instead of the orthogonal vector to $\underline{v}_1$, the orthogonal Green function vector $\underline{g}(x)^{\perp}$ is taken into account, as represented in figure 3-14. In such case, nor the whole scattering matrix neither the EVD decomposition are considered in the computations but $\underline{v}_1$ is the phase pattern of the S_{ii} vector obtained directly from measurements. The advantages of this MUSIC version, called "*Inverted MUSIC*", make it more reliable and more practical since:

(1) the noise subspace $\mathcal{N}$ is not involved, which allows to improve the accuracy estimation in case of low SNR values;

(2) only the reflection parameters S_{ii} are considered, which in case of long lines does not imply the measurement of transmission parameters.

Involving only the reflection scattering parameters, the equations 1.31 and 1.32 shown in 1.2.2 are recalled where both magnitude and phase are illustrated. In particular, normalizing them, the *ith* term of the vector $\underline{v}_1$ is given by:

$$\frac{S_{ii}}{|S_{ii}|} = \angle S_{ii} = e^{-j2\beta l_i} = e^{-j2\omega\tau_i}, \tag{3.16}$$

where l_i is the distance between the *ith* port and the fault while τ_i the time needed to the wave for reaching the fault from such a port. The only phase term is obtained and

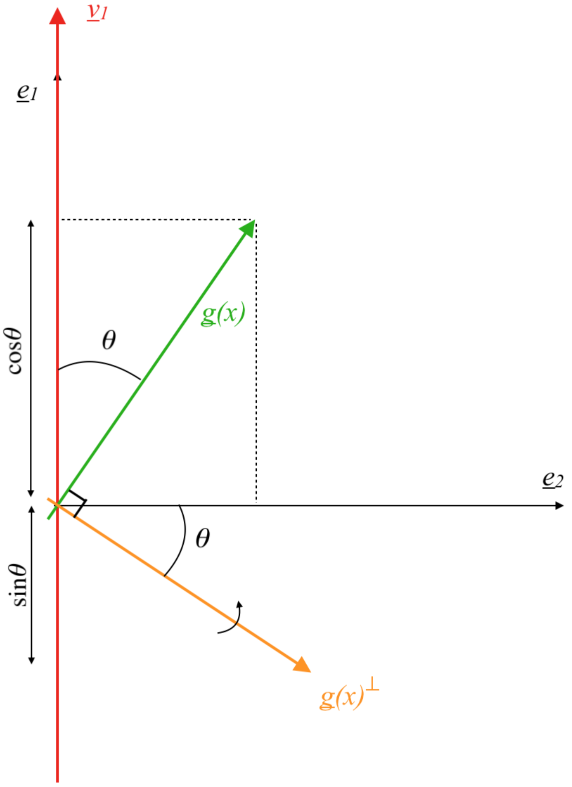

Figure 3-14: Projection operation in inverted MUSIC

can be directly projected onto the orthogonal Green function vector

$$\underline{g}(x)^{\perp} = \begin{bmatrix} 1 \\ -1 \end{bmatrix} \begin{bmatrix} e^{-j2\beta x_1} \\ e^{-j2\beta x_2} \\ \vdots \\ e^{-j2\beta x_p} \end{bmatrix} = \begin{bmatrix} 1 \\ -1 \end{bmatrix} \begin{bmatrix} e^{-j2\omega \tau_1} \\ e^{-j2\omega \tau_2} \\ \vdots \\ e^{-j2\omega \tau_p} \end{bmatrix}, \tag{3.17}$$

having the same pattern.

Therefore, in Inverted MUSIC no matrix subspaces are adopted and the inversed projection procedure is applied. The creation of the vectors to be projected can be accomplished in two ways, and thus two different approaches will be illustrated:

(1) *Frequency-delay MUSIC*, where all the frequency samples are involved and the vectors are function of each ω_j sample;

(2) *Port MUSIC*, where single frequency samples are involved and the creation of $\underline{v}_1$ and $\underline{g}(x)^{\perp}$ is performed depending on the number of testing ports.

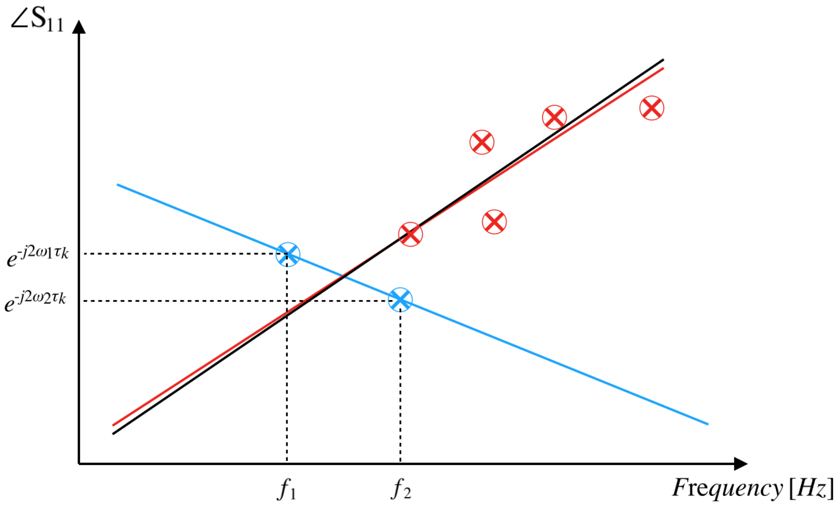

Figure 3-15: Graphical linear regression of the Frequency-delay MUSIC functional operation

Frequency-delay MUSIC

Frequency-delay MUSIC operates at different values of frequencies and considering only one testing port: thus, the only scattering parameter S_{11} is considered. Given a single 2-port transmission line with p τ, where each τ indicates a different position along the line, from every τ is generated a Green function where all the frequency samples m are included and mixed up in the vectors creation. Every scalar component depends on the jth frequency sample. For a specified kth τ:

$$\underline{g}(x)^{\perp} = \begin{bmatrix} 1 \\ -1 \end{bmatrix} \begin{bmatrix} e^{-j2\omega_1\tau_k} \\ e^{-j2\omega_2\tau_k} \\ \vdots \\ e^{-j2\omega_m\tau_k} \end{bmatrix}, \qquad \underline{v}_1 = \begin{bmatrix} e^{-j2\omega_1\tilde{\tau}} \\ e^{-j2\omega_2\tilde{\tau}} \\ \vdots \\ e^{-j2\omega_m\tilde{\tau}} \end{bmatrix}, \tag{3.18}$$

where $\tilde{\tau}$ represents the exact fault position and the size of these vectors is given by the m frequency samples. All the frequency samples are mixed up together and the fault position is looked for: cycling for all the τ positions along the line, the kth τ for which the relationship $\tau_k = \tilde{\tau}$ is verified results in the maximum projection between $\underline{v}_1$ and $\underline{g}(x)^{\perp}$ and the fault candidate is found. Frequency-delay MUSIC operates as a linear regression in order to find out the exact τ value. Greater is the number of frequency samples m, better will be the regression and the resulting fitting. Considering the figure 3-15, the black line represents the phase terms of the measured $\underline{v}_1$ with the exact $\tilde{\tau}$. For a specified kth τ value, the vector $\underline{g}(x)^{\perp}$ is represented by the red line. When the fault position has been detected, the behavior in frequency of the Green function phase patterns corresponds to

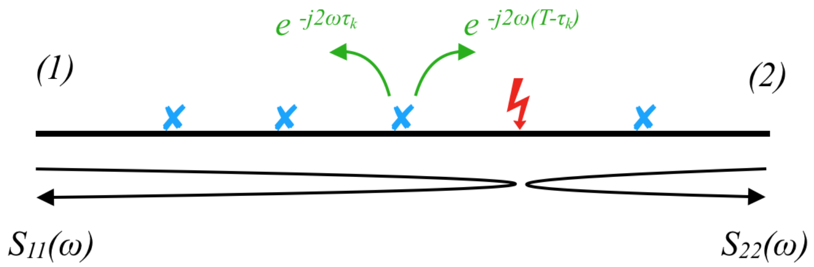

Figure 3-16: Transmission line excited from both the testing ports and particular on Green function generation from a fault candidate

$\angle \underline{v}_1$. If there are only few frequency samples the regression can bring to very big mistakes, as shown in the blue line case, where the projection procedure does not allow to find out the exact position of the fault.

However, frequency-delay-MUSIC shows a problem in its procedure since, in order to obtain the phase pattern vector of the measured scattering coefficient $\underline{v}_1$, a normalization of the S_{11} coefficient is needed. But since the magnitude of this coefficient depends on frequency, normalization is not possible in this case due to the fact that all the frequency samples are mixed up together. This problem can be overcome considering another version of Inverted MUSIC, implemented in this thesis work, which operates at single frequencies but considering more testing ports: *Port MUSIC*.

Port MUSIC

Port MUSIC does not operate with many frequency samples but at single frequencies to fit the fault position. No regression is resulting and all the testing ports of the line must be taken into account for the vector construction. However, there is a price to be paid since in order to apply this method the entire length of the line must be known, and consequently the whole time T necessary for a wave to travel along the line. It is important to note that in this work the time delays τ are considered and not the distances x between testing ports and fault since in this case there is not necessity to know the value of the velocity of the wave propagation, but only the frequency. Considering the line in figure 3-16, where a simple 2-port line is illustrated, both the ports are excited and the two reflection scattering parameters S_{11} and S_{22} are involved:

$$S_{11}(\omega) = \Gamma_1 = \Gamma_f e^{-j2\omega\tilde{\tau}}, \tag{3.19}$$

$$S_{22}(\omega) = \Gamma_2 = \Gamma_f e^{-j2\omega(T-\tilde{\tau})}, \tag{3.20}$$

where $\tilde{\tau}$ is the time needed for the wave to reach the exact fault position from the port (1). Normalizing the reflection coefficients S_{ii}, the phase vector $\underline{v}_1$ is obtained:

$$\underline{v}_1 = \begin{bmatrix} \frac{S_{11}}{|S_{11}|} \\ \frac{S_{22}}{|S_{22}|} \end{bmatrix} = \begin{bmatrix} e^{-j2\omega\tilde{\tau}} \\ e^{-j2\omega(T-\tilde{\tau})} \end{bmatrix}, \tag{3.21}$$

at a given single frequency sample. At each fault candidate position τ_k it is possible to find out the Green function generated from such a point to both the testing ports (green line in figure 3-16):

$$\underline{g}(x)^{\perp} = \begin{bmatrix} 1 \\ -1 \end{bmatrix} \begin{bmatrix} e^{-j2\omega\tau_k} \\ e^{-j2\omega(T-\tau_k)} \end{bmatrix}. \tag{3.22}$$

The *kth* τ correspondent to $\tilde{\tau}$ results in a complete vectorial projection. Thus, p Green function vectors are built, one for each *kth* position of the line, whose size is given by the n number of testing ports. For each *kth* fault candidate, single frequency measurements are carried out cycling from 0 to m.

The great advantage of Port MUSIC is the fact that it can operate at single frequencies; it is therefore possible to apply the normalization of S_{ii}. However, the price to be paid is that the entire length of the line must be known a priori and that a certain number of measurements must be done, corresponding to the n number of testing ports. Although it can operate at single frequencies, in order to be more robust it is better to consider more frequency samples. In fact, the *Pseudo-spectrum* function $\Phi(x)$ is defined over many frequency samples:

$$\Phi(x) = \frac{1}{\sum_{j=1}^{m}\sum_{k=1}^{p} |<\underline{v}_1, \underline{g}(x)^{\perp}>|^2}, \tag{3.23}$$

for each *kth* fault candidate. It is worthy to observe that in case of multiple faults, not only the vector $\underline{v}_1$ is involved in the projection but the N $\mathcal{S}$ eigenvectors, where N represents the number of faults, as the number of scatterers in open media.

In order to better understand this concept, the graphical representation of figure 3-17 is showed, where the performances of Port MUSIC are analyzed in the 10km lossless and noiseless line of figure 3-7. The figure represents the Pseudo-spectrum function $\Phi(x)$ and the yellow straight line represents the exact position of the fault. Port MUSIC can operate at single frequencies and at each frequency sample it is able to localize the fault. In particular, considering the specified samples of 0.6, 1.2 and 1.8MHz represented by the pink, red and green horizontal line, respectively, it is possible to observe that at each frequency many peaks are detected: in other words, $\Phi(x)$ is maximum at different points for a single frequency. These peaks are represented by the colored points along each horizontal line. For example, considered the frequency of 1.2MHz (red line) for a

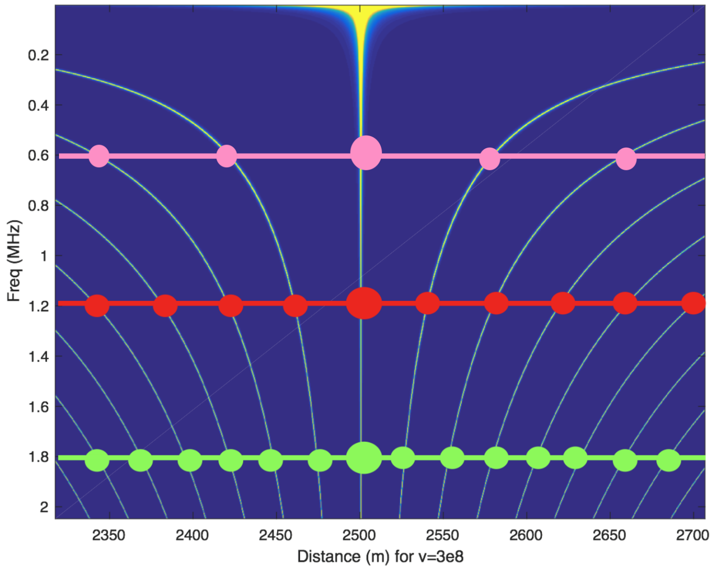

Figure 3-17: Pseudo-spectrum representation in a lossless and noiseless line with the fault at 2.5km from the first testing port

range going from 2300m to 2700m, the Pseudo-spectrum is maximum in 10 points: Port MUSIC finds 10 fault candidates at this frequency in such range. In the same way, at the frequency 0.6MHz (pink line) 5 fault candidates are detected and at 1.8MHz (green line) 14. As a matter of fact, considering many frequencies it is possible to state which is the exact fault position: each fault candidate is evaluated at each frequency, and only one of them is collected for all the considered frequencies. This candidate is represented with bigger balls, and underlined by the the yellow straight line.

Now the question is: why at each frequency many peaks are found? And what the yellow hyperbolas on the Pseudo-spectrum plot represent? To answer at these questions, it is important to note that at each frequency the detected fault candidates are periodically separated. This is due to the fact that in transmission lines theory the position along a line is periodic and then the Green function is periodic too. In particular, moving from the x_k position to the right or left side along the line by $\lambda/4$, the Green function is given by:

$$\underline{g}(x) = \begin{bmatrix} e^{-j2\beta(x_k+\frac{\lambda}{4})} \\ e^{-j2\beta(L-x_k-\frac{\lambda}{4})} \end{bmatrix}. \tag{3.24}$$

Considering the only S_{11} reflection parameter and the position $x_k + \frac{\lambda}{4}$:

$$e^{-j2\beta(x_k+\frac{\lambda}{4})} = e^{-j2\beta x_k} \cdot e^{-j2\beta\frac{\lambda}{4}} = e^{-j2\beta x_k} \cdot e^{-j2(\frac{2\pi f}{v})\frac{\lambda}{4}} \tag{3.25}$$

$$= e^{-j2\beta x_k} \cdot e^{-j4\frac{\pi}{\lambda}\frac{\lambda}{4}} = e^{-j2\beta x_k} \cdot e^{-j\pi} \tag{3.26}$$

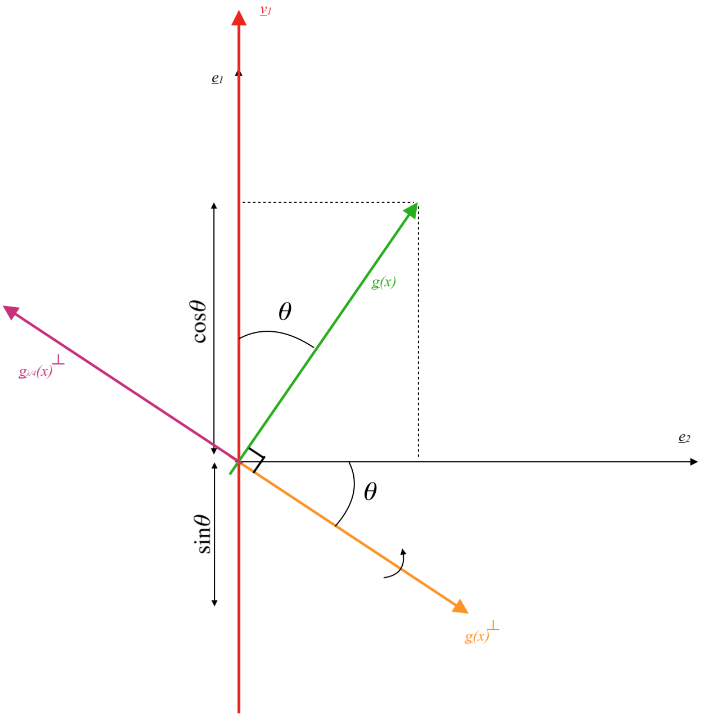

Figure 3-18: Illustration of projection procedure with periodicity of transmission line

and thus, the resulting vector is the opposite vector to the orthogonal Green function vector:

$$\underline{g}_{\frac{\lambda}{4}}(x)^{\perp} = -\begin{bmatrix} 1 \\ -1 \end{bmatrix} \begin{bmatrix} e^{-j2\beta x_k} \\ e^{-j2\beta(L-x_k)} \end{bmatrix}. \tag{3.27}$$

As shown in figure 3-18, when the projection is zero for $\underline{g}(x)^{\perp}$, it will be zero also for its opposite vector. Consequently, considering the Pseudo-spectrum plot, different periodical peaks are detected and the yellow hyperbolas are formed, called *ghosts*. In order to clearly show this concept, the Pseudo-spectrum function (see equation 3.23) is taken into account and the detected peaks are plotted in function of distance, as shown in figure 3-19. Considering the same three frequency samples as in figure 3-17, it is evident that they are distanced by $\frac{\lambda}{4}$, figure 3.19(a). Besides, only at one position all the frequencies converge together and are able to detect a peak: it is the exact fault position. Moreover, more frequency samples are considered, more accurate the fault location is and less errors are made, figure 3.19(b).

Therefore, the concepts of *Inverted MUSIC* have been shown in this section and the advantages of *Port MUSIC* with respect to the other methods are verified. It is important to note that Inverted MUSIC does not show differences with respect to Standard MUSIC in the noiseless case (figure 3-19): advantages in noise robustness will be discussed in chapter 4. Accordingly, in the next chapters the results and performances comparison between Port MUSIC and TDR will be shown.

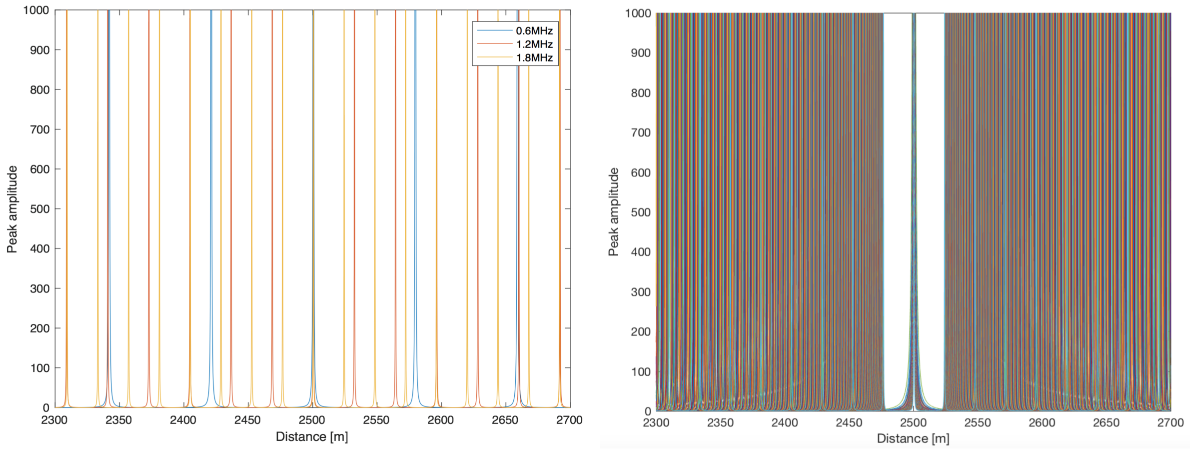

(a) *Three frequency samples* (b) *All frequency samples*

Figure 3-19: Peak detection in Port MUSIC

3.5 Summary

In this chapter, two time reversal based methods have been introduced: DORT and MUSIC. Both derive from the same scattering matrix decomposition and operate on the S subspace analysis, but their functional mode is different since based on different subspaces ($\mathcal{S}$ for DORT and $\mathcal{N}$ for MUSIC). The advantages of DORT are several but not in our case study. In fact, when there are multiple faults or multiple reflections it becomes very useful since it is able to maximize the energy at the fault positions. The theoretical concepts and the procedure have been presented, and its graphical representation for fault location shown.

The substantial difference of MUSIC with respect to DORT is that it is not a time-domain based method but it operates in frequency, through a projection procedure where *Green functions* at different positions on the line and *S noise subspace* are involved. This results in a very super resolution performances which overcomes the limitations in time encountered by TDR and DORT above all in presence of losses (see chapter 5). Moreover, a new version theoretically more robust than the standard one has been introduced, *Inverted MUSIC*, and two different approaches of this technique presented. In particular, *Port MUSIC* has resulted very interesting since it is able to operate at single frequencies, improving the spatial resolution problems arising with TDR.

In the next chapters, a performances comparison between *Port MUSIC* and *TDR* will be shown, from both simulations and experiments points of view. In particular, in the next chapter a 10km 2-port lossless line is considered as NUT, in chapter 5 a 2-port lossy line and in chapter 6 a Y-branched line.

Chapter 4

Soft Fault Location in a Single Lossless Line

In the previous chapters the concepts and the general ideas of different fault location methods have been presented, with their advantages and limitations. The time reversal based methods have been introduced in two main methodologies: DORT and MUSIC. After having deeply theoretically analyzed such methods, *Port MUSIC* is revealed the most profitable, ensuring good performances even in presence of noise.

From this chapter on, simulations studying the methods' ability in soft fault location are analyzed and a comparison between TDR and Port MUSIC performances carried out. Precision and accuracy of both methods are investigated with different noise levels and according to its intensity a specified study is done.

The NUT considered in the numerical simulations is a 10km line length MV power cable whose parameters, structure and behavior in frequency have been studied in chapter 2. In this chapter, a lossless line is considered while more complex structures will be presented in the next chapters, and the fault is represented as an impedance discontinuity.

4.1 Introduction

In chapter 1 the general theory of a lossless line has been presented. Only L and C are involved and the characteristic impedance is represented by the equation 1.16. In table 2-4 the electrical parameters in frequency of our NUT are shown and considering the high frequency values the characteristic impedance Z_c of the healthy line can be computed:

$$Z_c = \sqrt{\frac{L}{C}} = 19.24\,\Omega. \tag{4.1}$$

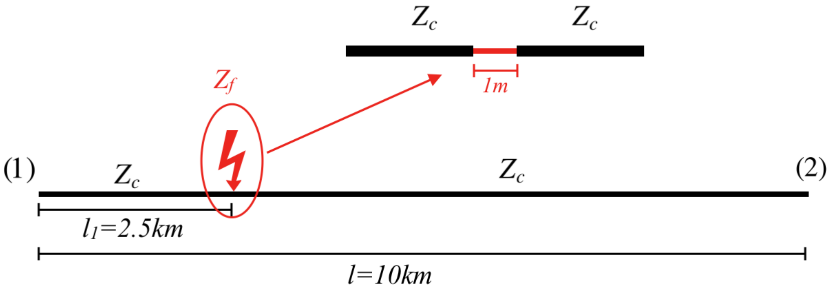

Figure 4-1: Transmission line considered in the simulations with 1m-fault situated at 2.5km from the first testing port and represented by an impedance discontinuity

The fault is represented as a thinner line portion, obtained for example crushing it and the consequent characteristic impedance of such a part will be different. In particular, in this work a 10% increase and decrease of C and L respectively is considered and the faulty characteristic impedance is:

$$Z_f = \sqrt{\frac{0.9 \cdot L}{1.1 \cdot C}} = 17.4\,\Omega. \tag{4.2}$$

The fault is considered as 1m line length and is situated 2.5km from the first testing port over the 10km line length, as shown in figure 4-1. Since a lossless line is considered, there are no limitations in bandwidth and so an arbitrarily maximum frequency can be chosen. In this work a 10MHz bandwidth with 10kHz of frequency sampling is adopted. The reason why we have not chosen an higher maximum frequency deals with the fact that in the next chapter a lossy line is analyzed and, in order to compare the results between the two cases, a lower bandwidth is considered. Thus, the velocity of propagation can be computed at high frequencies and is given by:

$$v = \frac{1}{\sqrt{LC}} = 1.9044 \cdot 10^8\,\frac{m}{s}. \tag{4.3}$$

The test spectrum signal is represented by a *Taylor window*, which is similar to a Chebyshev window but with a weaker decrease of secondary lobes (figure 4.2(b)). Other kinds of windowing could be chosen, as the rectangular or Gaussian one, but Taylor ensures a good compromise between the spatial resolution of the main lobe and the presence of secondary lobes. The spectrum signals are considered in baseband and thus only half of the whole bandwidth is considered for the simulations: therefore the maximum frequency is 5MHz and the number of frequency samples 501.

Before starting the simulations, it is important to precise how the SNR has been defined in this work. A very important role is played by it, as will be shown in the next sections of this chapter. In particular, it is defined in frequency-domain since when TDR

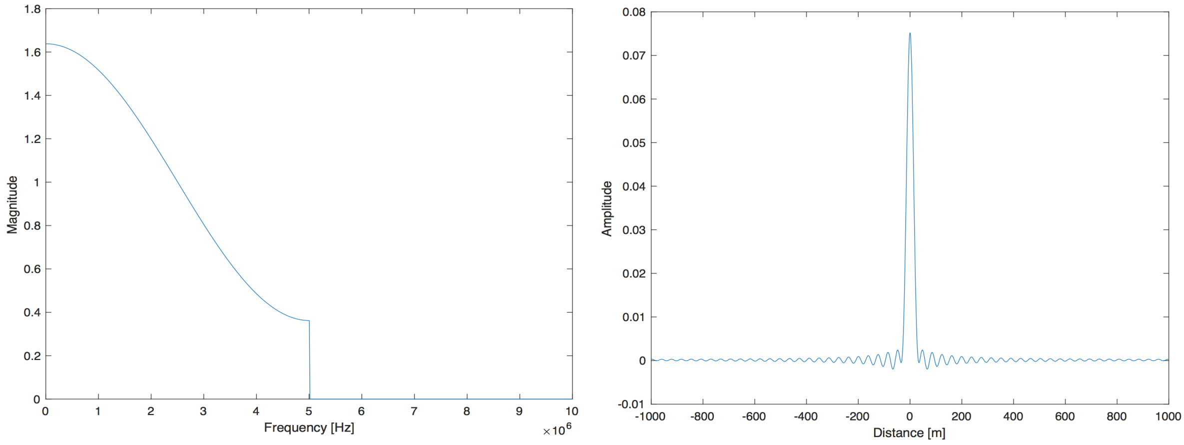

(a) *Frequency-domain* (b) *Time-domain*

Figure 4-2: Peak detection in Port MUSIC

is considered a Fourier anti-transform is applied in order to obtain the time-reflected echo, and at each time instant a convolution over all the frequency samples is carried out. In other words, a mean operation is involved and thus the resulting SNR at each time instant will be lower than computing it directly in time. Therefore, defining it in time-domain the noise robustness of TDR would be worse than what considered in this work. Figure 4-3 represents the amplitude of S_{11} considering three different SNR values in frequency, 20dB, 10dB and 0dB.

4.2 Precision Estimation

In this section TDR and Port MUSIC are compared in the precision at which they are able to locate the fault. Different SNR values are considered in such a simulation and a study of spatial resolution is carried out. The methods' performances are analyzed separately and the results compared considering the same conditions.

TDR

As introduced in chapter 1, TDR operates injecting a time impulse in the network and the reflected wave is analyzed. In particular, the time delay needed to the reflected wave for reaching the injecting port allows the identification of the fault position. The reflectogram is the graphical tool with which it is possible to observe the reflected wave and therefore detecting the fault position. As a matter of fact, TDR operates with a Fourier anti-transform, where the time-domain reflection coefficient S_{11} is retrieved.

Considering the faulty line of figure 3-8, the correspondent reflectogram is shown in figure 4-4. From this figure some observations can be done. First, uncertainty about the

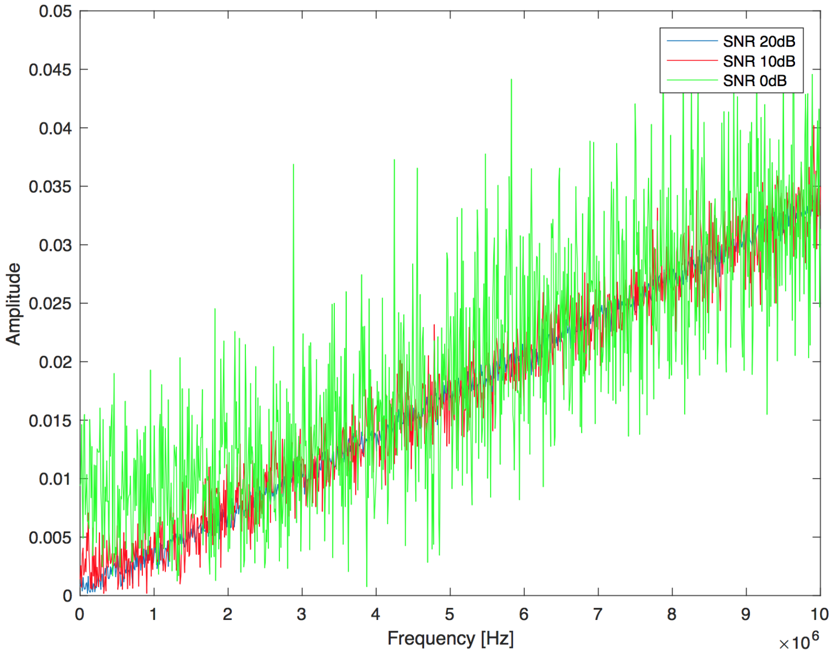

Figure 4-3: S_{11} amplitude in frequency at three different SNR: 20dB (blue), 10dB (red) and 0dB (green)

fault position can be observed since the fault is not detected through a single peak or a singularity but is located between 2480m and 2520m. It can be any point inside this region: for sake of simplicity in our work we have considered the middle point between the two peaks. Then, the derivative shape of the reflectogram is interesting to be investigated. Considering the same line in figure 3-8, the reflection coefficient seen from the testing port *(1)* can be retrieved starting from Γ_0:

$$\Gamma_f = \Gamma_0 + (1 - \Gamma_0^2)(-\Gamma_0)e^{-j2\beta w}, \tag{4.4}$$

and after some mathematical operations,

$$\Gamma_f = j2\beta w \Gamma_0 e^{-j\beta w} = j\omega 2\frac{w}{v}\Gamma_0 e^{-j\beta w}, \tag{4.5}$$

where the derivative term $j\omega$ explains the reflectogram shape obtained. It is interesting to observe that the previous analysis is valid only in case of electrically short fault. In fact, according to [17], the term $\frac{\Gamma_f(\omega)}{\Gamma_0}$ can be approximated by the following equation:

$$\frac{\Gamma_f(\omega)}{\Gamma_0} = \frac{Aj\omega}{j\omega + p}, \tag{4.6}$$

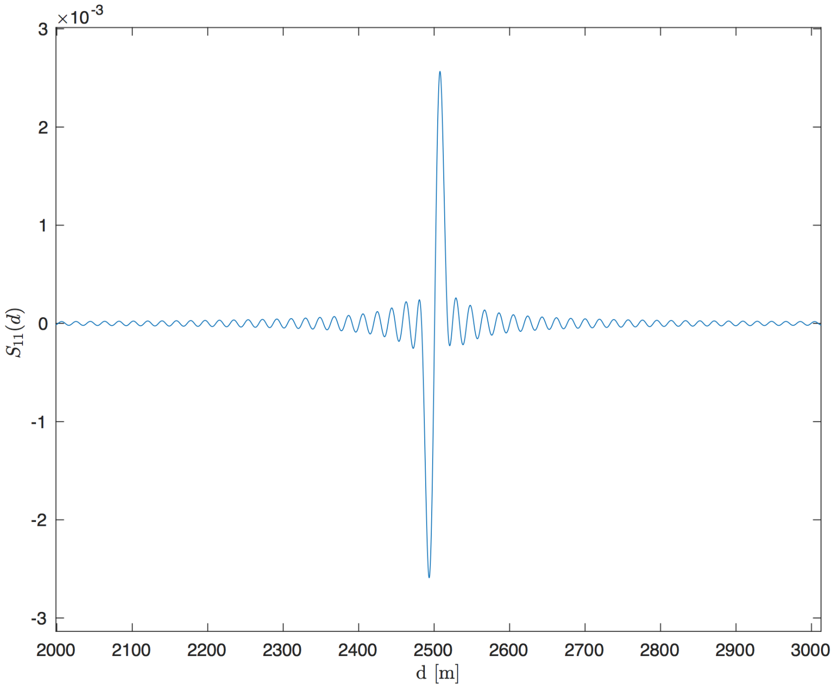

Figure 4-4: Reflectogram in case of 1m-fault over a 10km transmission line

where A is a constant term and p a real-valued pole,

$$\begin{cases} A = \frac{2}{1+\Gamma_0^2} \\ p = \frac{1-\Gamma_0^2}{1+\Gamma_0^2 \frac{v}{w}} \end{cases}, \tag{4.7}$$

found out through a Padé approximation. In the lower frequency range, where the fault is electrically short, a further approximation can be done:

$$\Gamma_f(\omega) = j\omega \frac{A}{p} \Gamma_0, \tag{4.8}$$

and substituting the values of equation 4.7, the equation 4.5 is retrieved. According to this last equation, it is possible to compute the value of $|\Gamma_f|$ at 10MHz of maximum frequency and thus knowing how much the reflected time-domain impulse is decreased with respect to the injected one when encounters the fault. Substituting all the values, with $w = 1$ and the characteristic impedances of equations 4.1 and 4.2:

$$|\Gamma_f(\omega)| = 2\omega \frac{w}{v} |\Gamma_0| = 0.033. \tag{4.9}$$

Therefore, it is important to know whether a fault is electrically short or not; in fact, in case of not electrically short fault, the denominator cannot be neglected and p acts as a real pole, changing the identification of the fault position. In order to evaluate the

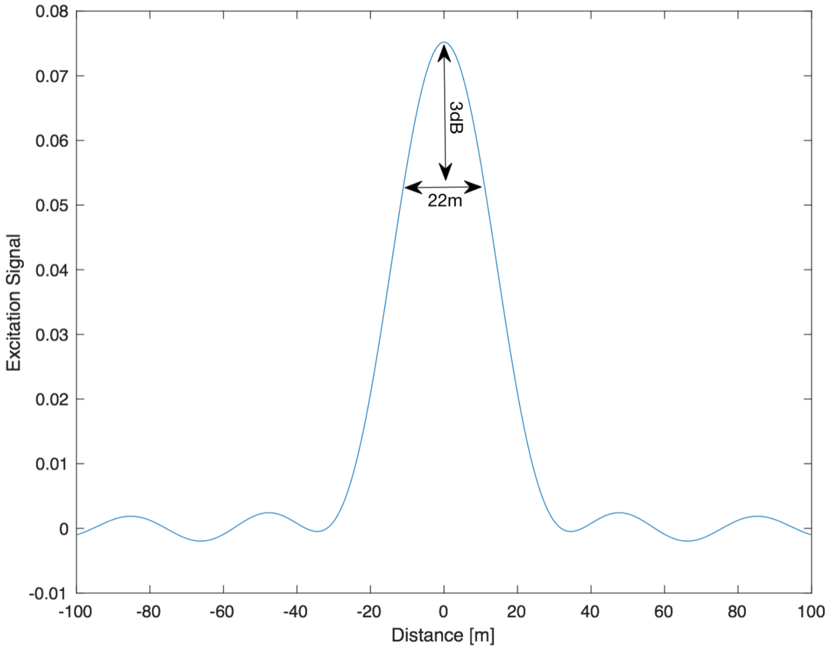

Figure 4-5: Spatial resolution of TDR in case of lossless line

spatial resolution of TDR, and in more general of all the time-domain based methods, the injected time-domain impulse is considered (the resolution does not change when the wave is reflected or transmitted). A protocol must be adopted in order to have the same yardstick for both the methods compared. In particular, a decrease of 3dB from the maximum peak is taken into account.

As shown in figure 4-5, the spatial resolution of the time-domain methods is around 22m when a lossless line is considered which, over a 10km line length, corresponds to 0.22%.

Port MUSIC

The projection procedure operated by Port MUSIC for detecting the peaks involves, as seen in chapter 3, the orthogonal Green function vectors and the normalized S_{ii} vector $\underline{v}_1$. In a lossless line Γ_0 is a real number: for sake of simplicity S_{11} only is considered and is given by:

$$S_{11} = \Gamma_1 = \Gamma_f e^{-j2\beta\tilde{x}} = j\omega 2\frac{w}{v}\Gamma_0 e^{-j\beta w} e^{-j2\beta\tilde{x}}. \tag{4.10}$$

Since MUSIC operates considering the phase terms only, in order to obtain the vector $\underline{v}_1$ as in the equation 3.21, a normalization is needed:

$$\frac{S_{11}}{|S_{11}|} = je^{-j2\omega\tilde{\tau}}. \tag{4.11}$$

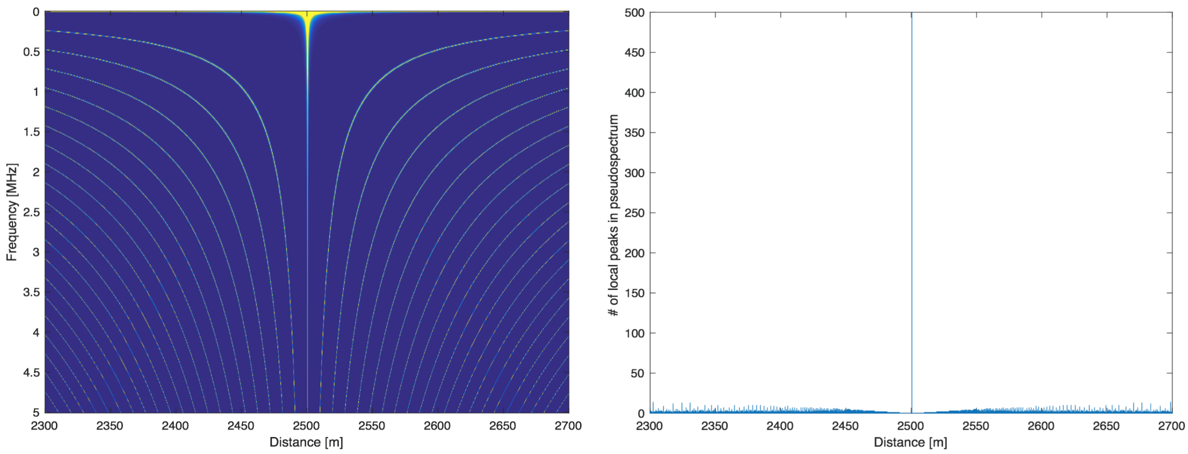

(a) *Pseudo-spectrum* (b) *Frequency counter*

Figure 4-6: Fault location in Port MUSIC considering the line in figure 4-1

However, in this case each normalized S_{ii} coefficient is an imaginary term and the resulting angle is displaced by $\frac{\pi}{2}$. In order to solve this problem, each S_{ii} term shall be multiplied by j and in this lossless case the vector $\underline{v}_1$ is built up as follows:

$$\underline{v}_1 = \begin{bmatrix} \frac{jS_{11}}{|S_{11}|} \\ \frac{jS_{22}}{|S_{22}|} \end{bmatrix} = \begin{bmatrix} e^{-j2\omega\tilde{\tau}} \\ e^{-j2\omega(T-\tilde{\tau})} \end{bmatrix}. \tag{4.12}$$

Running the simulations by Matlab where the projection is applied, the *Pseudo-spectrum* function is obtained where at each frequency several periodic peaks are detected and the fault is clearly located at 2500.5m (figure 4.6(a)). If there is no noise the peaks are found precisely and no spread is present between them. In order to clearly observe the peaks detected by $\Phi(x)$, a plot representing the number of local peaks at each position is figured out in figure 4.6(b). Several peaks are detected, corresponding to the number of fault position candidates collected at each frequency sample. At 2500.5m the number of candidates is 501, since without noise the candidates are not moved away from the exact position of the fault and all the frequencies samples considered in the bandwidth detect it exactly. In case of noise the number of candidates at the fault position is smaller and the spread between the peaks increases.

In figure 4-7, the point A represents the fault candidate in the noiseless case while the point B the fault candidate when a certain value of noise is present, represented by the black line. At a fixed frequency, higher the noise is, worse spatial resolution is expected: decreasing the SNR value, in fact, both accuracy and spatial resolution deteriorate, since the vector $\underline{v}_1$ is subjected to noise

$$< \underline{v}_1, \underline{g}(x)^{\perp} > = < (\underline{s}_1 + \underline{n}_1) \cdot \underline{g}(x)^{\perp} > = < \underline{s}_1 \cdot \underline{g}(x)^{\perp} + \underline{n}_1 \cdot \underline{g}(x)^{\perp}, \tag{4.13}$$

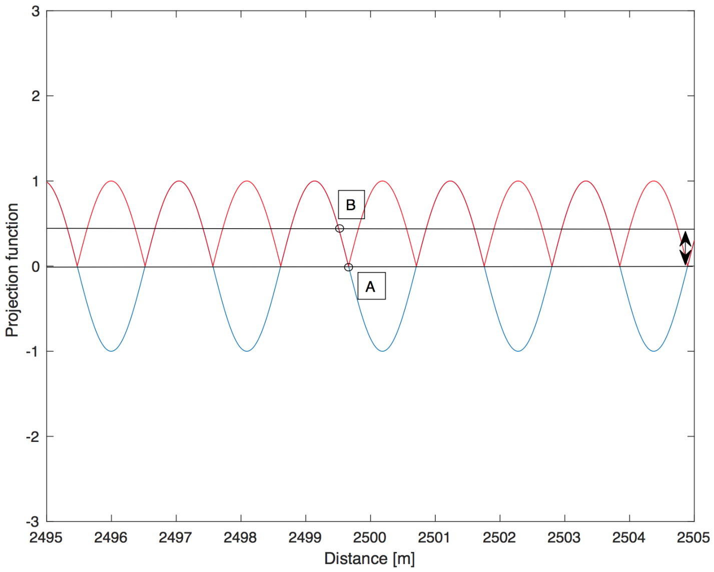

Figure 4-7: Projection function with fault location without (A) and with (B) noise

where $\underline{s}_1$ and $\underline{n}_1$ represent the signal and noise terms of the vector $\underline{v}_1$, respectively. Thus, in presence of noise the peaks are displaced from the exact fault position and from each other. To better understand the behavior, four different SNR values are considered and the correspondent *Pseudo-spectra* are shown in figure 4-8. The influence of noise is more evident considering the frequency counter, in which is shown that decreasing the SNR value less candidates are collected around the fault position and for low values (*i.e. 20dB*) the precise location becomes difficult. A solution adopted to improve this problem at 20dB will be shown in the next section. Figuring out the frequency counter (figure 4-9) it is also possible to compute the "*effective spatial resolution* " at each SNR value. It is important to observe that it is a pragmatic concept, where both accuracy and precision are measured and the resulting displacement represents an accuracy measurement of the method. As expected, it gets worse decreasing the SNR value. It is a different concept with respect to the real spatial resolution, which is the measurement index representing a method precision in the fault detection.

In order to compute the spatial resolution in MUSIC the peaks detected by the Pseudo-spectrum function must be analyzed and since MUSIC operates at single frequencies all the different frequency samples must be taken into account. For high SNR values all the fault candidates are situated around the fault position and most of the frequencies are able to precisely identify the exact position. In such a case, precision dominates on accuracy. On the other hand, decreasing the SNR, the fault is not detected at the exact position and accuracy dominates on precision. In this case, it is senseless talking about the ability of a method in the precision estimation: in fact, it can be very precise in locating the fault but if it is not the exact position it is useless.

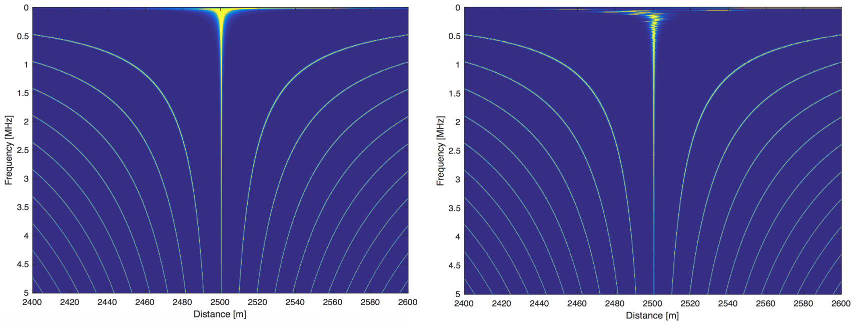

(a) *80dB* (b) *50dB*

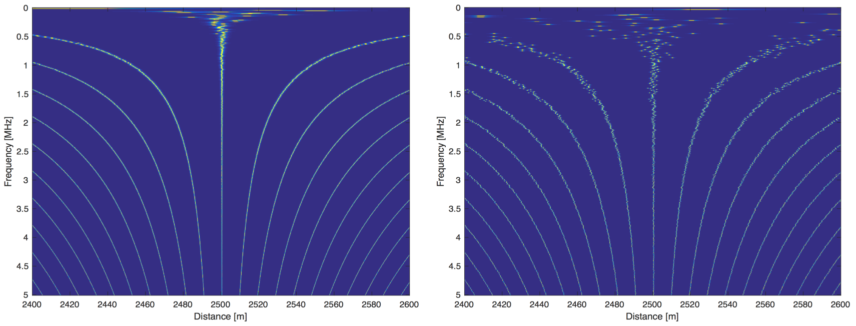

(c) *40dB* (d) *20dB*

Figure 4-8: Pseudo-spectra at different SNR values

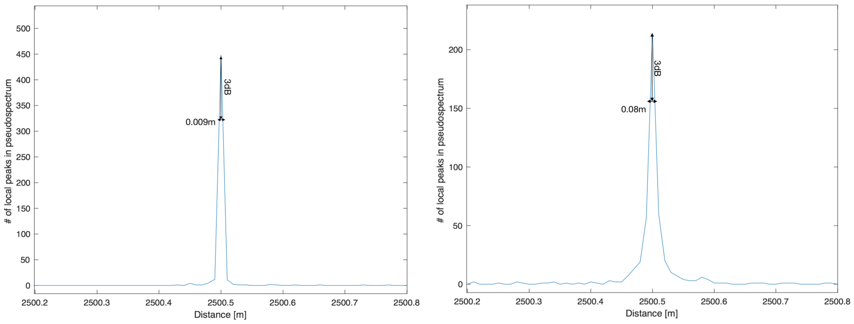

(a) *80dB* (b) *50dB*

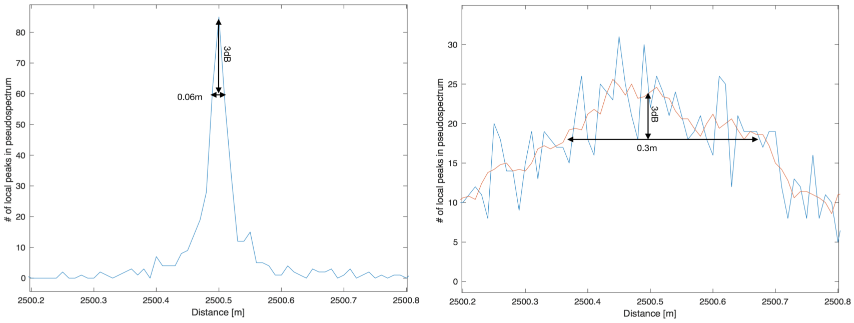

(c) *40dB* (d) *20dB*

Figure 4-9: Frequency counter at different SNR values

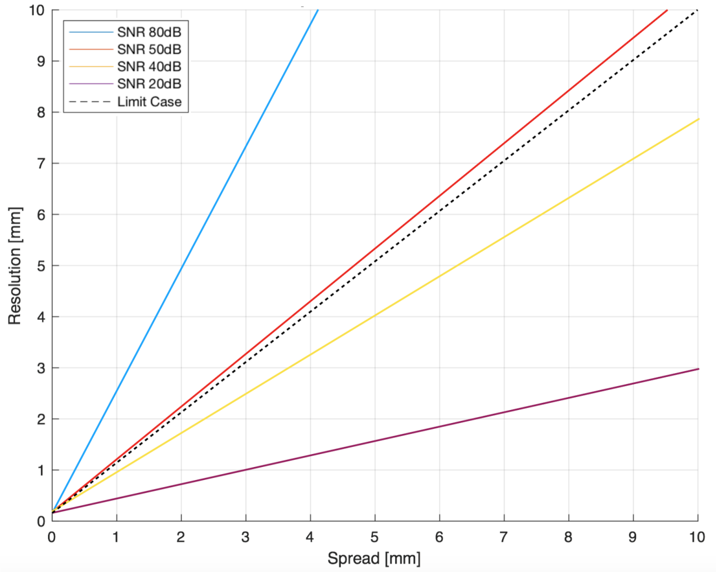

Figure 4-10: Scatterplot between spread and resolution at each frequency sample

This is the reason why for the precision estimation only high values of SNR are considered, the SNR values above which the precision dominates on the accuracy. And now the question is: which values of SNR could be considered for this estimation? And for which values, on the other side, the accuracy dominates on the precision? In order to answer at these questions, for each value of SNR (from 200dB to 0dB distanced by 10dB) a scatterplot is studied, shown in figure 4-10, where for a single noise realization the equivalent spread and the spatial resolution are plotted at each frequency sample. The same four arbitrarily SNR values are considered: 80dB (blue line), 50dB (red line), 40dB (yellow line) and 20dB (violet line). First of all, an interesting thing to observe is the linear relation between resolution and spread at the different SNR values.

For high SNR values the spread is low since the noise does not influence the result in a very deeply way. The precision of the peaks dominates the accuracy and thus in this region is useful compare the methods considering their precision in locating the fault. In the scatterplot it is represented by the 80dB case (blue line) where the slope of the line is positive and the resolution is greater than the spread at each frequency sample. For low SNR values, as the 20dB case (violet line) in the scatterplot, the noise is quite violent and the spread over each frequency value is higher. In this case the accuracy dominates the precision and it is senseless the comparison of the method performances in precision. An accuracy estimation analysis is needed (see section 4.3), where over a certain number of noise realizations the accuracy of both the methods is evaluated. The red and yellow lines are close to the limit case and it corresponds to a SNR value between 50dB and 40dB, respectively. Therefore, below the limit SNR value (black dotted line), the precision estimation is useless and the accuracy must be investigated.

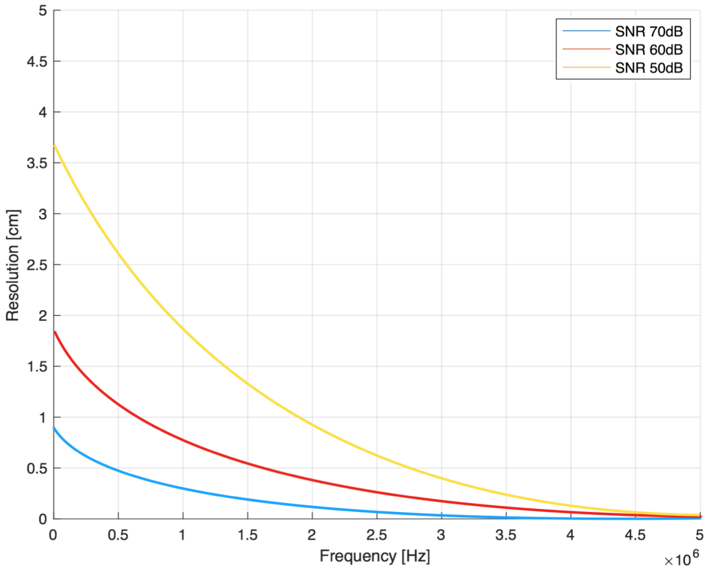

Figure 4-11: Spatial resolution in Port MUSIC considering three different SNR values: 70dB (blue), 60dB (red) and 50dB (yellow)

Accordingly, three different SNR values higher than the limit case are considered for the precision estimation: 50dB (yellow), 60dB (red) and 70dB (blue). The resulting plot considering all the frequency samples is shown in figure 4-11. Comparing this result with the TDR case the super resolution advantages of MUSIC are evident where, for the three cases considered, the spatial resolution is on the millimeter/centimeter order. Taking into account for example a single frequency sample, (*i.e. 4MHz at 60dB*), the correspondent peak resulting from the vector projection is shown in figure 4-12 and the super resolution of 1.4mm is obtained, decreasing the maximum peak by 3dB as done for TDR. For lower SNR values, MUSIC still performs super resolution on the order of the centimeter but the study have not been done for the reasons explained before.

A study of accuracy will be shown in the next section involving these SNR values. In such a case, also the peak amplitude decreases since a noise term is added, as shown in the equation 4.13, and the projection is not perfect as in the noiseless case, where the peak amplitude tends to infinite.

4.3 Accuracy Estimation

In this section the uncertainty about the fault position is investigated in both TDR and Port MUSIC. In order to perform it a noisy case is taken into account, with 20dB of SNR, chosen according to the study done in the previous section. A certain number of noise realizations are considered and a Monte Carlo simulation is applied in order to estimate the accuracy of the different methods.

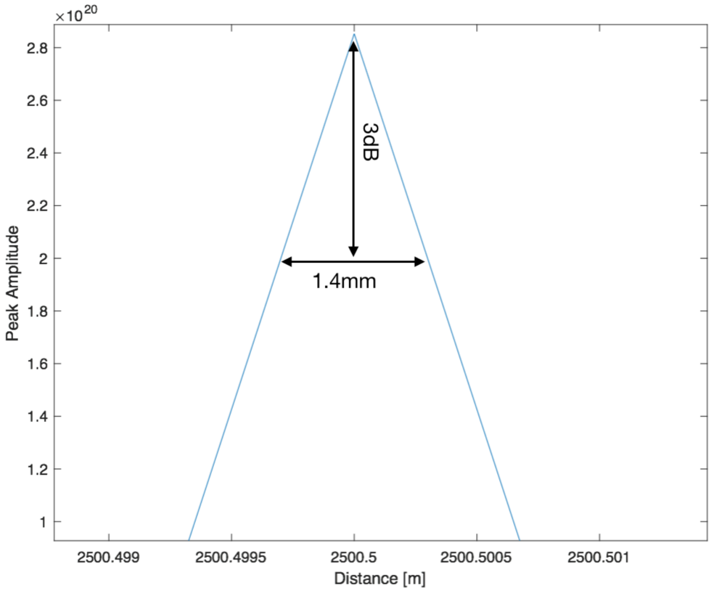

Figure 4-12: Peak resulting from the MUSIC projection procedure, at 4MHz and 60dB of SNR

TDR

Uncertainty is investigated by studying the standard deviation of each method and a consequent histogram is figured out. For TDR the reflectogram is shown (figure 4.13(a)), where it is evident the presence of 20dB SNR: the noise level is not so high due to the definition given to SNR in this work. In fact, as stated in section 4.1, it has been defined in frequency and as consequence of the mean operation carried out in frequency-domain, the noise level will be lower in time-domain. Running a Monte Carlo simulation with 100 noise realizations the resulting histogram identifying the fault position is shown in figure 4.13(b), where a quite good standard deviation σ is obtained.

Port MUSIC

In this case it is not immediate the procedure for computing the accuracy of the method. In fact, at each realization a counting of the fault candidates at the different frequencies is carried out and the position with the greatest number of candidates is identified as fault position. If the line is noiseless, in the exact fault position there is no displacement and all the frequencies find a peak at that position, as observed in figure 4.6(b). But in presence of noise (above all for low SNR values, i.e. 20dB) more candidates around the fault position occur and errors can be arisen. This procedure for which MUSIC locates the fault considering the maximum peak over the fault candidates is called *majority law*. It is the basic procedure and its operational mode is shown in figure 4-14. Considering a single realization, if the exact fault position is the blue one (4.14(a)) no errors arise.

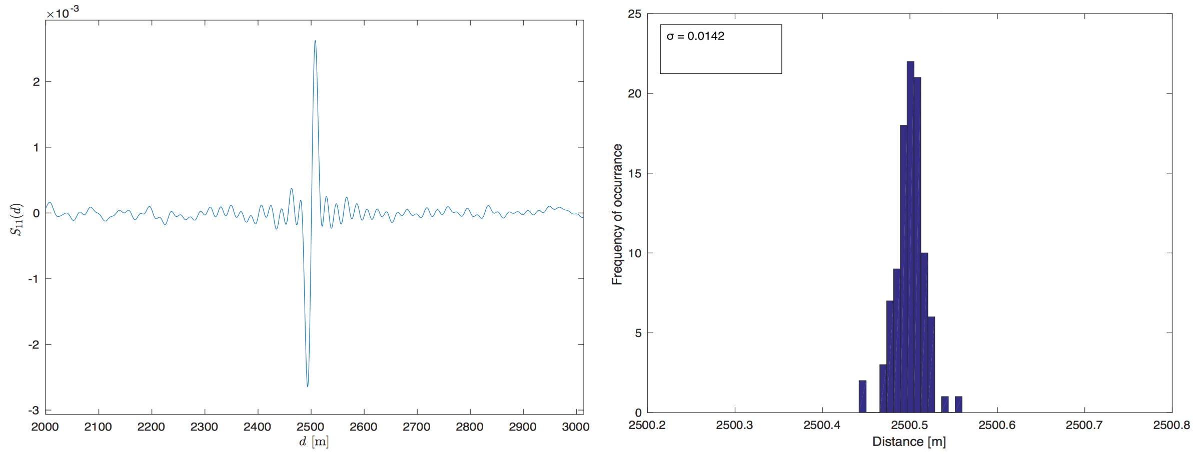

(a) *Reflectogram with SNR=20dB* (b) *TDR histogram*

Figure 4-13: Monte Carlo simulation results in TDR with 100 noise realizations and 1000 frequency samples

But in presence of noise the maximum peak can indicate a different position, bringing to errors in the location (4.14(b)). As a result, the histogram in figure 4.15(a) is obtained with a σ much higher than the TDR case.

In order to improve the problems arisen with the majority law, a second procedure is introduced: the smooth function. It operates considering the number of local peaks at different positions as the majority law, but it works with a convolution operation. In particular, a moving window is considered and the local peaks included in its area are convoluted together: in other words, it is nothing else than a low-pass filter. The accuracy is improved with respect to majority law ($\sigma = 0.039$) but the precision is worse since a region of space is considered and not singular peaks (figure 4.15(b)). Obviously, another consideration to be done is the choice of the width of the moving area. In the considered example, 7 position points are considered and included in the moving window: increasing it, accuracy improves but precision deteriorate. With 3 position points, for

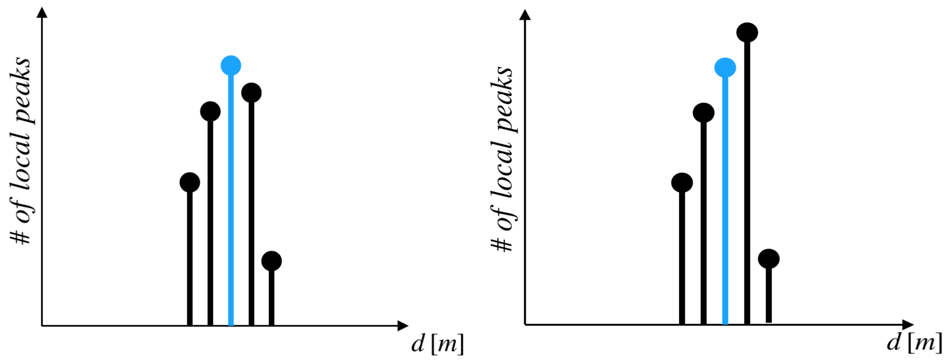

(a) (b)

Figure 4-14: Majority law procedure in Port MUSIC

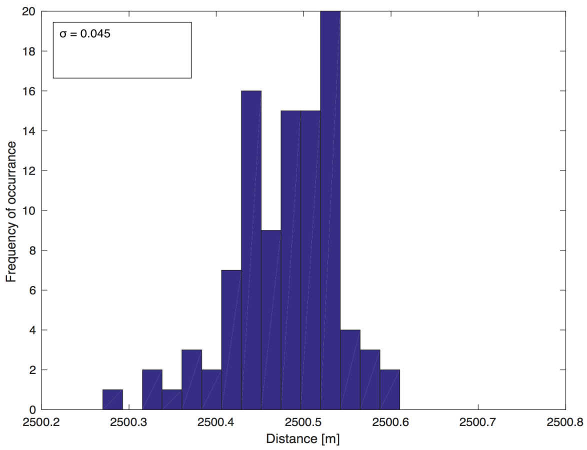

(a) *Majority law* (b) *Smooth function*

Figure 4-15: Port MUSIC histograms with 100 noise realizations and 1000 frequency samples

example, σ is 0.048 while with 15 position point 0.035. The choice of 7 point positions is a good compromise between precision and accuracy estimation (figure 4-16).

However, also considering the smooth procedure σ is still higher than the TDR case, and a new procedure shall be implemented to improve the performances. With this in mind, a third procedure for the accuracy estimation in Port MUSIC is developed: *DB-Scan function*. It operates in different region of the two-dimensional space frequency-distance (the space created by the Pseudo-spectrum function), through a "*cluster analysis* ". A maximum distance is chosen, the reference distance d_{ref}, and σ is computed considering only the points for which d $< d_{ref}$, where d is the distance between the samples. Different clusters are generated in the space and only the fault candidates close to the exact fault position are included in the accuracy estimation. Since MUSIC operates at independent frequencies, the exclusion of certain frequency samples is possible and advantages in accuracy estimation are expected. Considering always 10MHz as maximum

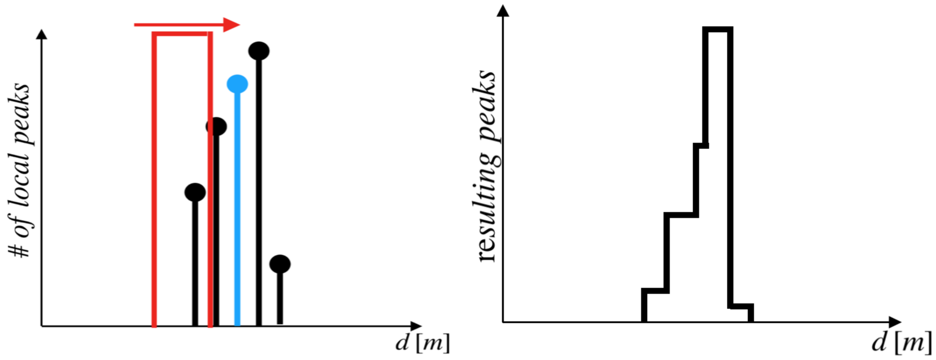

(a) *Moving window* (b) *Resulting peaks*

Figure 4-16: Smooth function procedure in Port MUSIC

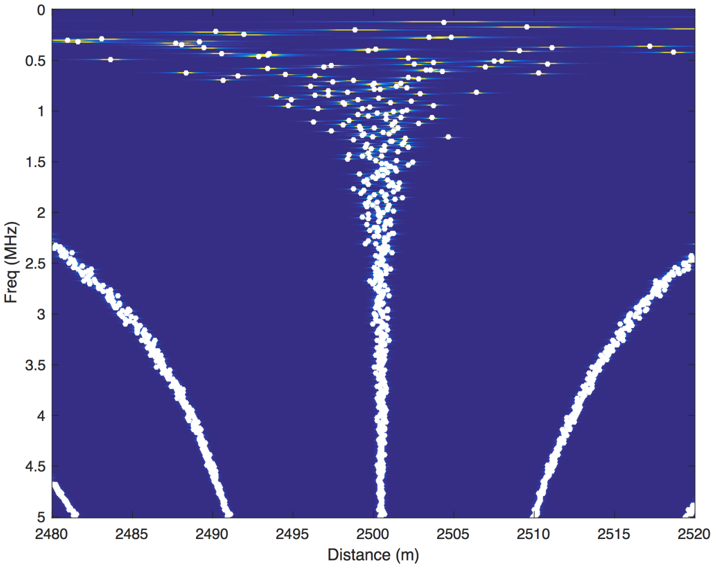

Figure 4-17: DB-Scan procedure where $d_{ref} > 9.51$m is considered and different clusters are generated involving also the *ghosts*

frequency in baseband a $d_{ref} < 9.51$m must be chosen. The reason of this choice is related to the presence of *ghosts*. In fact, the ghosts are distanced from each other and from the fault position by $\frac{\lambda}{4}$ and, obviously, at high frequencies this distance decreases. Different clusters are created where clouds of points are figured out in space, as represented in figure 4-17 by white points: thus, d_{ref} must be lower than $\frac{\lambda_{5MHz}}{4}$, which corresponds to 9.51m.

Moreover, the central cluster must be taken into account (the one within the fault) and for this purpose the *maximum kurtosis* is evaluated. The kurtosis is an index which measures how much a distribution is smooth evaluating how much the samples are spread in a particular distribution. In statistics and metrology it is common as the *4th* moment and in the similar way of skewness (*3rd* moment), kurtosis is a descriptor of the shape of a probability distribution. The way in which kurtosis can be expressed is the "*kurtosis index*":

$$\gamma = \beta - 3, \tag{4.14}$$

where β is the ratio between the fourth central moment μ and the square variance:

$$\beta \triangleq \frac{\mu^4}{\sigma^4} = \frac{E[(x_i - \mu)^4]}{(E[(x_i - \mu)^2])^2}, \tag{4.15}$$

with x_i a particular point in the Pseudo-spectrum space. Looking for the maximum, the cluster with less dispersion between its samples is obtained. In fact,

if $\gamma < 0$	the distribution is "leptokurtic", smoother than a Gaussian distribution;
if $\gamma = 0$	the distribution is "mesokurtic", smooth as a Gaussian distribution;

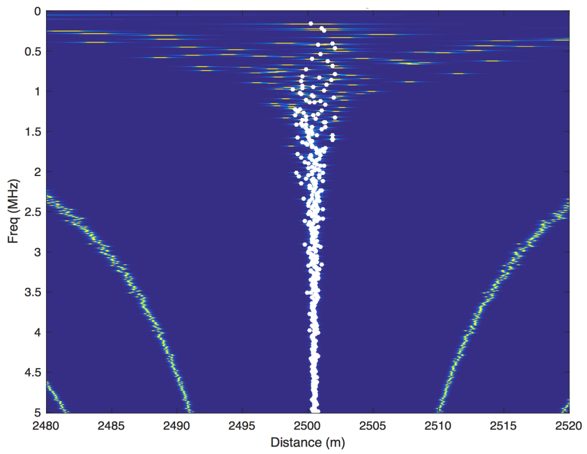

(a) $d_{ref} = 2.37m$ (b) $d_{ref} = 1.58m$

Figure 4-18: Pseudo-spectra in which DB-Scan is applied

if $\gamma > 0$ the distribution is "platykurtic", sharper than a Gaussian distribution.

Computing the maximum kurtosis the central cluster is considered since it is the one with less dispersion between its samples. Implementing DB-Scan, less frequency samples are taken into account and, in order to equally compare the results with TDR, a greater initial number of frequency samples are considered in such a way to obtain 1000 frequency samples for which d $< d_{ref}$ is verified.

The accuracy of Port MUSIC operating with DB-Scan is evaluated by considering two different cases of d_{ref}: 2.37m and 1.58m, corresponding to $\frac{1}{4}$ and $\frac{1}{6}$ of $\frac{\lambda_{5MHz}}{4}$, respectively. The Pseudo-spectra are shown in figure 4-18, where it is evident the low frequencies exclusion operated by this operational function. The improvement in accuracy results in

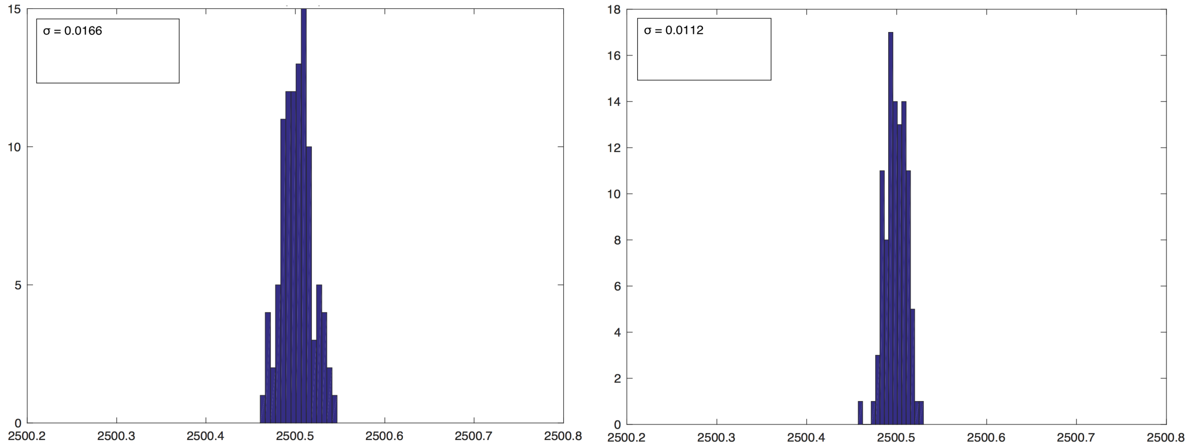

(a) $d_{ref} = 2.37m$ (b) $d_{ref} = 1.58m$

Figure 4-19: Histograms in which DB-Scan is applied

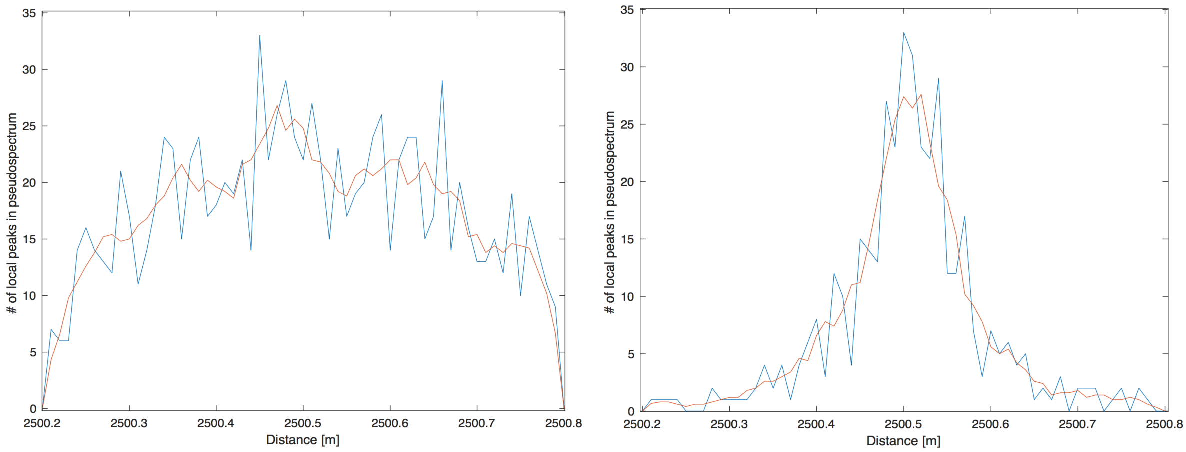

(a) *Majority law* (b) *DB-Scan with* $d_{ref} = 2.37m$

Figure 4-20: Accuracy estimation in frequency counter

the histograms figured out in 4-19. Less d_{ref} is, better accuracy is performed. However, taking lower d_{ref} values brings to the exclusions of an higher number of frequencies, making the results not so reliable. Again, a compromise between these two effects shall be considered and for this purpose the $\frac{\lambda_{5MHz}}{16}$ (4.18(a)) is considered in our simulations. The correspondent σ value ($= 0.0166$), shown in figure 4.19(a), verifies the accuracy improvement of Port MUSIC adopting DB-Scan and comparing it with majority law the result is evident. The frequency counter plots are shown (4-20) where a sharper behavior in DB-Scan (4.20(b)) results in a better σ estimation.

In conclusion, the accuracy between TDR and Port MUSIC are comparable when DB-Scan is adopted. What it is interesting to observe now is the behavior of these methods in the accuracy estimation when the number of frequency samples and the bandwidth change. From now on, TDR and Port MUSIC will be compared considering the only DB-Scan procedure with $d_{ref} = \frac{\lambda_{5MHz}}{16}$.

4.3.1 Parametric Study

In the previous sections the simulations have been carried out considering f_{max}=10MHz and 1000 samples. Now, the influence of these parameters variation and how the methods' performances are modified is studied. Besides, the influence of noise and the change of fault position is analyzed too and the accuracy results evaluated.

Number of Frequency Samples

A 10MHz of maximum frequency is considered with a different number of frequency samples. The accuracy estimation of both TDR and Port MUSIC is studied. The cases of 5000 and 10000 frequency samples are considered and compared to the previous case

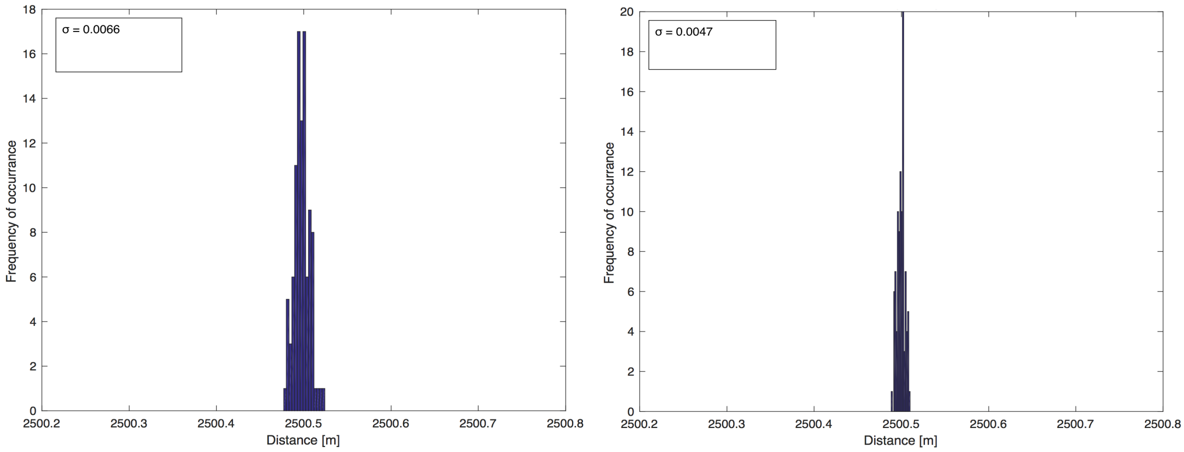

(a) m = *5000* (b) m = *10000*

Figure 4-21: TDR histograms with different frequency samples m

with m=1000. Increasing the total number of frequency samples m, an improvement in accuracy is expected for both the methods since a better mean operation is carried out.

For TDR, the histograms shown in figure 4-21 effectively figure out the expected behavior, with a decrease of σ increasing the number m of frequency samples. A very interesting thing to note is the behavior of σ: in fact, it decreases proportionally to $\sqrt{m}$, according to the central limit theorem. It can be easily verified considering the mathematical model of TDR: in this case, in fact, the variance of all the m samples is invariant and thus *CLT* can be applied:

$$\sigma^2 = \frac{1}{m^2}\sum_{j=1}^{m}\sigma_j^2 = \frac{1}{m}. \tag{4.16}$$

Also in Port MUSIC an higher number of frequency samples results in a better accuracy estimation. In fact, more samples are included in the central cluster with maximum kurtosis and consequently, over a certain number of noise realizations, the accuracy improves. A mathematical model is introduced, assuming that all the samples are distributed as a Gaussian distribution, in order to study the variation of σ changing m. Considering two arbitrarily values of f_{min} and f_{max} and their samples m_{min} and m_{max}, the deviations are related as follows:

$$\sigma_{max} = \sigma_{min}\frac{f_{min}}{f_{max}} = \frac{\sigma_0}{f_{max}}, \tag{4.17}$$

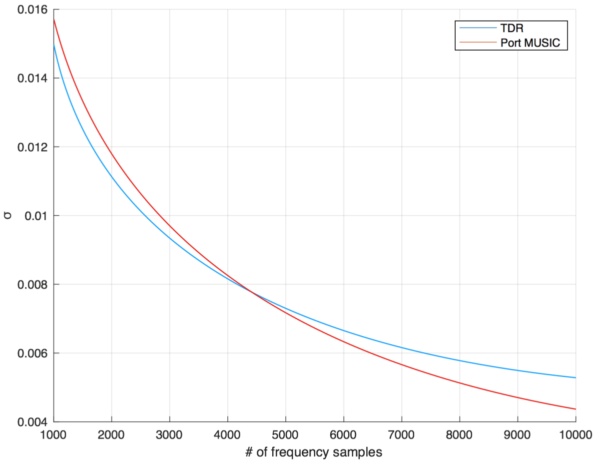

Figure 4-22: Behavior of σ in function of the number of frequency samples both for TDR (blue) and Port MUSIC (red)

where σ_0 is referred to the reference frequency f_{min}. The equivalent variance is given by:

$$\sigma_{eq}^2 = \frac{1}{m^2}\sum_{j=m_{min}}^{m_{max}} \sigma_j^2 = \frac{1}{(m_{max}-m_{min})^2}\sigma_0^2 \sum_{j=m_{min}}^{m_{max}} \frac{1}{j^2}. \tag{4.18}$$

Applying the *Euler-Maclaurin* formula,

$$\sum_{j=m_{min}}^{m_{max}} \frac{1}{j^2} = (m_{max}-m_{min}) \int\limits_{m_{min}}^{m_{max}} \frac{1}{j^2} = -\frac{m}{j}, \tag{4.19}$$

we can obtain

$$\frac{\sigma_{eq}^2}{\sigma_0^2} = \frac{1}{m_{min}m_{max}} = \frac{1}{m_{min}^2(1+\frac{m}{m_{min}})}, \tag{4.20}$$

and if m » m_{min}

$$\frac{\sigma_{eq}^2}{\sigma_0^2} \approx \frac{1}{m}. \tag{4.21}$$

Therefore, also Port MUSIC follows the CLT varying the number of frequency samples m and the behavior of σ is very similar to TDR, as shown in figure 4-22.

Maximum Frequency

A 100MHz of maximum frequency is now considered with 1000 frequency samples and its influence on the methods' performances studied with 20dB of SNR. Intuitively, also in this case an improvement in accuracy is expected.

For TDR the explanation derives directly from the Fourier theory since increasing the frequency bandwidth, a compression in time-domain occurs. It is figured out in the

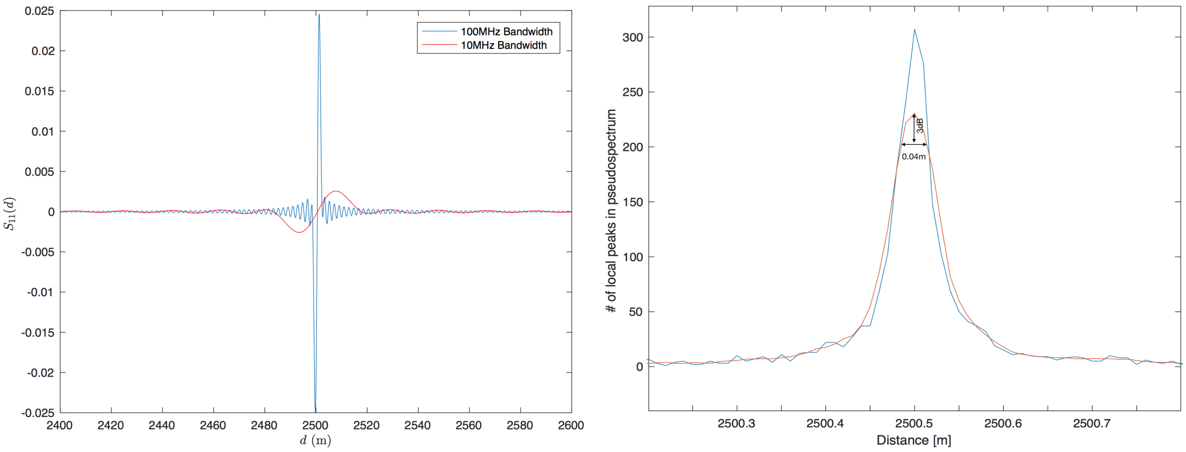

(a) *TDR- Reflectogram*

(b) *Port MUSIC - Frequency counter*

Figure 4-23: Results with 100MHz of maximum frequency and 1000 frequency samples

reflectogram of figure 4.23(a), where for the blue peak (100MHz) a better accuracy in fault location is evident with respect to the red one (10MHz): beside, it is interesting to observe that the blue peak is 10 times higher than the red one due to the proportional relationship between Γ_f and ω (see equation 4.5). This compression in time-domain performs benefits also in the precision estimation since a better spatial resolution is obtained. In case of $f_{max} = 100MHz$, 2.2m of resolution is obtained (figure 4.24(a)) and increasing more the bandwidth a significant improvement is verified. However, as shown in figure 4.24(b), in order to obtain a resolution of the *cm* or *mm* order performed in MUSIC very high bandwidths must be taken into account ($10 \div 100GHz$), which are not always available especially in presence of losses.

Intuitively, increasing the maximum frequency in MUSIC an improvement in accuracy occurs since an higher number of high frequencies are involved and the equivalent spread decreases. Consequently, an higher number of frequency samples are detected by the frequency counter around the fault position and the *effective* spatial resolution improves (figure 4.23(b)), from 0.09m when $f_{max} = 10MHz$ to 0.04m.

As a matter of fact, both for TDR and MUSIC the σ have been computed through a Monte Carlo simulation, resulting 0.00062 and 0.00084 respectively.

SNR

Until now a 20dB value of SNR has been chosen in order to evaluate the accuracy with a significant noise value. In this section, a statistical analysis is carried out by considering a varying SNR in the range from 40dB to 0dB, all values below the limit case, and the accuracy estimated. In fact, this is the range at which the accuracy dominates on the precision: it is better shown in figure 4-26, where at different SNR values the peaks

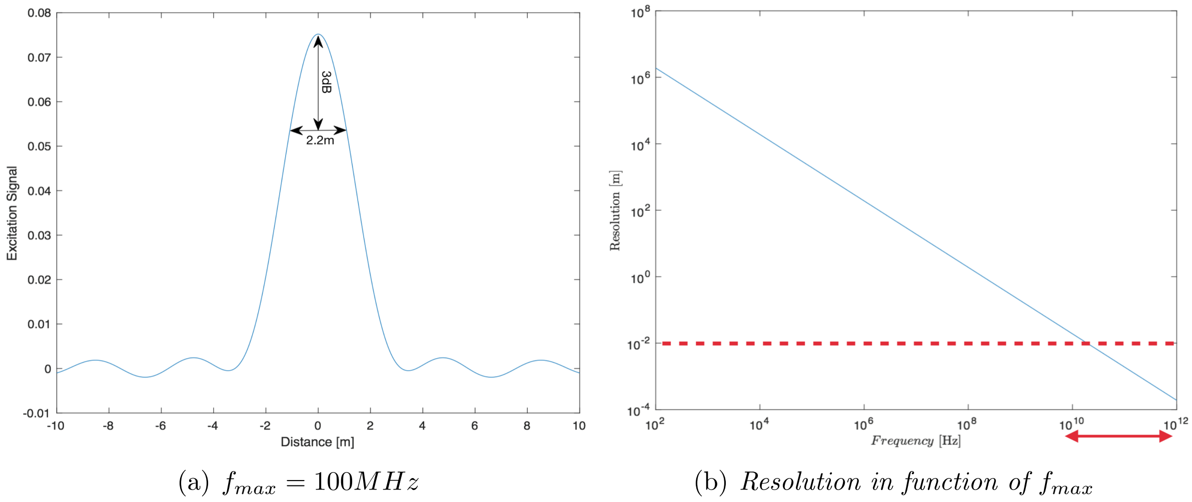

(a) $f_{max} = 100MHz$ (b) *Resolution in function of* f_{max}

Figure 4-24: TDR spatial resolution

obtained by $\Phi(x)$ are figured out. For SNR values higher than the limit case (>40dB), a very small range of positions is involved in the fault location: in particular, it is lower than the spatial resolution observed at that specified frequency ($\approx mm$) and consequently accuracy is dominated by precision. Instead, for SNR values going from 40dB to 0dB the fault is located in a wider range of position, higher than the spatial resolution at that specified frequency. As a result, σ deteriorates decreasing the SNR value. A metrological study using the *cumulative density function* is carried out in order to better analyze the effects of SNR. Three different values are taken into account and the CDF figured out (figure 4-27): as shown, the noise robustness is more or less the same for TDR and MUSIC. Beside, as expected σ gets worse decreasing the SNR value. To quantify the variation of the estimated fault's position for a given SNR, its mean value is observed along with its upper and lower bound estimates. A 95% confidence interval is considered, i.e. the significance level is set to 0.05 where the lower and upper bound estimates are taken at 2.5% and 97.5% of the CDF corresponding to the studied network at a predefined SNR, as shown in figure 4-28 considering the CDF at 0dB.

In this section the noise influence is investigated, showing that the performances of the two methods are very similar with very good results (figure 4.29(a) and 4.29(b)). It is interesting now to compare the noise robustness of Port MUSIC with the standard MUSIC method. From the theory, the new concept of Inverted MUSIC has been introduced since, ideally, should be more robust in presence of noise due to the fact that the projection operation does not involve the noise subspace $\mathcal{N}$ but real measured quantities (see section 3.4.2). In order to verify it, the CDF of the upper, mean and lower values analysis is done also for the standard version of MUSIC and the results compared. As expected and shown in figure 4.29(c), at the same conditions of Inverted Port-MUSIC and with same

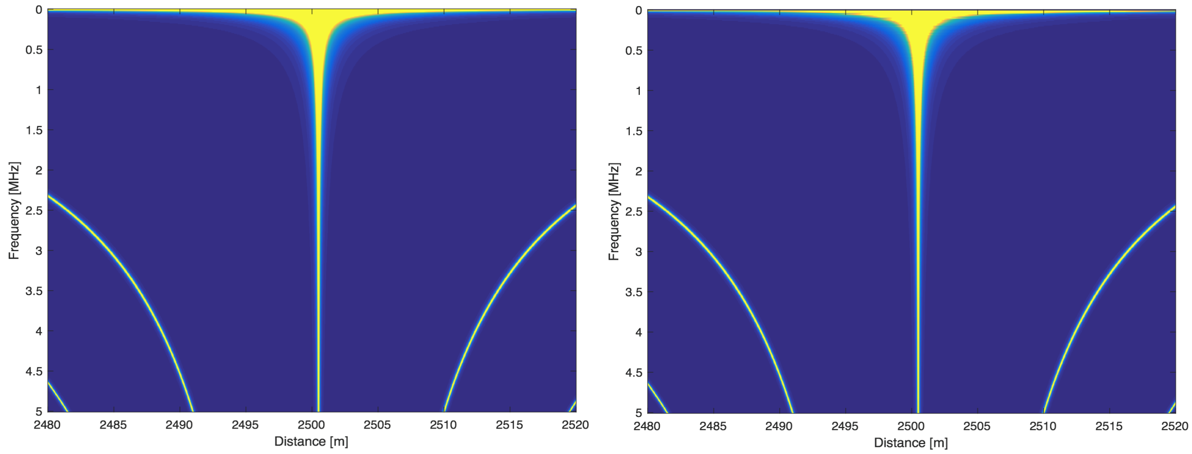

(a) *Noiseless* (b) *SNR 80dB*

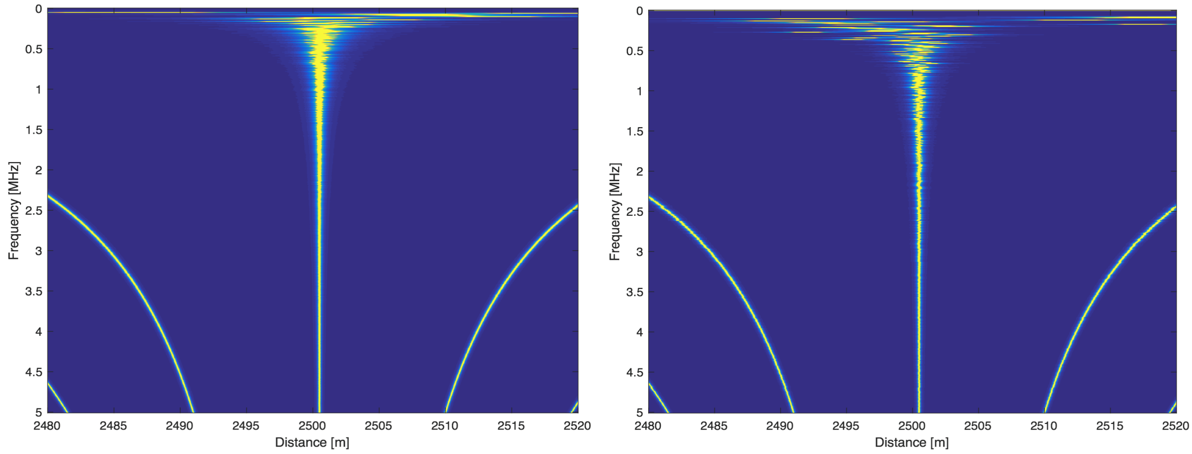

(c) *SNR 50dB* (d) *SNR 40dB*

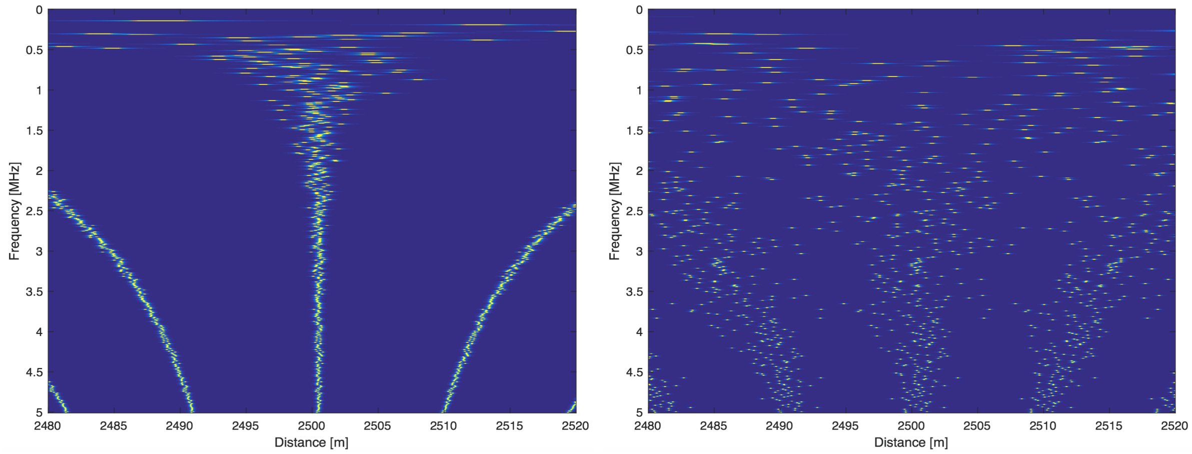

(e) *SNR 20dB* (f) *SNR 0dB*

Figure 4-25: Pseudo-spectra $\Phi(x)$ at different SNR values

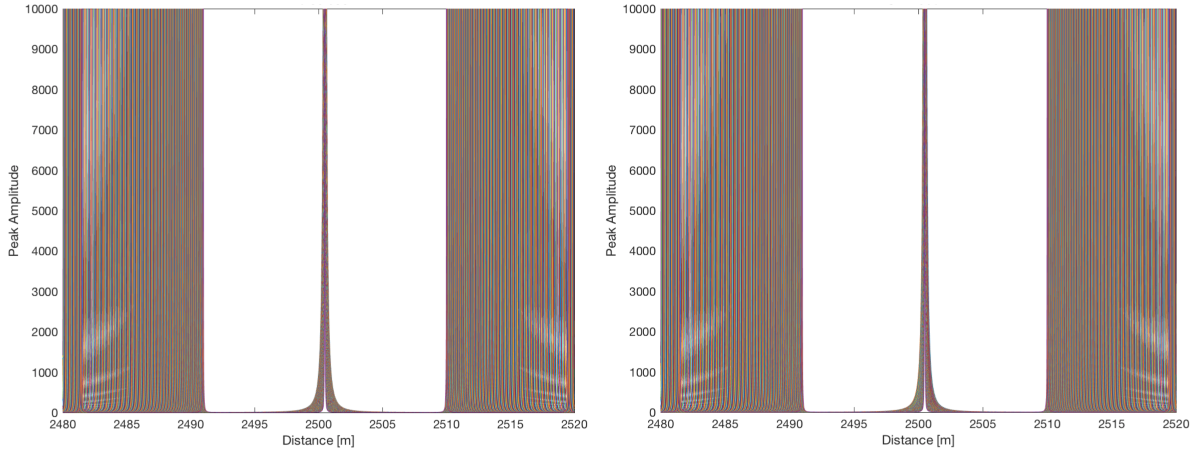

(a) *Noiseless*　(b) *SNR 80dB*

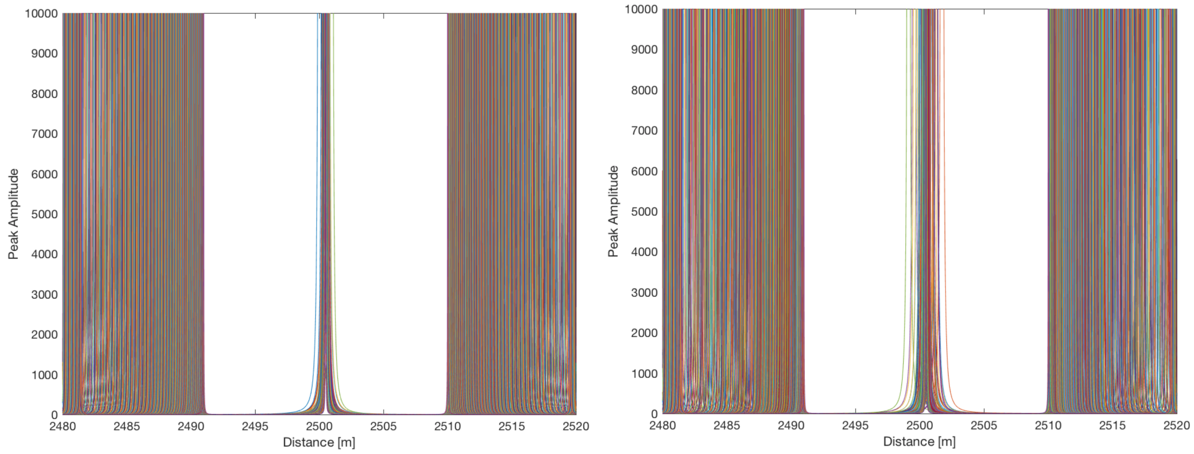

(c) *SNR 50dB*　(d) *SNR 40dB*

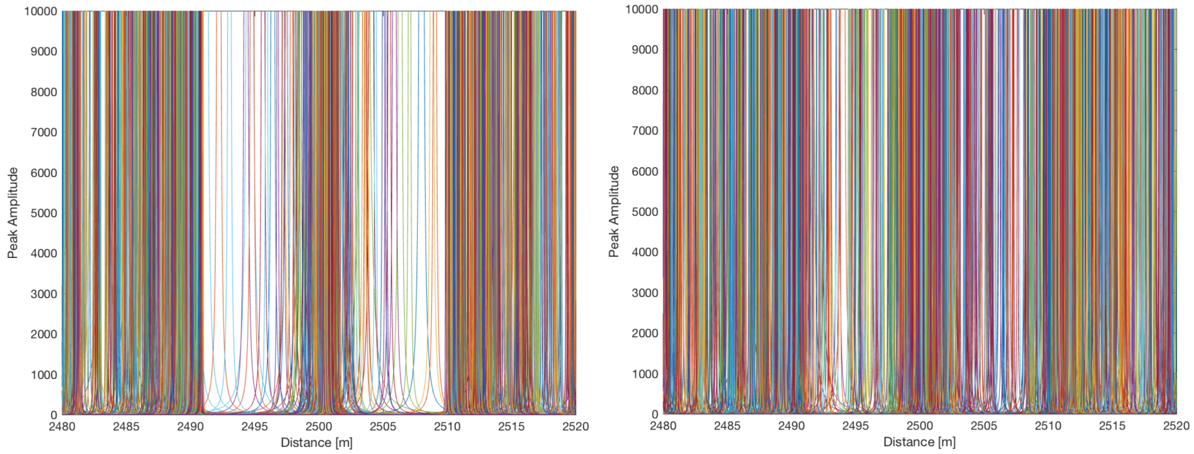

(e) *SNR 20dB*　(f) *SNR 0dB*

Figure 4-26: Peaks detected by $\Phi(x)$ at different SNR values

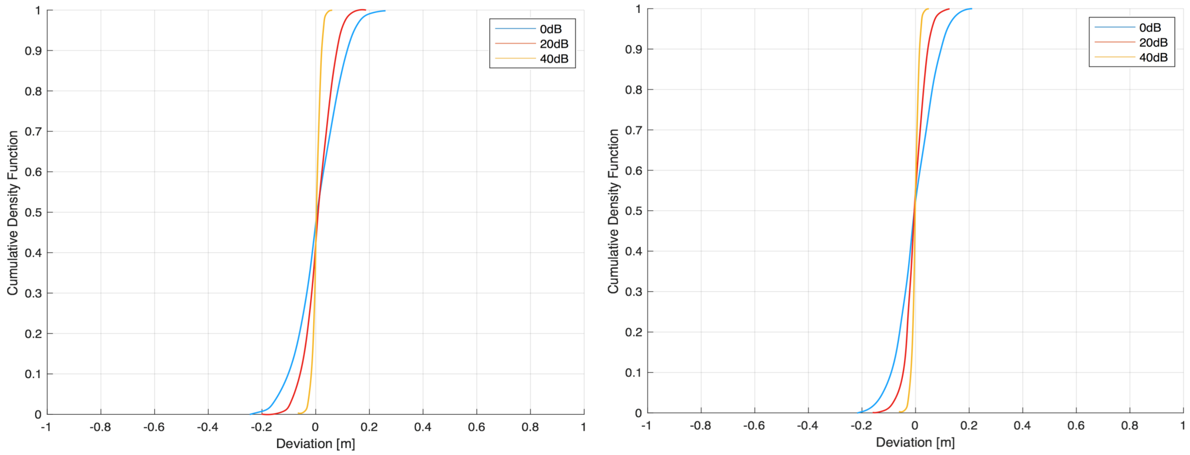

(a) *TDR*

(b) *Port MUSIC*

Figure 4-27: Cumulative density function at three different SNR values: 40dB (yellow), 20dB (red) and 0dB (blue)

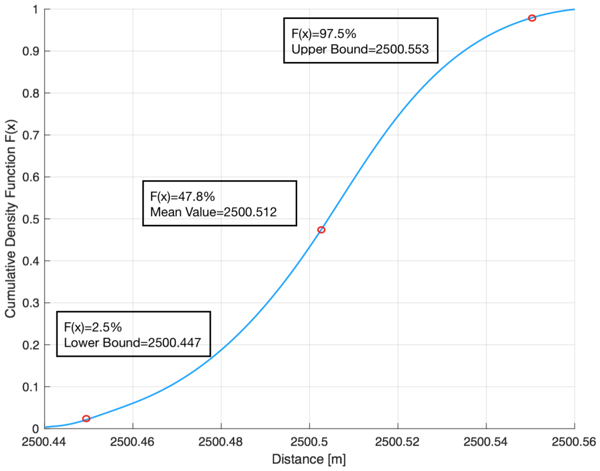

Figure 4-28: CDF of the deviation of the faults' s position for an SNR value of 0 dB

DB-Scan tools adopted, standard MUSIC is more influenced by noise with an higher σ for different SNR values.

Fault Position

In this section, we are going to see what happens if the fault position changes considering the fault at 7.5km from the first testing port, always over a 10km line length. Actually, the line is lossless and therefore it is easy to think that the fault position shall not influence the results. In fact, no losses are present on the line and consequently no attenuation is present. As seen in chapter 2 through the relationships between attenuation and fault position over a line, without attenuation there is no limitation in frequency and, thus, the performances of the methods are not influenced by the fault position.

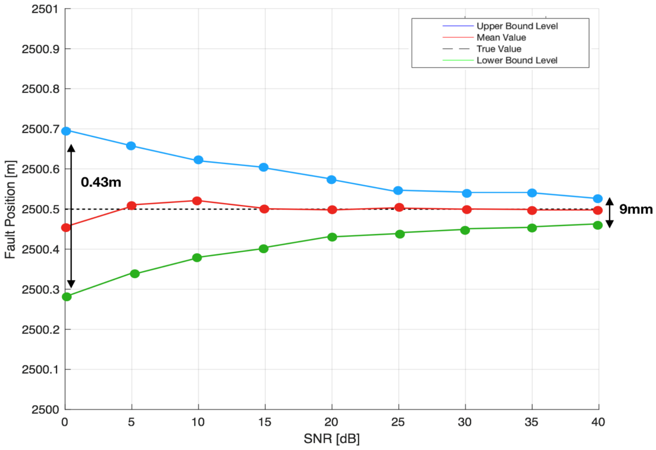

(a) *TDR*

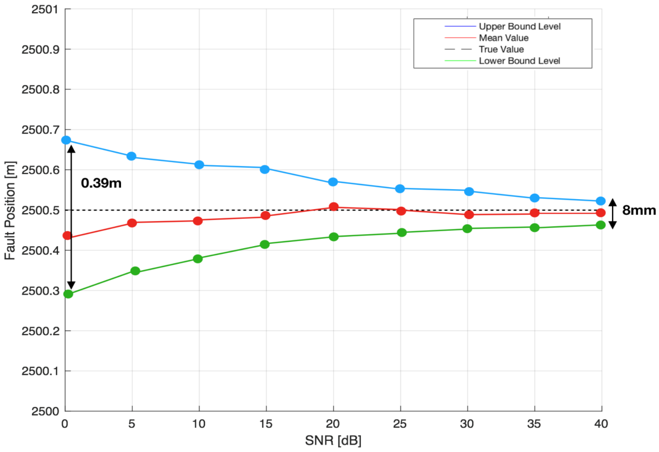

(b) *Port MUSIC*

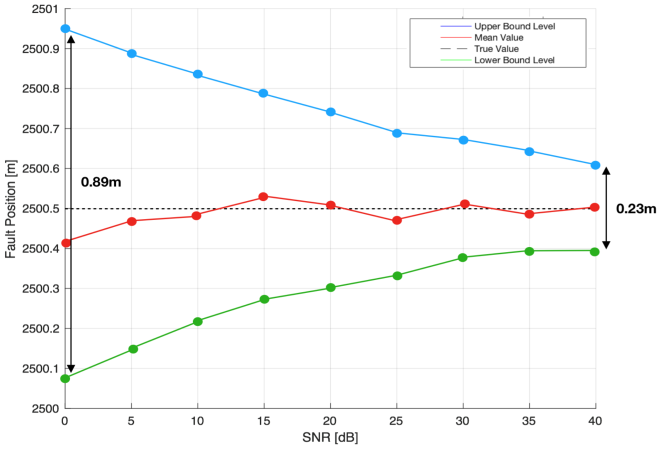

(c) *Standard MUSIC*

Figure 4-29: CDF with upper, mean and lower value and true value

This is not true when a lossy line case is studied, since at each fault position corresponds a different value of maximum frequency. In this section a simple computation with the fault at 7.5km from the testing port *(1)* is reported, with the only goal to verify that it does not influence the performances of the methods and as introduction to the lossy line case. Sampling with 1000 frequency samples and 10MHz of f_{max} at 20dB of SNR, the resulting σ are 0.0147 and 0.0116 for TDR and MUSIC, respectively, proving that the fault position does not affect the results.

4.4 Summary

In this chapter, a single lossless line has been studied. The precision and accuracy of TDR and Port MUSIC have been evaluated in function of SNR, which plays a very important role in such estimation analysis. In particular, for high SNR values the precision estimation is carried out whereas the accuracy estimation for low SNR.

The super resolution of MUSIC ensures great advantages with respect to TDR, above all in case of frequency limitations. Beside, the methods show very similar results in accuracy: at this purpose, different MUSIC accuracy estimation procedures have been presented, where DB-Scan has performed very interesting results.

In conclusion, it is possible to state and observe the advantages of Port MUSIC with respect to TDR, with the same accuracy results and a much higher precision in the fault location. The price to be paid is the necessity of using all the available ports, but according to CLT it would show anyway advantages with respect to TDR with the same number of injecting ports. The study of a lossy line illustrated in the next chapter will result very interesting since attenuation and dispersion are introduced, causing limitations in frequency.

Chapter 5

Soft Fault Location in a Single Lossy Line

THE analysis of a lossy line and the effects of attenuation and dispersion on the fault location method are studied in this chapter. The NUT considered is the one introduced in chapter 2 (10km with 1m-fault), and the relationships found out between attenuation and losses of the cable are recalled. 10MHz of f_{max} is still considered but due to attenuation some frequency limitations are presented. 1000 frequency samples and the noiseless case are studied both for TDR and Port MUSIC.

Two different types of fault are considered in the analysis: firstly, the fault is represented by a portion of line with a different conductance with respect to the remaining part of the line, while *R=0* for the entire line ("*G fault* "). In such case, for TDR a numerical validation of the model is introduced and verified with *CST MWS*. Then, for the entire line $R \neq 0$ and $G \neq 0$, and the fault is represented, as in chapter 4, by an impedance discontinuity ("*Z fault* "). In this case it is no more a "conductance fault" but is given by $Z_f \neq Z_c$.

In the last section of the chapter an experimental validation of Port MUSIC is implemented, adopting the Vector Network Analyzer (VNA) in Supélec facilities.

5.1 G Fault

The fault is considered here as a piece of lossy line where the conductance is different from the remaining part of the line. These kinds of faults are very common in real cables given, for example, by the excessive moisture upon the cable or a water penetration. Such effects are going to modify the value of tanδ of the involved portion of line and consequently a change in the value of G occurs. In particular, as shown in figure 5-1, for the healthy line tanδ is $5 \cdot 10^{-4}$ while $5 \cdot 10^{-3}$ for the fault (table 2-1). Both the characteristic impedances

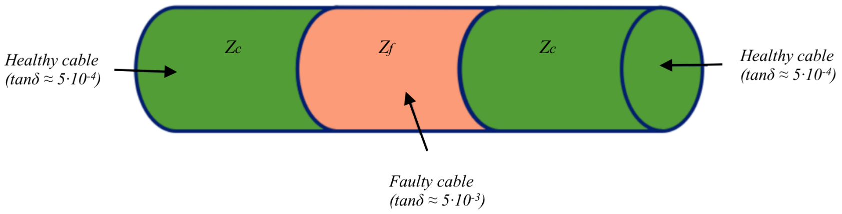

Figure 5-1: Transmission line with a different conductance fault

of the healthy and the faulty lines are complex numbers changing with frequency, with different value of G:

$$Z_c = \sqrt{\frac{j\omega L}{G_c + j\omega C}}, \tag{5.1}$$

$$Z_f = \sqrt{\frac{j\omega L}{G_f + j\omega C}}, \tag{5.2}$$

where G_c and G_f are the conductances of the healty and faulty line, respectively. Computing the value of Γ_0, starting from the equations 5.1 and 5.2,

$$\Gamma_0 = j\frac{tan\delta}{4} \tag{5.3}$$

is obtained, where it is possible to note that it is no more a real number but an imaginary one. Substituting it in the equation 4.5, we obtain:

$$\Gamma_f = -\omega\frac{w}{v}\frac{tan\delta}{2}e^{-j\beta w}. \tag{5.4}$$

MUSIC shows the same results as the lossless line case (see chapter 4). In fact, it operates on phase patterns only and thus is not influenced on the fault topology. This is due to the fact that in Port MUSIC a normalization procedure is applied and since Γ_0 is out of phase no phase distortion is verified. The only difference with respect to the lossless case is the composition of $\underline{v}_1$ since now Γ_0 is a complex term, and each term of $\underline{v}_1$ is given by:

$$\frac{S_{ii}}{|S_{ii}|} = e^{-j2\omega\tau_i}. \tag{5.5}$$

Interesting results involving instead TDR: in this case, the time-domain reflected wave has no more the derivative shape since the term j is deleted by Γ_0. Investigations about its shape are developed in this section, first in Matlab and then numerically verified in *CST MWS*. The fault in the reflectogram is now detected by the minimum peak, as shown in figure 5-2. It corresponds to the minus sign of equation 5.4. Besides, Γ_f depends on tanδ: in figure, two values of tanδ are shown ($5{\cdot}10^{-3}$ in blue and 0.01 in red) where it is

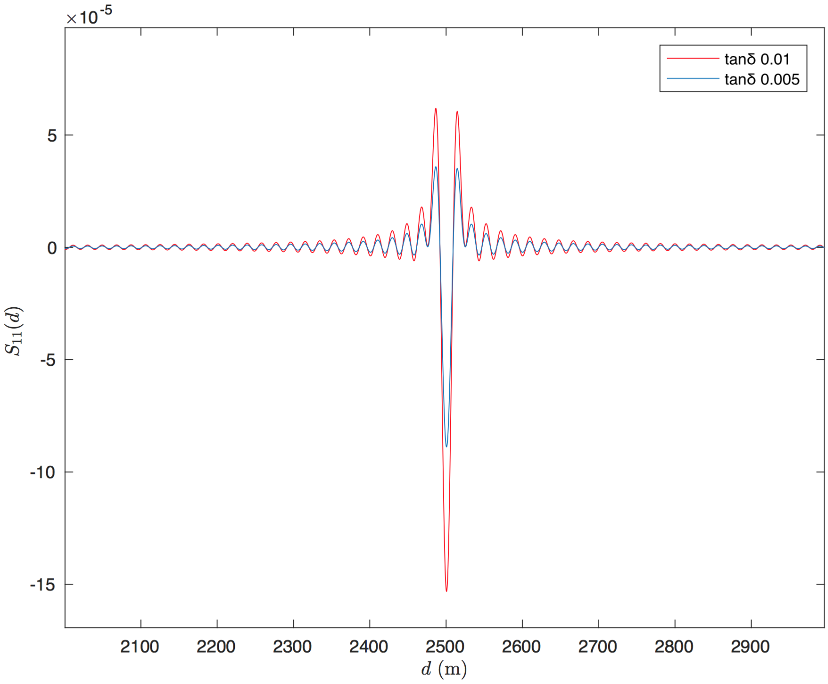

Figure 5-2: Reflectogram in case of G fault with two different tanδ values: $5{\cdot}10^{-3}$ in blue and 0.01 in red

possible to observe that for low values of tanδ the reflected wave could not be seen.

In order to numerical validate the Γ_0 model of equation 5.4, the CST software Microwave Studio has been adopted where the cable structure is the same as the one studied. Three cable portions are built, the ones at the extremes representing the healthy lines and the one in the middle representing the faulty line. The dielectric considered is the XLPE, with the same tanδ value considered in Matlab for the healthy lines and a 0.01 constant value (predefined value of lossy XLPE offered by the software) for the fault. A PEC (Perfect Electrical Conductors) model is adopted for the inner and outer conductors. The structure of the cable built with MWS is shown in figure 5-3, where a cutting along the z plane figures out the three different layers of the cable (in gray the conductors and in white the dielectric). Beside, a cutting along the x plane shows the different conductance in the faulty and healthy sections, respectively in green and red. A port mode is adopted for the simulations in order to chose the directions of the electric and magnetic fields: *TEM* mode (*mode=1*) has been selected, where the waves propagating along these lines are characterized by electric and magnetic fields entirely transverse to the direction of propagation, as represented in figure 5-4. The *CST* simulations are aimed to validate the numerical results obtained with the model of a 10km power cable. The faulty line length considered is still *1m* but, in order not to make too heavy the computations only a very small portion of the 5km health lines is considered (*1m* or *1.5m*) depending on the considered case: the result is not influenced on this changes since we are interested in

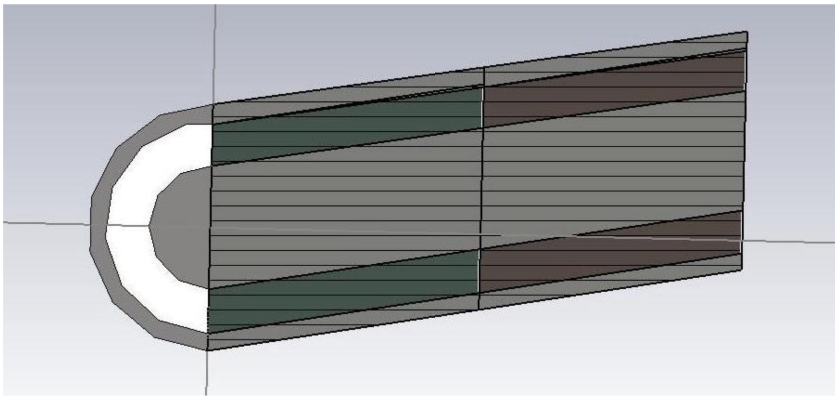

Figure 5-3: Cable structure with *CST* where dielectric of faulty (green) and healthy (red) line sections are shown

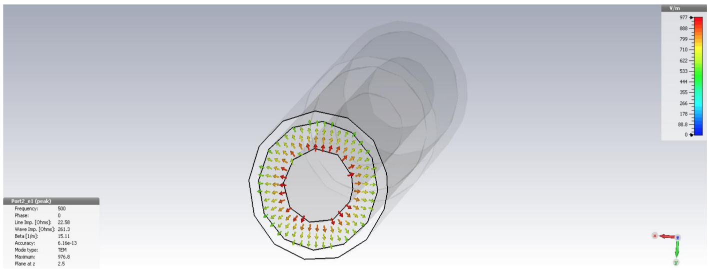

Port2_e1 (peak)
Frequency: 500
Phase: 0
Line Imp. [Ohms]: 22.58
Wave Imp. [Ohms]: 261.3
Beta [1/m]: 15.11
Accuracy: 6.16e-13
Mode type: TEM
Maximum: 976.8
Plane at z 2.5

(a) *Electric field*

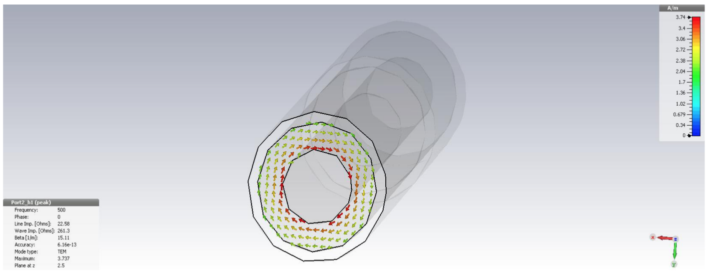

Port2_h1 (peak)
Frequency: 500
Phase: 0
Line Imp. [Ohms]: 22.58
Wave Imp. [Ohms]: 261.3
Beta [1/m]: 15.11
Accuracy: 6.16e-13
Mode type: TEM
Maximum: 3.737
Plane at z 2.5

(b) *Magnetic field*

Figure 5-4: *TEM* mode propagation developed in *MWS*

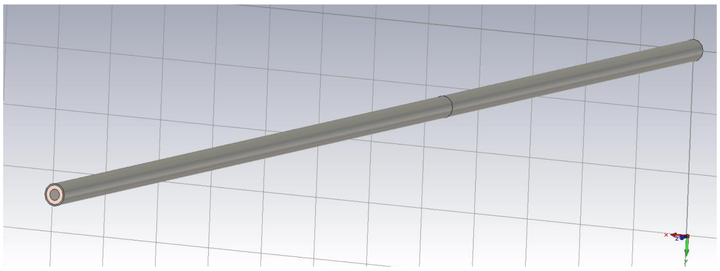

Figure 5-5: Cable model when a single discontinuity is studied: the healthy and faulty lines are *1.5m* and *1m* respectively

studying the shape of the reflected wave, no matter the value of frequency or line length. Due to the smaller line lengths considered, an higher *1GHz* bandwidth is chosen. Since the phase constant β is known from CST (=15.11 $\frac{rad}{m}$), the velocity can be computed corresponding to $4.1 \cdot 10^8 \frac{m}{s}$. It is approximated to a constant value, as done also before, since for wide frequency ranges the inductance can be considered constant and thus the velocity does not depend on frequency, but the high frequency value can be considered. Thus, the wavelength can be computed and its value is around *0.41m* for the maximum frequency.

As first, the effect of the imaginary reflection seen by the fault Γ_0 is studied. The model introduced in this section puts into evidence a difference with respect to the lossless case caused by the imaginary Γ_0 term. In order to analyze the influence of j on the time echo reflected signal just a single discontinuity is considered with a single portion of healthy line of *1.5m* length and *1m* fault, figure 5-5. Two waveguide ports are inserted at the line terminations: a source, representing the transmission port at the healthy line extremity and a matched load, representing the receiving port at the faulty line extremity. The simulations with *CST* software have been carried out and the result shown in figure 5.6(a), in blue. The distortion presented in the plot is a systematic error due to the software since *CST* does not consider tanδ constant in the whole frequency range but just in a higher range (figure 5.6(b)). This problem can be fixed by increasing the number of mesh density although the program deteriorates in computational speed; in any case, it does not figure out a precise constant value and consequently a distortion in the signal is included. In our case a compromise is chosen, where the constant value is reached for a quite wide frequency range. In order to validate the model, the same results must be obtained in *Matlab*. With this in mind, the time domain excitation signal *e(t)* (a Gaussian tapering window is chosen in order to avoid the oscillations due to secondary lobes) is multiplied by Γ_0. In particular, after having applied the Fourier transform to the excitation signal *e(t)* and multiplied it by Γ_0 in frequency-domain, the time reflected signal e_0*(t)* delayed by $2\beta l$ is recovered through a Fourier anti-transform:

$$e_0(t) = \int d\omega E(\omega) j \frac{tan\delta}{4} e^{-j2\beta l}, \tag{5.6}$$

where l is the distance between the injecting port and the fault position. The result is represented in figure 5.6(a) by the red curve. The signal follows the same behavior of the one obtained with CST, both in intensity and reflection width, validating thus the numerical model. The effect of the imaginary term j on the time reflected signal is quite similar to a derivative shape although the term ω is missing.

After the numerical model validation, the complete case is studied with both the fault discontinuities in order to study Γ_f. Again, two ports at the line terminations are added

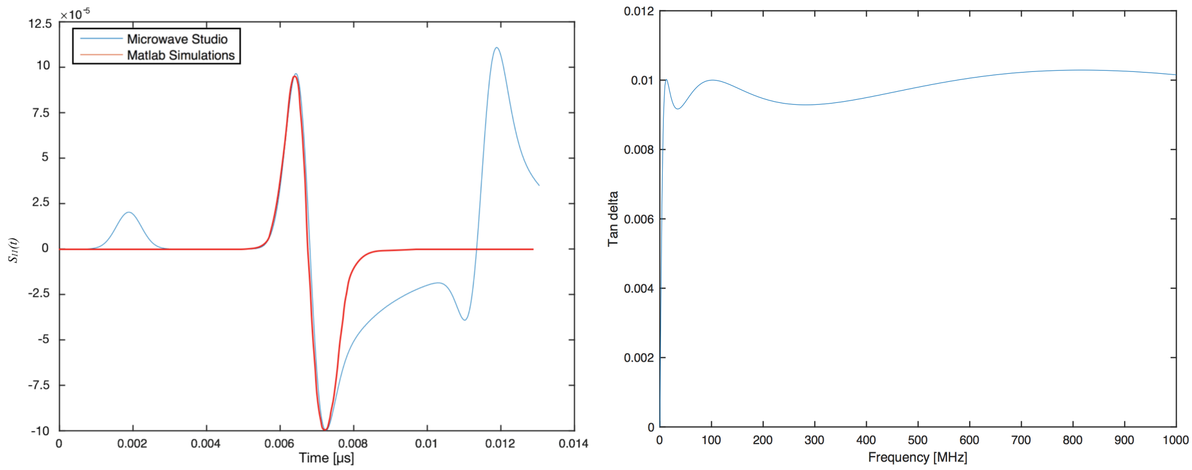

(a) *Comparison between Matlab (red) and CST (blue) results*

(b) *Tanδ behavior in CST*

Figure 5-6: *CST* simulation results when a single discontinuity is studied

operating as transmission and receiving ports. Two cases have been analyzed: when the fault is not electrically short (figure 5.7(a)) with *1m* of faulty line length and when it is (figure 5.7(b)) with *1cm* of faulty line length. In the first case, *1m* of healthy line lengths are considered while in the second case *1.5m*: this choice has been done in order to obtain the same time delay around *7ns* in both the cases and show with more clearness the comparison. The result is shown in figure 5-8, where the blue line represents the case *(a)* and the red line the case *(b)*. At each discontinuity the term Γ_0 is presented, with different signs since at the second discontinuity

$$\Gamma_0 = -j\frac{tan\delta}{4}. \tag{5.7}$$

Decreasing the faulty line length, the distances between these two two-peaks shapes gets closer until the fault becomes electrically short. In such a case, Γ_f can be approximated by the equation 4.8 and a single reflection is shown. This result is very similar to the one of figure 5-2 obtained with Matlab for the same value of tanδ, fixed at *0.01*. The same intensity of the reflection and the same shape is figured out, numerically validating the Γ_0 model introduced, where the negative peak of the signal identifying the fault position is given by the real nature of Γ_f (equation 5.4).

5.2 Z Fault

In presence of losses, limitations in frequency arise and in the time-domain methods bad spatial resolutions are performed. On the contrary, Port MUSIC is able to ensure super resolution performances, showing very precise results. In this case the entire line is lossy

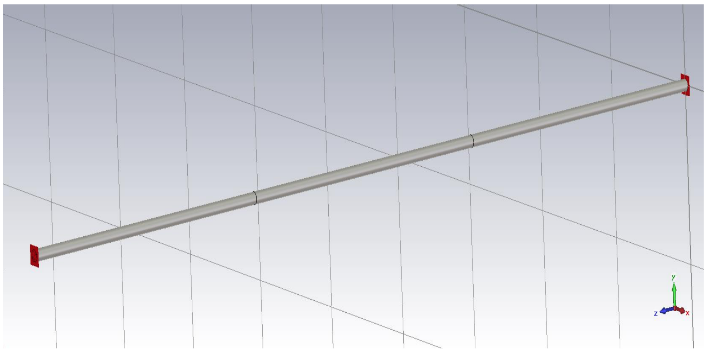

(a) *Not electrically short fault*

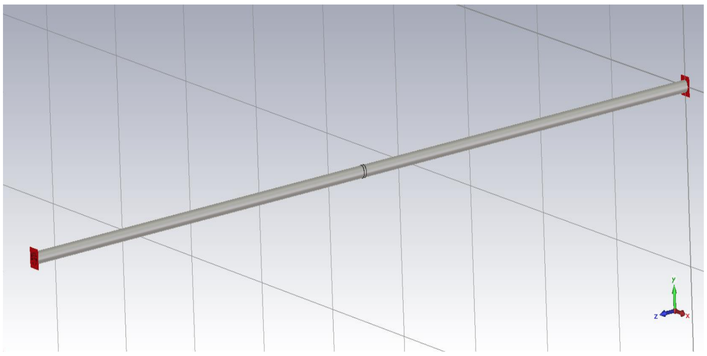

(b) *Electrically short fault*

Figure 5-7: Cable model when two discontinuities are studied

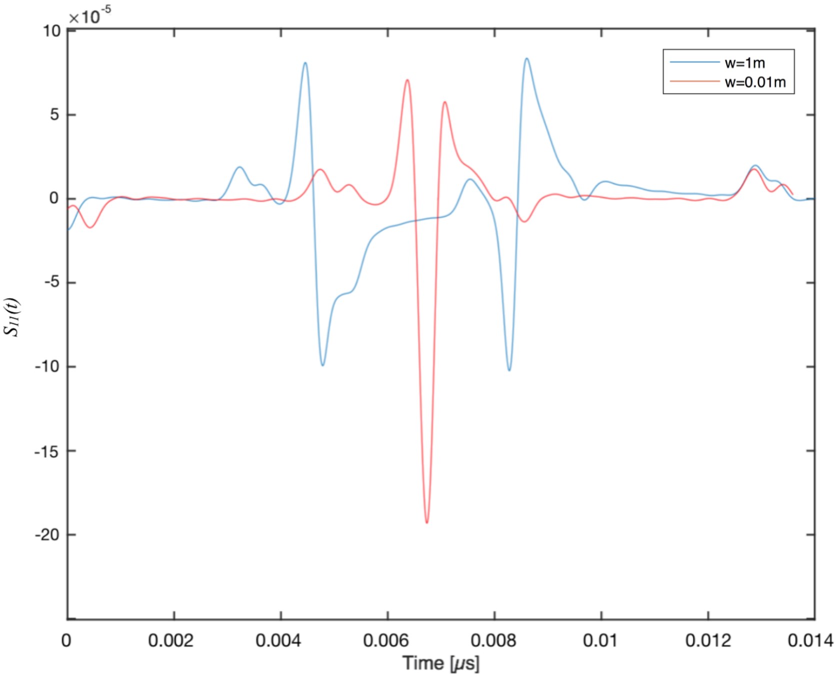

Figure 5-8: CST result when 2 discontinuities are studied: electrically short (red) and not electrically short fault (blue)

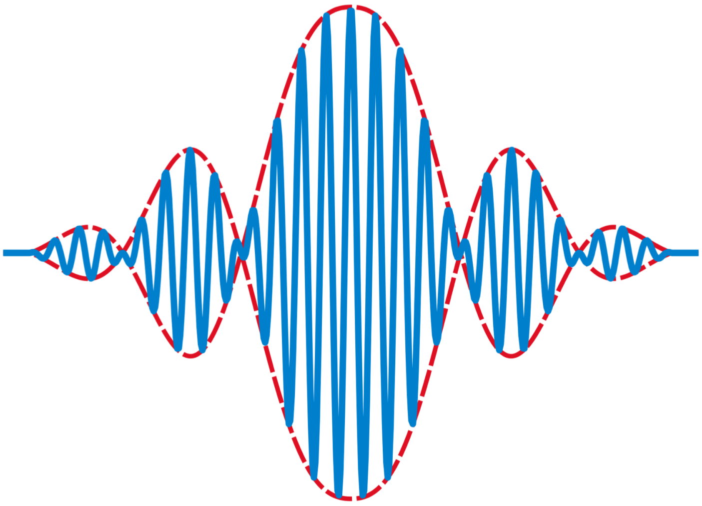

Figure 5-9: Dispersive case: envelope of the wave (in red) and its components (in blue) representing group and phase velocity respectively

with both R $\neq$ G $\neq$ 0 and the characteristic impedance is given by:

$$Z_c = \sqrt{\frac{R + j\omega L}{G + j\omega C}}, \tag{5.8}$$

and for the faulty line portion:

$$Z_f = \sqrt{\frac{R + j\omega 0.9L}{G + j\omega 1.1C}}, \tag{5.9}$$

where G in this case is the same and the fault is simulated as in the lossless case by a 10% decrease and increase of L and C, respectively. Due to the losses, attenuation and dispersion are present in the computations. In fact,

$$\gamma = \sqrt{(R + j\omega L)(G + j\omega C)} = \alpha + j\beta, \tag{5.10}$$

where $\alpha \neq 0$ and $\beta = \beta(f)$. Attenuation is given by the presence of α, as discussed in chapter 2. Dispersion is related to the linear frequency dependence of β. Actually, the substantial difference with respect to the case of section 5.1 is the fact that it is a “*dispersive* ” case. The direct consequence is that velocity is no more constant in frequency but is divided into two terms: *phase velocity* and *group velocity*. The group velocity of a wave is the velocity with which the overall shape of the waves amplitudes, known as the modulation or envelope of the wave (red line in figure 5-9), propagates through the space. For example, if a stone is thrown into the middle of a very still pond, a circular pattern of waves with a quiescent center appears in the water, also known as a “capillary wave ”. The expanding ring of waves is the wave group, within which one can discern individual wavelets of differing wavelengths traveling at different speeds. The shorter waves travel faster than the group as a whole, but their amplitudes diminish as they approach the leading edge. The velocity at which these shorter waves travel is called phase velocity. It is the rate at which the phase of the wave propagates in space and represents the velocity at which the phase of any wave frequency component travels. For such a component (blue lines), any given phase of the wave (i.e., peaks or troughs) will appear to travel at the phase velocity. It is anything else than the ratio between the pulsation ω and the phase constant β, while the group velocity is its partial derivative, since it represents a local velocity:

$$v_{phase} = \frac{\omega}{\beta} \quad , \quad v_{group} = \frac{\partial \omega}{\partial \beta}. \tag{5.11}$$

In particular,

(1) if ω is directly proportional to β, the group velocity is exactly equal to the phase velocity. A wave of any shape will travel undistorted at this velocity. This is the lossless line case;

(2) if ω is a linear function of β, but not directly proportional ($\omega = ak + b$), group and phase velocity are different. The envelope of a wave packet will travel at the group velocity, while the individual peaks and troughs within the envelope will move at the phase velocity;

(3) if ω is not a linear function of β, the envelope of a wave packet will become distorted as it travels. Since a wave packet contains a range of different frequencies (and hence different values of β), the group velocity will be different for different values of β. Therefore, the envelope does not move at a single velocity, but its wavenumber components (β) move at different velocities, distorting the envelope. If the wavepacket has a narrow range of frequencies, and $\omega(\beta)$ is approximately linear over that narrow range, the pulse distortion will be small, in relation to the small non-linearity.

The β formulas derived in chapter 2 (equation 2.13 and 2.16) show that the dispersion acts at lower frequencies, for our studied NUT below $750kHz \div 1MHz$. The β-ω curve will show, thus, linear proportionality for frequency values starting from such a value.

5.2.1 TDR in Presence of Losses

In this dispersive case, two different cases are studied: first, the fault position is at 2.5km from the testing port *(1)*, as done for the lossless case, and then the fault is studied

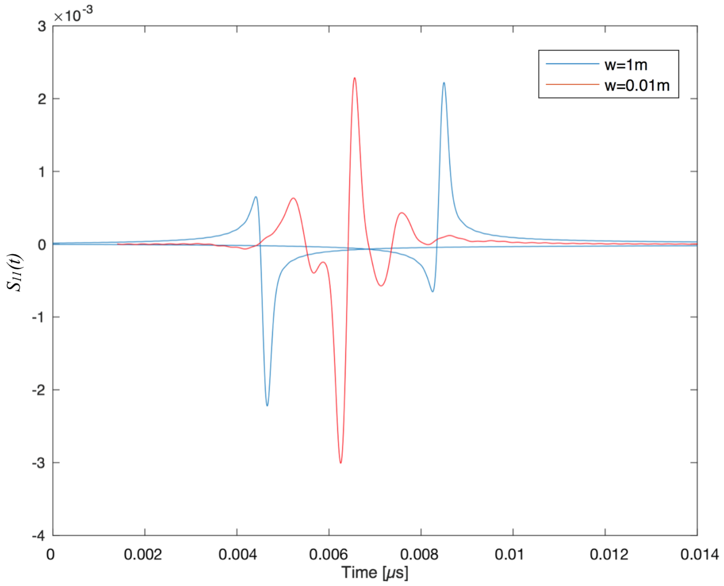

Figure 5-10: Dispersive case: expected e_0(t) shape obtained with *CST*: electrically short fault (red) and not (blue)

at 7.5km from the same port. In fact, in presence of losses both attenuation and f_{max} depend on fault position and, theoretically, more the fault is far from the testing port less the maximum frequency associated to a fixed attenuation value is.

A mathematical model to retrieve the shape of the time reflected wave must be introduced in order to know what should be expected for identifying the fault position. Starting from equations 5.8 and 5.9, the Γ_0 term is given by:

$$\Gamma_0 = \frac{Z_f - Z_c}{Z_f + Z_c} = \Gamma_r + j\Gamma_i = -0.0493 + j0.0087, \tag{5.12}$$

obtained after some operations with *Wolfram Mathematica Software*. Both Γ_r and Γ_i depend on R, L, C, G of the cable and ω. Substituting the equation 5.12 in 4.5, the term Γ_f is given by:

$$\Gamma_f = j\omega 2\frac{w}{v}\Gamma_r e^{-j\beta w} - \omega 2\frac{w}{v}\Gamma_i e^{-j\beta w}, \tag{5.13}$$

and with $f_{max} = 10MHz$ and *w=1*:

$$|\Gamma_f| = 2\omega\frac{w}{v}\sqrt{\Gamma_r^2 + \Gamma_i^2} = 0.033. \tag{5.14}$$

The reflectogram showing the expected shape of Γ_f is plotted with *CST* (figure 5-10) where a line with the fault electrically short (0.01m) and not electrically short (1m) is considered with f_{max}=1GHz (figure 5-7). Both attenuation and dispersion are very low in this case since the fault position is very close to the testing port (l_1=1.5m) and the frequency range considered is wide. This plot is very important since it gives an indication

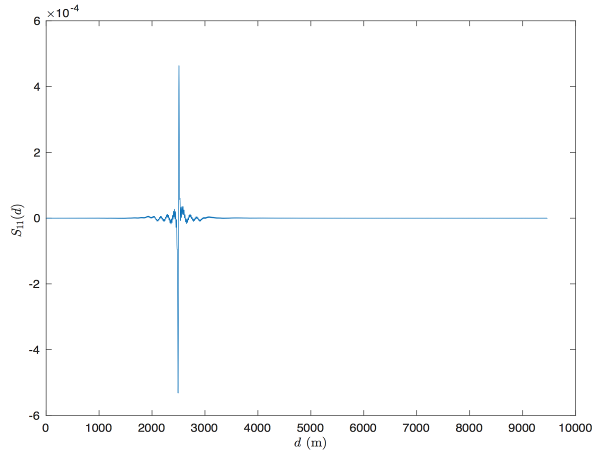

(a) *Fault at 2.5km from the injecting port* (b) *Fault at 7.5km from the injecting port*

Figure 5-11: Reflectograms with f_{max}=10MHz

of what we are expecting on the reflectogram shape in this dispersive case. The analysis throughout *Matlab* can be now carried out, considering the fault at the two different positions.

When the fault is at 2.5km from the testing port attenuation and dispersion are weak. The reflectogram is shown in figure 5.11(a), where it is possible to observe that the fault can be easily located at 10MHz. In fact, according to table 2-6 in chapter 2, the f_{max} associated to *10dB* of attenuation is on the order of 5MHz and thus at 10MHz it is quite weak, around *15dB* according to equation 2.19, making the fault location feasible. The problems arise when the fault distance from the testing port increases. Keeping constant the frequency at 10MHz attenuation increases, making more difficult the fault location. As a matter of fact, the case with the fault at 7.5km from the injecting port is considered and the reflectogram shown in figure 5.11(b). It is evident the stronger attenuation (around 50dB) influence which make the fault location hidden and the expected e_0(t) shape is not visible. In order to reduce the value of attenuation, the value of f_{max} must be reduced: the analysis done in chapter 2 results here very useful. Arbitrarily choosing a fixed value of attenuation at *10dB*, as already explained, the value of related f_{max} can be retrieved according to figure 5-12 and it is around *605kHz*. Thus, a frequency reduction is applied and consequently a clearer time-domain signal is obtained, shown in figure 5-13. The expected peak is now visible and the fault can be identified. However, there is a price to be paid: reducing the frequency bandwidth, a dilatation in time-domain occurs, according to Fourier theory. It implies a worse spatial resolution (around *320m*) in the time impulse injected and a consequent deterioration in the precision estimation, as shown in figure 5-14. Losses deteriorate the accuracy estimation too: the fault is not located at the exact position due to the fact that the fixed high frequency velocity is

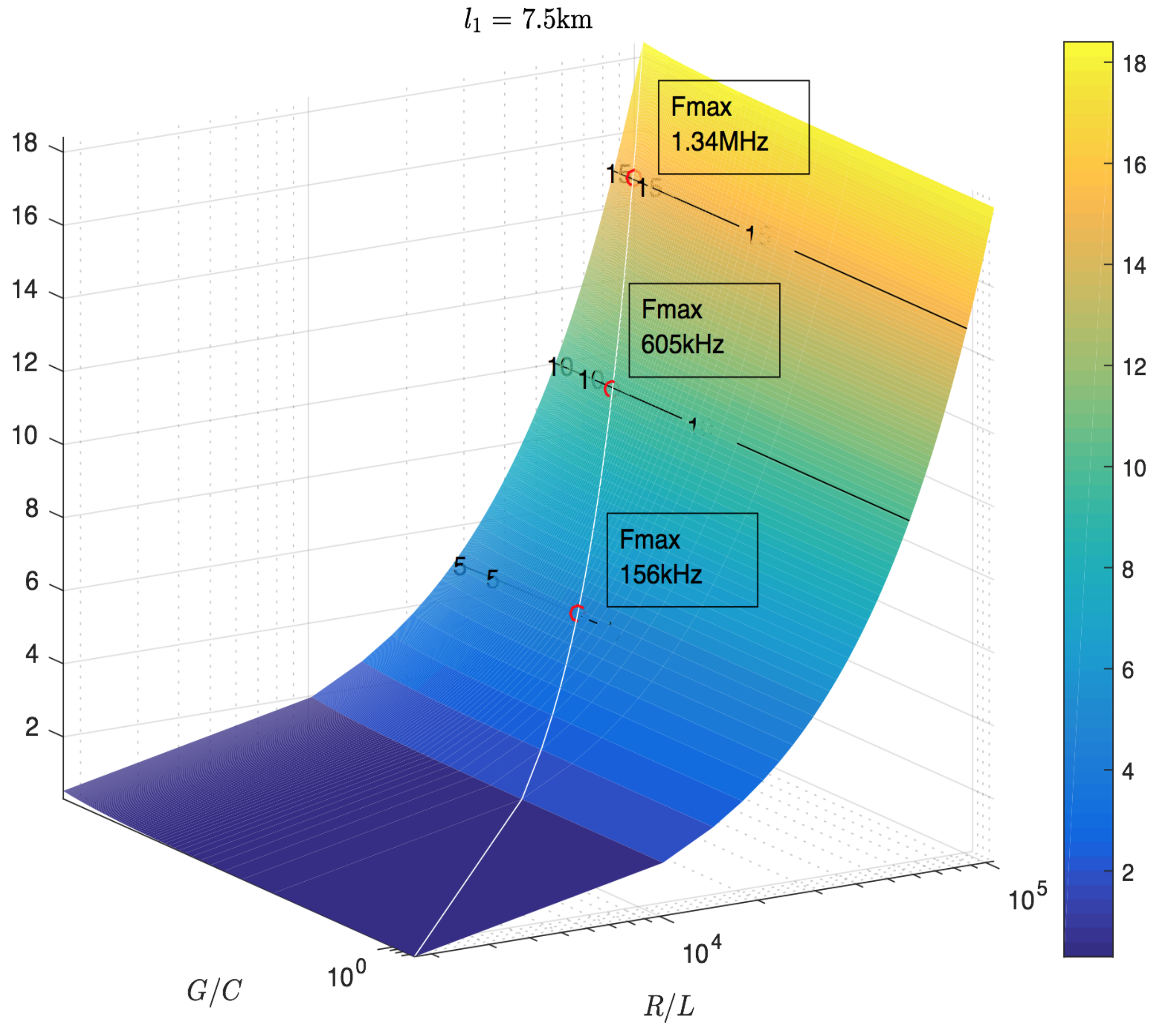

Figure 5-12: Three-dimensional attenuation-losses plot with the fault at 7.5km from the injecting port

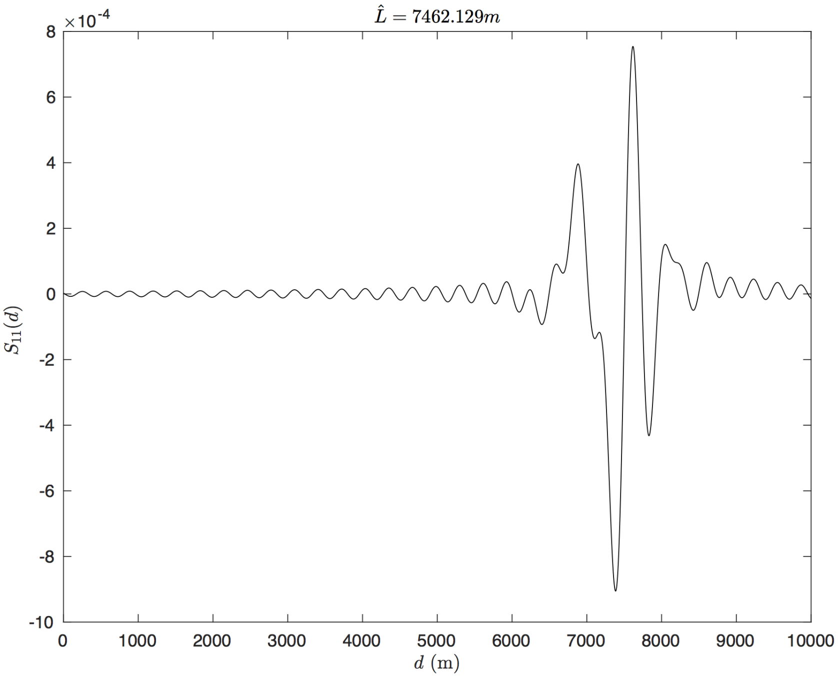

Figure 5-13: Reflectogram with the fault at 7.5km and f_{max}≈605kHz

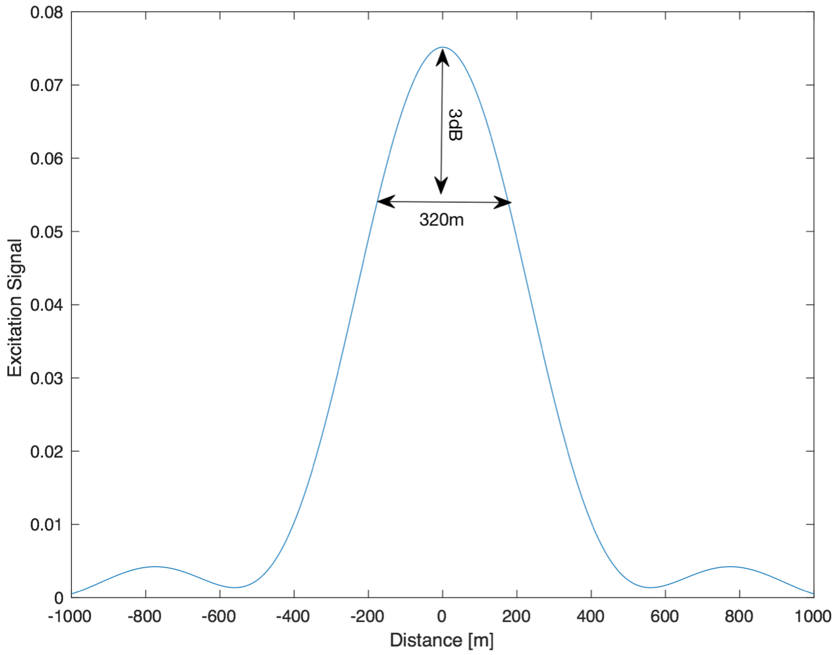

Figure 5-14: TDR spatial resolution in presence of losses with the fault at 7.5km from the injecting port and f_{max}≈605kHz

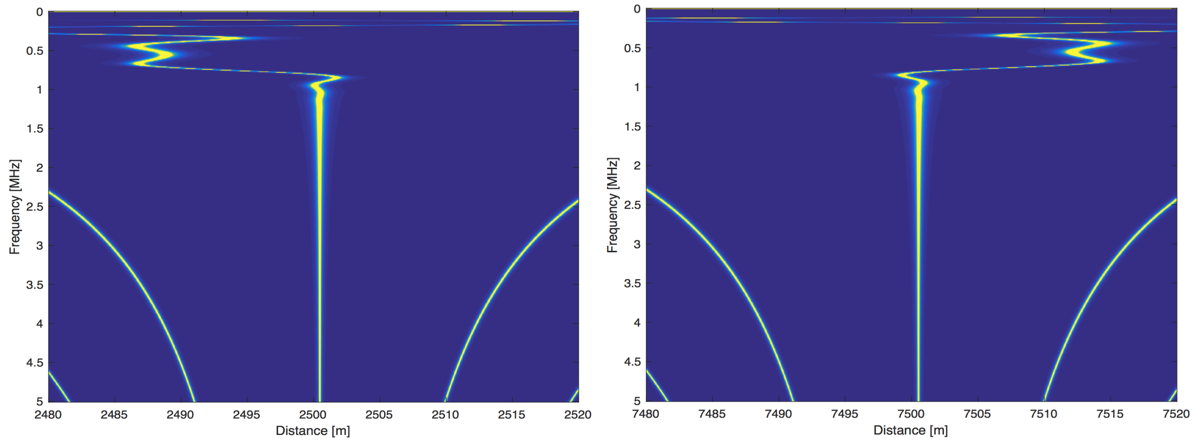

(a) *Fault at 2.5km from the injecting port* (b) *Fault at 7.5km from the injecting port*

Figure 5-15: Pseudo-spectra with f_{max}=10MHz

considered. However, since in this case v=$v(f)$ a systematic error is present.

5.2.2 MUSIC in Presence of Losses

As already said, MUSIC operates only on phase patterns since a normalization procedure is applied. Therefore, only dispersion influences its performances in presence of losses: the problems arisen in TDR due to attenuation can be overpassed and there is no need to reduce the frequency bandwidth. According to what stated in chapter 2, dispersion acts at lower frequencies, up to 750kHz÷1MHz. This is verified from the Pseudo-spectra in figure 5-15, where from that value of frequency the fault can be easily located. Up to that frequency value, β is wrongly detected and consequently the fault position. The reason why is due to the velocity dependence on frequency: the phase velocity is considered and

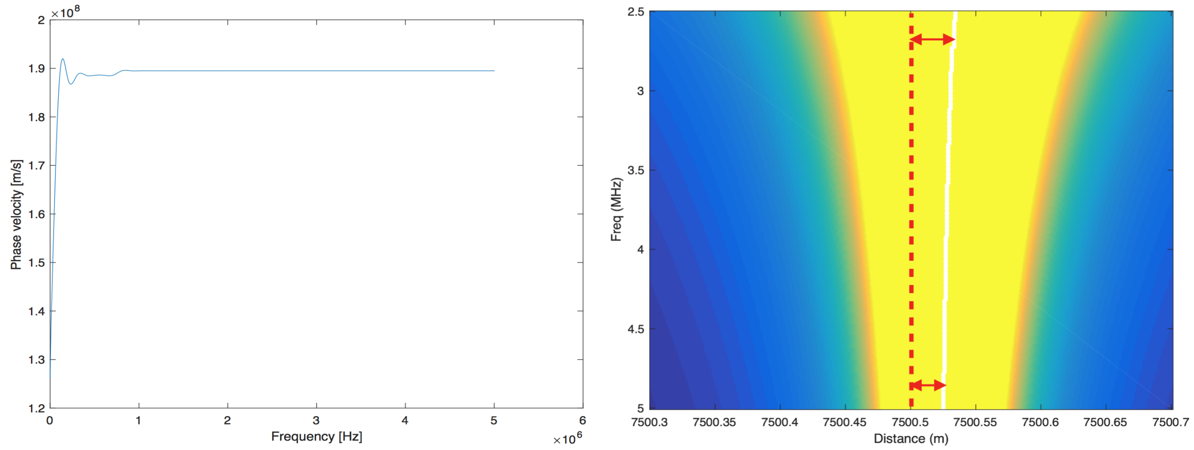

(a) *Phase velocity in function of frequency* (b) *Pseudo-spectrum at higher frequencies*

Figure 5-16: Effects of dispersion in Port MUSIC

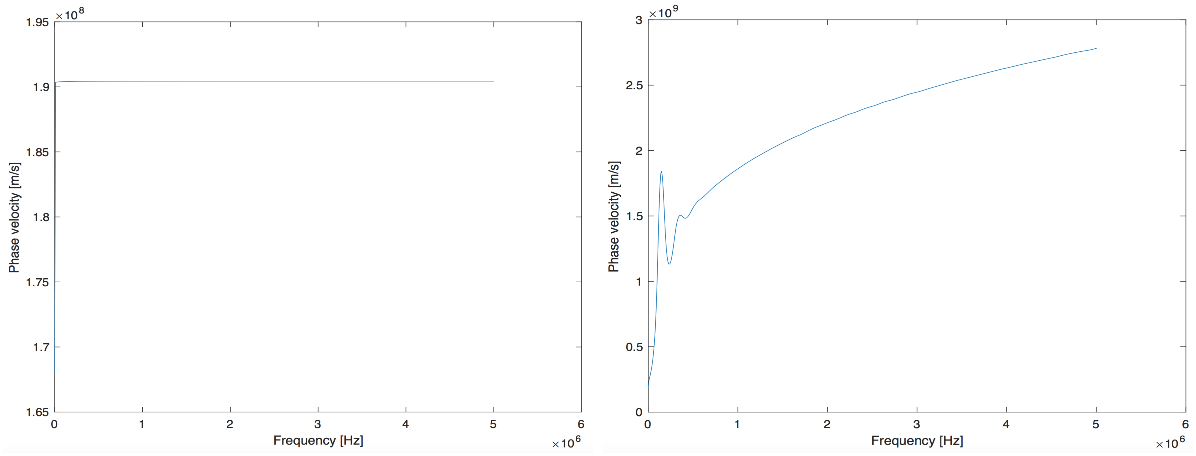

(a) *L constant* (b) *30% of L variation*

Figure 5-17: Phase velocity at different L variations

at lower frequency it is affected on dispersion. For $\omega > \omega_0$ at which the equation 2.16 is verified, v_{phase} tends to v_{group} and β gets closer to the linear proportionality with ω (figure 5.16(a)). However, it will never reach the perfect linearity due to losses and consequently a small spread will be present, as shown in figure 5.16(b).

This dispersion is associated to the R, G and L variation in frequency. In order to see the relative contributions and analyze the causes of such a dispersion, a sensitivity approach is adopted where the weight of the inductance variation has revealed stronger than resistance and conductance. With this in mind, two examples of different L variation are shown in figure $5-17$, where in (a) is taken constant and in (b) its variation is 30%. It is important to note that a phase Γ_f term has been introduced when dispersion is present. Consequently, in order to properly apply the projection procedure a phase normalization

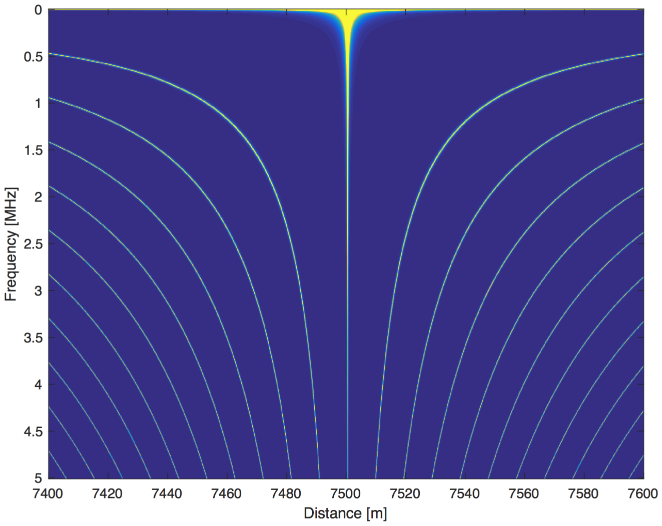

Figure 5-18: Dispersive Pseudo-spectrum after compensation

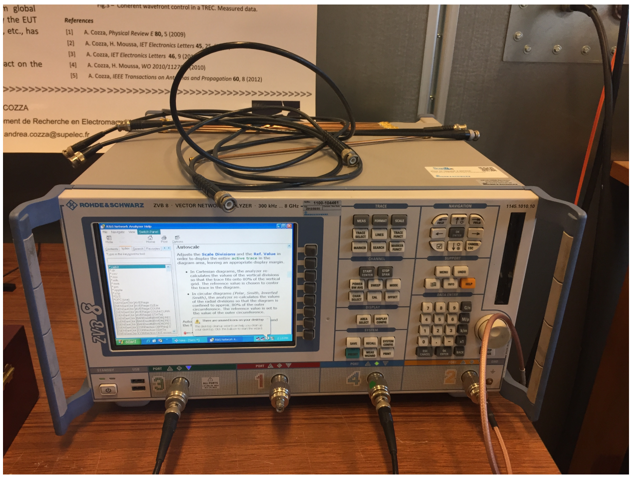

Figure 5-19: VNA adopted in the experiments situated in GeePs department of Supélec, Gif-sur-Yvette, France

Figure 5-20: GPIB interface device realized by Agilent Technologies

must be applied too. Besides, operating frequency by frequency, $\beta(\omega)$ can be retrieved and, known the distance from the port, it is possible to compensate the phase distortion and obtain a precise Pseudo-spectrum (figure 5-18). Moreover, the super-resolution still remains on the millimeter order as in the lossless line case.

To conclude, in presence of losses *frequency* and *time* are mixed together in the time-domain methods and thus it is not possible to distinguish at which frequencies the dispersion acts, while in MUSIC it is well-defined. Besides, Port MUSIC is not affected by amplitude distortion since a normalization is applied and no frequency limitations occur.

5.3 Experimental Results

In order to verify the feasibility in practical applications of MUSIC, measurements with VNA are performed. This kind of measurements are conducted on shorter high frequency cables and not on the 10km power cable studied in this work. Therefore, these measurements aim to show the practical feasibility and efficiency of Port MUSIC method and not as experimental validation of the obtained results. Particularly, the 10km power cable has not been tested for two main reasons:

(1) unavailability of testing networks (10km power cable, connectors, measurement set) at the Centrale-Supélec laboratory;

(2) difficulty on simulating *1m* faults, above all tanδ ones, really caused by defects as moisture or water trees.

Real scattering parameters are computed by means of VNA and the post-processing operation is done with Matlab. The experimental measurements shown in this section are conducted testing the single branch configuration without presence of losses, since losses in the tested high frequency cables are very low and can be neglected without errors. The real scattering matrices are measured through a Vector Network Analyzer (VNA) whose testing ports were connected to the extremities of the NUTs. The VNA we used is a Rohde&Schwarz ZVB-8 network analyzer, with a frequency range from 300 kHz to 8 GHz, and four testing ports, shown in figure 5-19. The *TOSM* calibration (also referred as *SOLT* calibration) procedure is applied using the calibration kit of the Rohde&Schwarz ZVB-8 network analyzer, by testing the open, short and matched termination at each port and the through termination between the combinations of the ports. Although we are interested on reflection measurements only, we chose to apply this kind of calibration, where also the transmission parameters are measured, since it ensures a better general accuracy with respect to the reflection normalization procedure, in which only the S_{11} and S_{22} parameters are measured. The intermediate-frequency filter bandwidth was set to 100 kHz. The input power has been set at 0dBm harmonic excitation signal: this ensures a strong rejection of noise, yielding very clean results that can be regarded as practically unaffected by any noise source. Using the VNA implies accessing the collected data in frequency-domain. Thus post-processing using Matlab has been applied in order to extract the time-domain responses using the Fourier anti-transform. The importation of the data collected through VNA in Matlab has been done by means of a GPIB interface device realized by Agilent Technologies (figure 5-20), which connects together the VNA and the PC with Matlab included. By means of some Matlab functions the scattering data are imported and saved in the code. Every device is characterized by an address

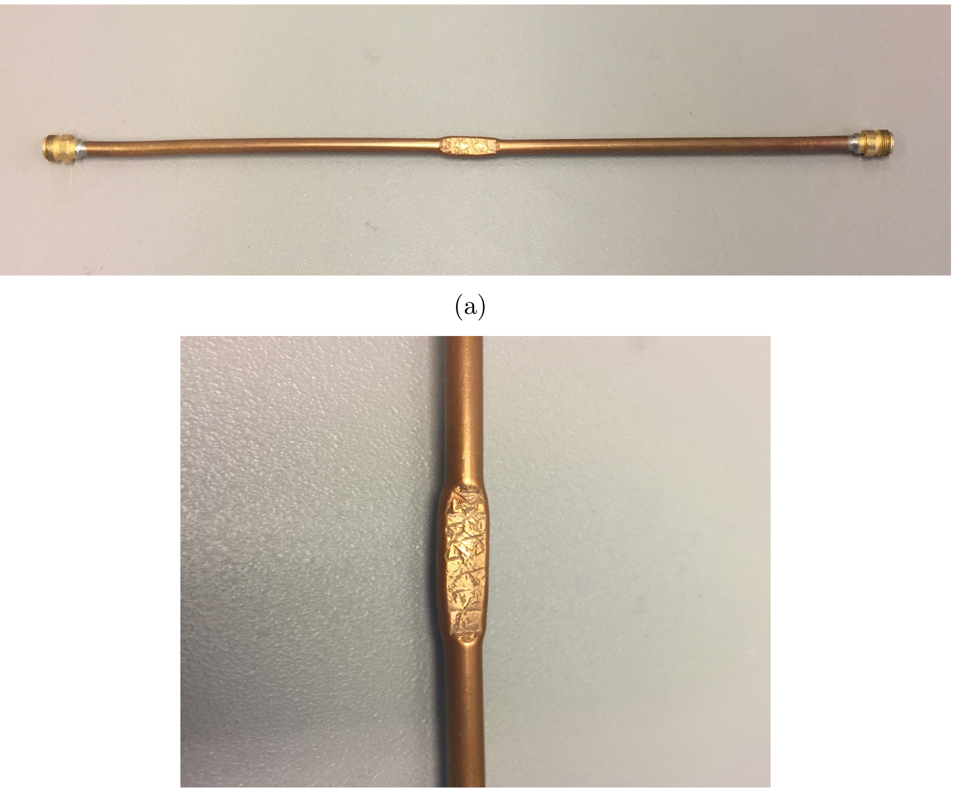
(a)

(b)

Figure 5-21: 20cm long sample made of semi-rigid coaxial lines

number, which allows to Matlab to recognize it and create a connection between the devices. Besides, parameters needed for the post-processing computation have been set and then the same approach used for simulations has been carried out. Coaxial cables with 50Ω of characteristic impedance have been used as transmission lines. It is difficult to find practical coaxial cables with this characteristic impedance, but nevertheless for measurements they ensure high stability in the procedure. The conclusions drawn in this section are not related to the type of lines used, since the proposed method is completely general, and thus also for longer lines it can be applied. Shorter coaxial cables offer another important advantage, since soft faults can be introduced through a set of 20cm long samples made of semi-rigid coaxial lines terminated by two connectors. Crushing the sample, a soft fault is simulated as shown in figure 5-21. In our case, we have considered a 1.4mm crush sample with 1cm of length; intuitively, less a crush is, more the fault is soft. As a consequence, the thickness from its normal 3.4mm cross-section has been reduced to only 2mm. The cables have been strictly bonded to the table by means of some stickers in order to prevent undesired effects eventually caused by sudden movements. Moreover, in order to try to minimize the effect of the interconnections between the cable and the VNA, the *difference system* will be considered. Thus, two

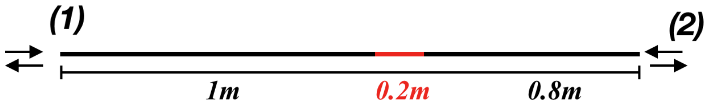

Figure 5-22: NUT considered in the experiments

scattering matrices of the NUT have been measured, the faulty one and the healthy one, always by placing the semi-rigid line in the network. As a matter of fact, in post-processing done in Matlab the difference between these two scattering matrices is taken into account and the only reflection coefficients of the resulting matrix is involved in the $\underline{v_1}$ construction. This procedure is called "*baselining*" (or *difference system*) and it will be better seen in the next chapter when the Y-branched network is studied and the need of the junction removal becomes necessary for the efficiency of the fault location methods. The considered cable is 2m length and the first termination of the 20cm semi-rigid cable is situated at 1m from the testing port (1), as shown in the figure 5-22, and the practical NUT implementation is shown in figure 5-23. The measurement of the scattering matrices has been done considering a bandwidth going from 1MHz to 1GHz; by means of VNA, magnitude, phase and the correspondent Smith Chart are obtained and their values used in the post-processing operation done with Matlab. Obviously, in order to verify the feasibility of the method, the fault is simulated also in Matlab by means of the generated codes introduced in the previous sections and the resulting Pseudo-spectra are compared (figure 5-24).

In this work, a simple experiment validation has been done by recalling the work contained in [3], where more complex structures have been studied and experimentally validated, in order to take confidence with the VNA real measurements and showing the feasibility of the method, although the impossibility of testing 10km power cables. Another interesting thing to observe is that considering higher frequencies, the super-resolution performance of MUSIC is going to improve. In fact, increasing the frequency

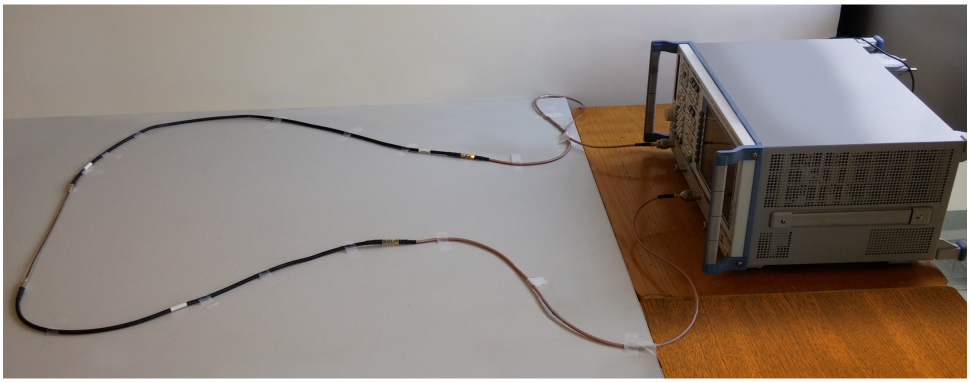

Figure 5-23: Practical NUT implementation

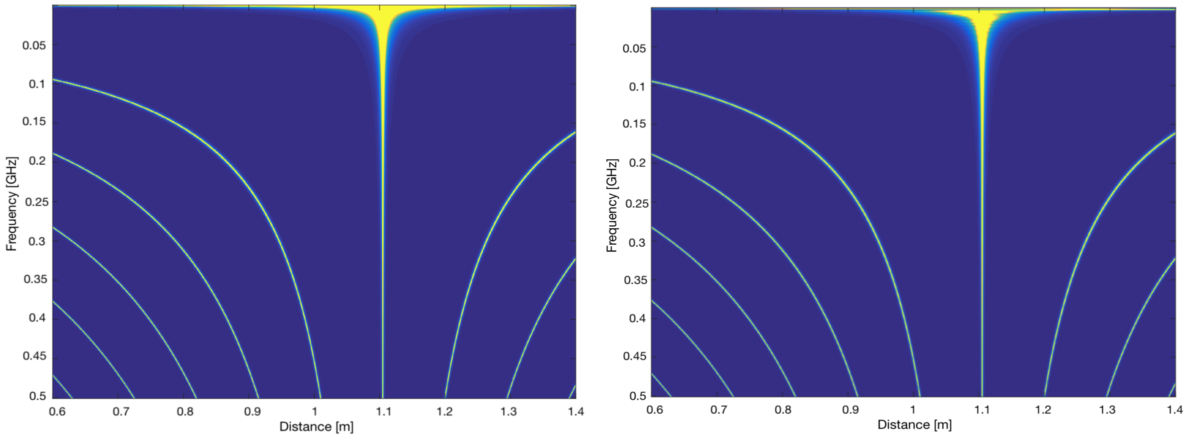

(a) *Model simulations* (b) *VNA measurements*

Figure 5-24: Pseudo-spectra comparison referred to the NUT of figure 5-22

the wave support is smaller and together with it also the spatial resolution, with a value moving around 0.01mm. As a matter of fact, the distance between the different ghosts corresponds, also in this case, to $\frac{\lambda}{4}$ and it is possible to observe that at 500MHz is around *10cm*.

5.4 Summary

In this chapter losses are introduced in the line and TDR and Port MUSIC are compared in performances. Time-domain methods are influenced by both amplitude and phase distortion due to attenuation and dispersion, respectively. In particular, the study carried out in chapter 2 about the mapping has resulted useful since the f_{max} related to a particular attenuation value is derived. Thus, in order to obtain good attenuation values a frequency limitation in bandwidth occurs causing a deterioration in spatial resolution.

Port MUSIC is very advantageous in this lossy case: in fact, operating frequency by frequency, dispersion can be confined at low frequency ranges and above a certain frequency value the fault can be easily located. Moreover, attenuation does not affect its performances, not causing frequency limitations and super-resolution is still verified.

At last, MUSIC experimental validation with VNA are performed proving the practical feasibility of the method.

Chapter 6

Soft Fault Location in a Y-Branched Line

IT is interesting now to study a more complex case when an higher number of testing ports is present. A Y-branched structure is analyzed where the role of the junction shall be accurately investigated. Actually, the operational mode of TDR is already known and discussed in chapter 1, where signals must be injected from all the ports and a triangulation is necessary to identify the fault position. In the first part it is re-called together with the explanation of the baselining system, in order to study and avoid the effect of the junction.

Then, the behavior and performances of Port MUSIC are presented, both through simulations and experiments, and a comparison with TDR is carried out.

6.1 The Baselining System

Echoes which come back from targets and interfere with useful signals are referred as *clutters*. Such undesired signals can be due to targets including natural objects such as ground, sea, precipitations, sand storms, animals (especially birds), atmospheric turbulence, and other atmospheric effects, etc. In such cases, the echoes returned by a relatively weak reflectivity target may be masked by those produced by clutter leading to an impossibility of detection in some critical cases. Consequently, to overcome the problem of clutter in free space propagation, the basic idea was to try to minimize as much as possible its effect, introducing the concept of "*difference system*" or "*baselining* ". This situation can be also verified in wave propagation along guided structures, where discontinuities (as junctions) play the same role of clutters masking the fault especially in presence of soft one that is basically characterized with weak reflectivities. The basic concepts of baselining are introduced and explained in this section, first in free space and then in wiring networks.

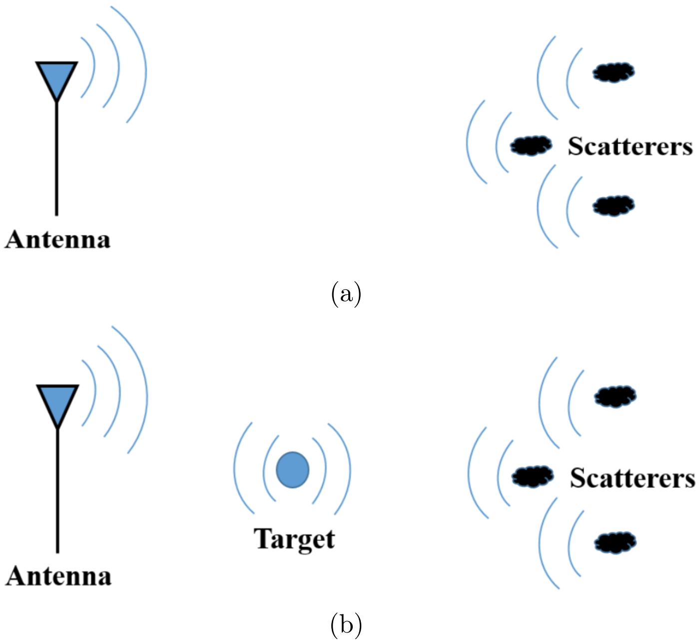

Figure 6-1: Free space propagation without (a) and with (b) targets

6.1.1 Baselining in Free Space

An antenna emitting waves is firstly considered in an homogeneous medium and the presence of many scatterers analyzed, as shown in figure 6-1. At the beginning (a), no target is present in the medium, thus the wave propagates until it interacts with the scatterers. In presence of several scatterers a multiple scattering scenario is obtained, where a specified scatterer X not only reflects the initial emitted wave but also several reflections coming from other scatterers occur. However, if the scatterers are distant from each other, the reflected wave interaction is considered (referred to the single scattering scenario) and the waves reflected from the other scatterers are negligible. In fact, the wave reflected from a scatterer X and interacting with other scatterers is minimized since its amplitude decreases as the square the distance separating X from other scatterers. In (b), a target is added. Multiple reflections occur given by the interactions between scatterers and target. Under the assumption of the single scattering scenario, only the most significant reflected wave resulting from the first interaction will be considered for both the case of the target and the scatterers and subtracting the total waves (incident and reflected) present in (b) from those in (a), only the reflected wave diffracted by the target results. This is verified if the *first-order Born approximation* is applied, i.e. the reflected waves of the other scatterers are not affected by its presence. A "new " system is obtained by applying the difference of the systems with and without the target presence: it seems as the target was a secondary source, emitting isotropically in all directions. This system is denoted as *baselining*; equivalently, it corresponds to a system

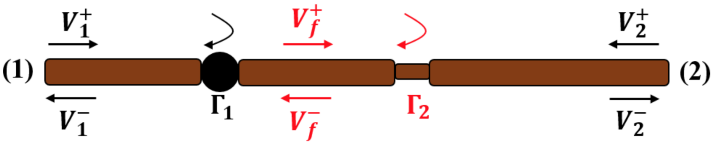

Figure 6-2: A transmission line containing an impedance discontinuity with a reflection coefficient Γ_1 and a fault with a reflection coefficient Γ_2

whose transfer function is the result of the subtraction of two transfer functions: the first one is the reference system without the target and the second one is the system with the presence of the eventual target. In the same way, a fault in a wiring network can be considered as a scatterer in free space, where a fault can be seen as a target while discontinuities (including junctions and mismatched loads) as scatterers. In this case, multiple scattering scenario refers to the multiple reflections involving fault and junction. However, some inequalities are present for the difference system between free space and guided wave propagation. Waves are attenuated as the inverse of the distance in free space, while guided waves perform negligible attenuation. Under the assumption of a soft fault, the effect of the other elements of the system after the subtraction operation are ideally removed and the fault can be treated as a secondary source, as seen for the target in the open media case.

It is important to note that the baselining system results fundamental for fault detection and location techniques above all in presence of soft faults. The reason is intuitive since it makes the signature of the initially weak reflectivity soft fault more visible in presence of junctions.

6.1.2 Baselining in Wiring Networks

Although most of the contributions of other elements in the system not related to the fault are avoided, due to the multiple interactions with the target a residual contribution of such elements still exists and appears in the difference system response. To better understand such a contribution, a simple uniform lossless transmission line is considered, containing a discontinuity of reflection coefficient Γ_1 and a fault of reflection coefficient Γ_2 as illustrated in figure 6-2. For the sake of simplicity line lengths are equal to zero, and consequently no delay terms will appear in the following computations. The incident and reflected voltages at the extremities (1) and (2) are given by V_1^+, V_1^-, V_2^+, and V_2^- respectively. The system is assumed being in a steady state and that the waves propagating in the faulty system between the discontinuity and the fault referred to as V_f^+ and V_f^-. Under these assumptions,

$$V_f^+ = V_1^+(1+\Gamma_1) + V_f^+\Gamma_1\Gamma_2, \tag{6.1}$$

dividing and factorizing,

$$\frac{V_f^+}{V_1^+} = \frac{1+\Gamma_1}{1-\Gamma_1\Gamma_2}. \tag{6.2}$$

The global reflection coefficient at the first port (1), denoted as

$$S_{11} = \left.\frac{V_1^-}{V_1^+}\right|_{V_2^+=0}, \tag{6.3}$$

shall be calculated firstly in the reference system without the fault, where

$$S_{11}^b = \Gamma_1, \tag{6.4}$$

whereas in the faulty network it is given by

$$S_{11}^f = \Gamma_1 + \frac{\Gamma_2(1+\Gamma_1)^2}{1-\Gamma_1\Gamma_2}. \tag{6.5}$$

Knowing that in this case,

$$V_1^- = \Gamma_1 V_1^+ + \Gamma_2(1+\Gamma_1)V_f^+ \tag{6.6}$$

the global reflection coefficient of the *"baselining"* can be calculated as

$$S_{11} = S_{11}^f - S_{11}^b = \frac{\Gamma_2(1+\Gamma_1)^2}{1-\Gamma_1\Gamma_2}. \tag{6.7}$$

It is clear that the baselining does not eliminate totally the contribution of the discontinuity, designated by Γ_1 in the equation 6.7, thus explaining the presence of multiple reflections. With this in mind, the harder the fault is, i.e the higher Γ_2 is, the more significant is the perturbation brought by the fault presence to the system. Consequently, soft faults ensure weaker perturbations caused by the fault's presence in the system.

6.1.3 Performance Analysis of Baselining in Case of Soft Fault

In order to better illustrate the concept of baselining for the case of a soft fault, the single junction network of figure 6-3 is considered. The reflectograms of figure 6-4 show the TDR echo for the system containing the fault and that deprived of it, where a stronger echo can be seen at the position of the junction whereas a barely visible response can be detected at the position of the soft fault (figure 6.4(a)). Applying the difference system to the responses of the two systems the effect of the junction is removed and a stronger visible signature identifies now the fault position, as shown in figure 6.4(b). Accordingly,

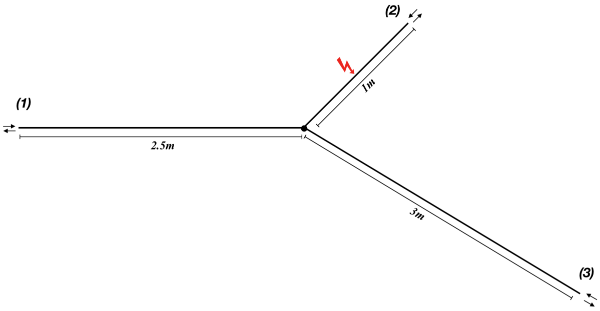

Figure 6-3: A transmission line containing an impedance discontinuity with a reflection coefficient Γ_1 and a fault with a reflection coefficient Γ_2

the main objective of baselining in making the soft fault' s weak signature visible is demonstrated and validated in this example. On the other hand, it is important to point out that the results are obtained on the basis of a perfect baselining, i.e. 100% identical network to that of the faulty topology one. What if a perfect baseline is not available? This is a reasonable question since all methods using the difference system to improve the detectability of soft faults are either accomplished with simulations or with measurements done in a very controlled laboratory environment. Baseline approach is a very good solution to make soft faults more visible, but it is very difficult to obtain such a perfect one in a realistic environment. For instance, such wire movements which are inevitable in high-vibration environments as that in planes or easily in some laboratory experiments, can change the impedance of the wire-NUT interfaces thus masking the eventual presence of a soft fault. It was proven in some experiments that slightly moving a wire create more impedance changes than frays (soft faults). In other words, regardless of how accurate and sensitive the systems are made, the environmental impedance changes can be expected to be larger than the fray impedance change, making it impossible to locate such frays using reflectometry methods. Under those circumstances, and due to the deficiency of reflectometry methods in dealing with soft faults when discontinuities are present, adopting time reversal for this purpose becomes essential. They can ensure a maximization of the energy impinging on the fault position with respect to the rest of the system (DORT) or a super-resolution performance due to the Green function analysis (TR-MUSIC). In any case, the signals applied to the network no longer aim at directly locating the fault but, rather, are meant to characterize the propagation of signals through the network. The scattering matrix of the network rather than echoes is involved now in the procedure and it should improve the problem of discontinuities arisen with TDR, making the fault, as softer is, always visible.

The numerical and experimental results are shown in the next sections and the performances of Port MUSIC evaluated.

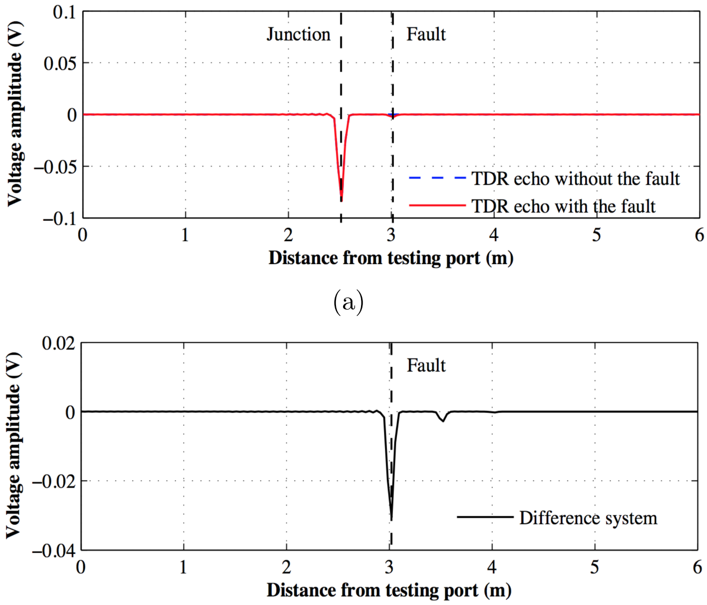

(a)

(b)

Figure 6-4: Free space propagation without (a) and with (b) targets

6.2 Port MUSIC in the Three-dimensional Case

As known, a projection procedure is applied in the operational mode of Port MUSIC and, with respect to the single line case, two main differences arise:

(1) size of $\underline{v}_1$ and $\underline{g}(x)^\perp$ which become $[3 \times 1]$ since three testing ports are present;

(2) space dimension where the projection is involved;

(3) two Green function vectors are involved in the projection.

In fact, given n the number of testing ports of the NUT, the size of the vectors involved is $[n \times 1]$. Besides, the procedure occurs in a n-dimensional space with *(n-1)* $\underline{g}(x)^\perp$. It is interesting to observe that in standard MUSIC *(n-1)* eigenvectors belonging to $\mathcal{N}$ would be involved. Thus, referring to figure 6-5 in the three-dimensional case, a peak is found when both the two Green function vectors $\underline{g}_1(x)^\perp$ and $\underline{g}_2(x)^\perp$ are minimally projected onto $\underline{v}_1$. In other words, $\Phi(x)$ is maximum when both $\underline{g}_1(x)^\perp$ and $\underline{g}_2(x)^\perp$ belong to the same subspace, orthogonal to the subspace where $\underline{v}_1$ is contained. As a matter of fact, the vector $\underline{v}_1$ is given by:

$$\underline{v}_1 = \begin{bmatrix} \frac{S_{11}}{|S_{11}|} \\ \frac{S_{22}}{|S_{22}|} \\ \frac{S_{33}}{|S_{33}|} \end{bmatrix} = \begin{bmatrix} e^{-j2\omega\tilde{\tau}_1} \\ e^{-j2\omega\tilde{\tau}_2} \\ e^{-j2\omega\tilde{\tau}_3} \end{bmatrix}, \tag{6.8}$$

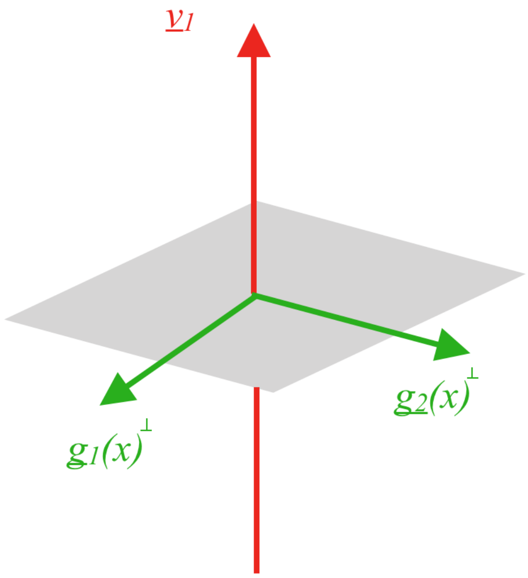

Figure 6-5: Three-dimensional projection procedure

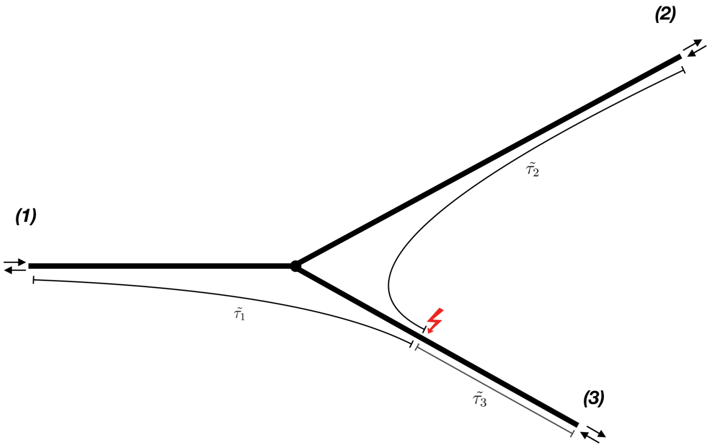

Figure 6-6: Example of faulty Y-branched structure

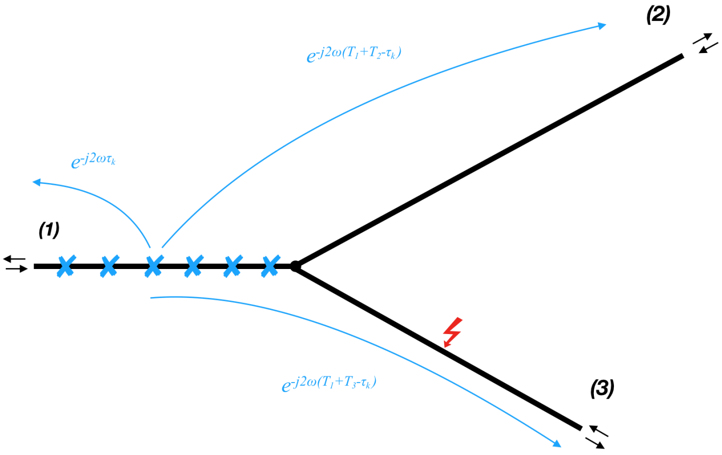

Figure 6-7: Green function evaluation in a Y-branched structure

where $\tilde{\tau_1}$, $\tilde{\tau_2}$ and $\tilde{\tau_3}$ are the times needed to the injected signals for reaching the fault position from the correspondent testing port, as shown in the example of figure 6-6. Differently from the 2-dimensional case, now the Green function must be computed separately branch by branch. With this in mind, firstly the faulty branch is individuated and then the exact fault position along such a branch. For example, the branch 1 is considered and all the positions belonging to this branch are evaluated. The correspondent Green function vector is given by:

$$\underline{g}^{branch\ 1}(x) = \begin{bmatrix} e^{-j2\omega\tau_k} \\ e^{-j2\omega(T_1+T_2-\tau_k)} \\ e^{-j2\omega(T_1+T_3-\tau_k)} \end{bmatrix}, \tag{6.9}$$

where T_1, T_2 and T_3 are the times needed to the injected signals for reaching the junction from the correspondent testing port, as shown in figure 6-7. The same procedure is done for branch 2 and 3:

$$\underline{g}^{branch\ 2}(x) = \begin{bmatrix} e^{-j2\omega(T_2+T_1-\tau_k)} \\ e^{-j2\omega\tau_k} \\ e^{-j2\omega(T_2+T_3-\tau_k)} \end{bmatrix}, \tag{6.10}$$

$$\underline{g}^{branch\ 3}(x) = \begin{bmatrix} e^{-j2\omega(T_3+T_1-\tau_k)} \\ e^{-j2\omega(T_3+T_2-\tau_k)} \\ e^{-j2\omega\tau_k} \end{bmatrix}. \tag{6.11}$$

The two orthogonal vectors $\underline{g}_1(x)^{\perp}$ and $\underline{g}_2(x)^{\perp}$ are obtained multiplying the Green function vectors by $\underline{w}_1$ and $\underline{w}_2$, respectively, where:

$$\underline{w}_1 = \frac{1}{\sqrt{2}}\begin{bmatrix} 1 \\ 0 \\ -1 \end{bmatrix} \quad , \quad \underline{w}_2 = \frac{1}{\sqrt{6}}\begin{bmatrix} 1 \\ -2 \\ 1 \end{bmatrix}. \tag{6.12}$$

The branch 3 is individuated as the faulty one and then the same procedure as before is applied, evaluating $\tau_k = \tilde{\tau}$ for identifying the fault position.

6.3 Numerical Results and Analysis

In this section numerical results on a Y-branched line are performed and the performances of Port MUSIC evaluated. Given a simple structure, as represented in figure 6-8, TDR operates with a simple triangulation, supplying all the testing ports and comparing the three time delays. In fact, in presence of a junction, TDR cannot operate injecting signals in only one branch as before: if the fault is situated on the faulty branch it is able to

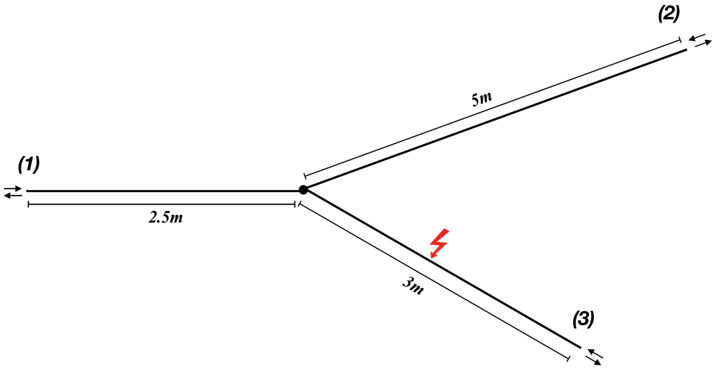

Figure 6-8: Y-branched structure with fault in branch 3

localize its position but if not it fails.

What about Port MUSIC? Obviously, by definition it also operates considering all the branches since the S parameters and the Green function vectors are built according to the number of testing ports. Besides, it operates at single frequencies and the length of each branch must be known a priori; as already said, it represents a disadvantage since without this condition it fails. In this section the performances of Port MUSIC in presence of a junction are analyzed, included the effects of the impedance discontinuity and the method precision estimation. As introduced in section 6.1, the baselining procedure is applied in order to avoid the discontinuity response which could jeopardize the whole performance of the method. Therefore the S_{11} parameter of equation 6.7 is now considered, resulting from the difference between the faulty S_{11} (S_{11}^f) and the healthy S_{11} (S_{11}^b). Noiseless and lossless line is considered in this section: in fact, the effects of noise and losses have been already analyzed in the previous chapters, and no modifications on it are brought by the presence of the junction. Considering the fault as an impedance discontinuity, the same values as in chapter 4 (Z_c =19.24Ω and Z_f =17.4Ω) are considered, thus resulting still a soft fault. Situated in the middle of the branch 3, it is important to point out that the fault line length is 1m and it is situated 1.5km far from the testing port 3 and 1.5km far from the junction. Therefore, the center of the faulty line, which is the point localized by Port MUSIC in the simulations, is 1500.5m. First of all, Port MUSIC individuates the branch in which the fault is situated, as explained in the previous section and then its exact position. When the projection is minimum a peak at each frequency is detected and the resulting Pseudo-spectra for each branch are represented in figure 6-9. As observed, in the branch 1 and 2, the "*healthy branches* ", distanced peaks are found belonging to the ghosts. Instead, an higher peak density is evident in the faulty branch, the number 3, where the hyperbola shapes of the ghosts are clear and each frequency detects a peak at the exact fault position. It is important to remind that the MTLs in this case are oriented from the correspondent testing port to the junction, chosen this convention for

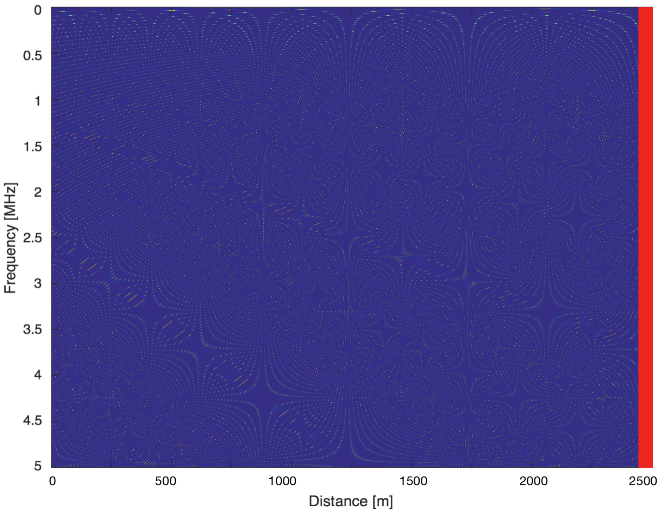

(a) *Branch 1*

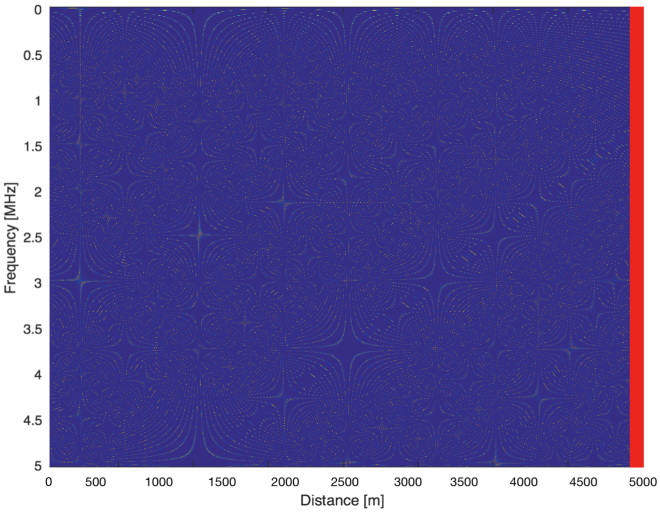

(b) *Branch 2*

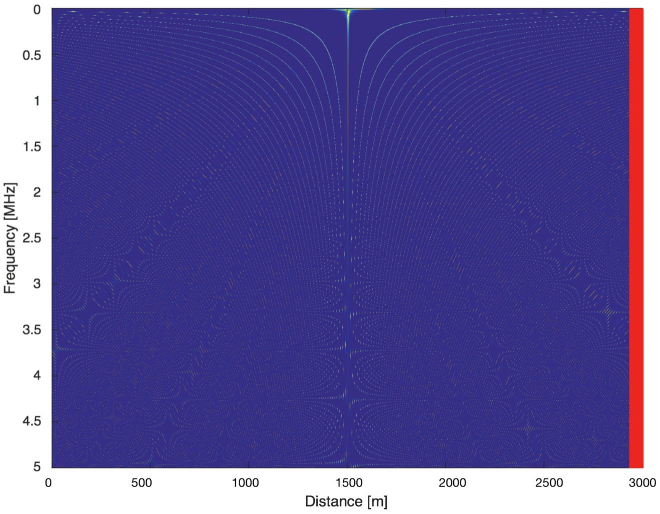

(c) *Branch 3*

Figure 6-9: Pseudo-spectra in presence of a junction, referred to the network of figure 6-8

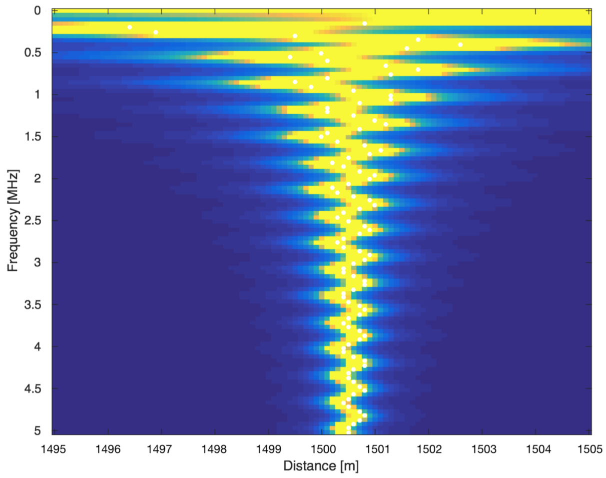

Figure 6-10: Pseudo-spectrum of the faulty branch around the fault position

sake of simplicity. Therefore, in the plots of each branch represented in figure 6-9, the correspondent testing port is on the left while the junction is always situated on the right, marked by the red line. What it is interesting to observe is the shape of the Pseudo-spectrum plot around the fault position. In fact, looking closer in figure 6.9(c) in the 10m range between 1495m and 1505m from the testing port 3, oscillations around the fault position are evident, as shown in figure 6-10. This phenomena is caused by the presence of the junction. As seen in the equation 6.7 (section 6.1.2), although the baselining procedure a little residual term of the junction remains, due to the multiple reflections between fault and junction, as represented in the network of figure 6-11. The blue line represents the reflected wave due to the fault, as in the single line case, and the green line represents the multiple reflection wave between the fault and the junction. Therefore, at the testing port 3 a wave made up by the sum of these two waves back propagates, with two different amplitude and phase patterns:

$$A(\omega) = A_1 e^{-j2\omega\tau_1} + A_2 e^{-j2\omega\tau_2}, \tag{6.13}$$

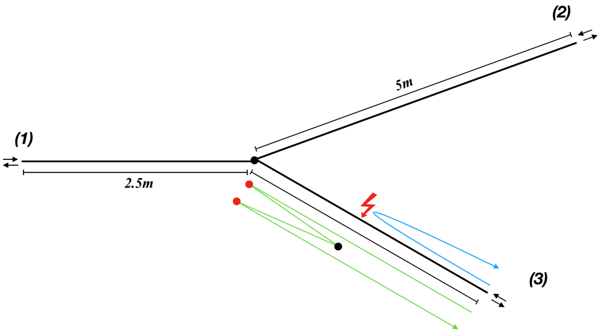

Figure 6-11: Multiple reflections between fault and junction in the Y-branched structure of figure 6-8

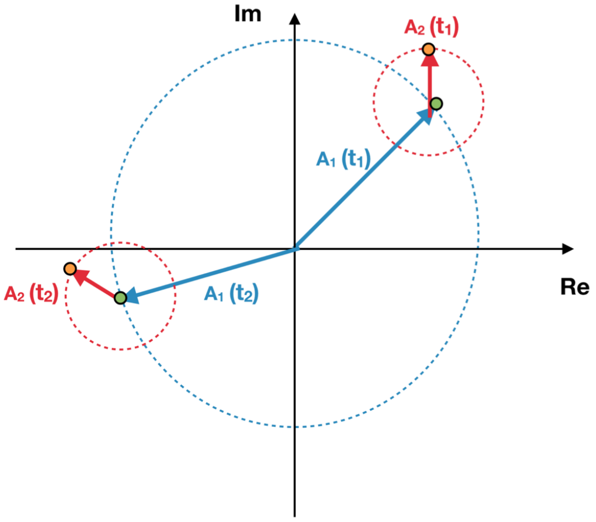

Figure 6-12: $A(\omega)$ representation in the complex plane

where the first term represents the wave reflected by the fault (blue line), and thus,

$$A_1 = \Gamma_f, \tag{6.14}$$

represented by the black point, and τ_1 is the time delay referred to the fault position. Besides, in the last equation the second term represents the residual term due to the junction presence, where its amplitude represents the reflection coefficient and is given by:

$$A_2 = 2\frac{\frac{Z_c}{2} - Z_c}{\frac{Z_c}{2} + Z_c} = -\frac{1}{9}, \tag{6.15}$$

corresponding to the red points of figure 6-11, and where τ_2 is the time delay referred to the multiple reflections between fault and junction. From the last equation,

$$A_2 << A_1. \tag{6.16}$$

As a matter of fact, $A(\omega)$ is the result of the summation of two terms at different frequencies and thus can be graphically represented in the complex plane, as shown in figure 6-12. The blue vector represents the wave reflected by the fault with amplitude A_1 and time delay τ_1, whereas the red vector represents the wave combined by fault-junction multiple reflections with amplitude A_2 and time delay τ_2. The rotation velocities of these two vectors are clearly different, being different the time delays. As a result of this vector summation, the effective peak found with the projection procedure by the Pseudo-spectrum function is not the green point as would have been in the single line case but the orange point which moves around. This is the reason why oscillations around the fault position occur. It is the physical phenomena of beat, in acoustic and electromagnetism

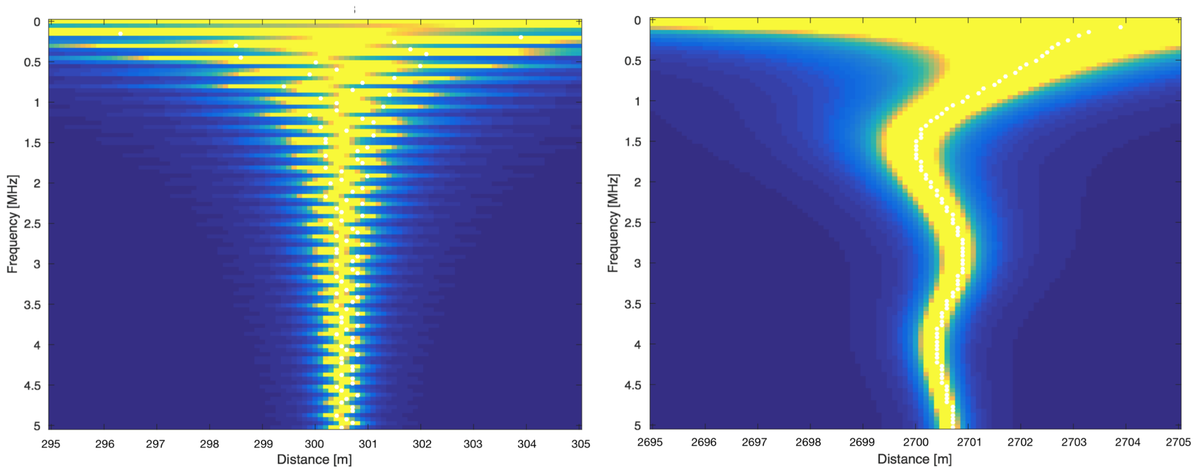

(a) *300 far from the testing port* (b) *300 far from the junction*

Figure 6-13: Pseudo-spectra of the Y-branched structure of figure 6-8 where the fault position has changed

very common, where the addition of different frequencies results in positive or negative interferences. To better understand, the oscillations occur since the *approximated* Green functions are considered in the computation: in fact, the Green functions are calculated at each position of the healthy line, and thus no real faults are included in. But, when a junction is present in the line multiple reflections occur between it and the real fault and another term arises as shown in equation 6.7, which is not included in the approximated Green functions terms. This additional term is the effective cause of the presence of oscillations.

6.3.1 Change of Fault Position

According to figure 6-12, higher the difference of frequencies is more interference between frequencies occur and, consequently, more oscillations around the fault position are shown in the Pseudo-spectrum. In other words, higher the distance between the fault and the junction is, more oscillations around the fault position are present. Vice versa, lower the distance is, less oscillations are present around the fault position: this is the worst case since a *bias* is formed and for certain number of frequency samples the peak is wrongly detected. In figure 6-13 these new configurations are shown: in (a) the fault is situated at 300m from the testing port 3 and 2.7km from the junction, whereas in (b) at 2.7km from the testing port 3 and 300m from the junction. In this last plot the bias is evident and, above all for the lowest frequencies the fault candidates individuated by the projection procedure are quite far from the exact fault position. Considering instead, the same structure of figure 6-8 but with the fault in the middle of the branch 1 and 2, respectively, the Pseudo-spectra are presented in figure 6-14. Also in this case,

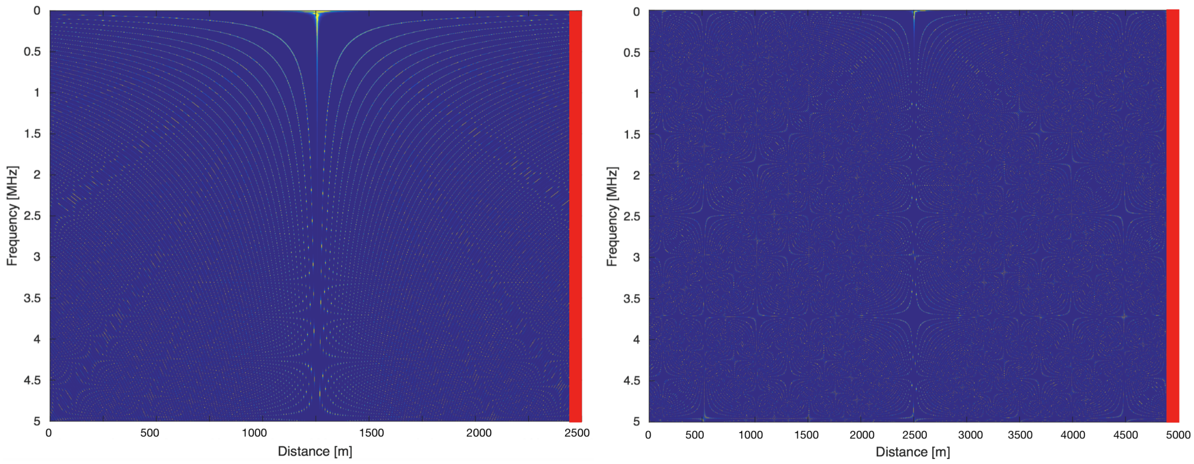

(a) *Branch 1*

(b) *Branch 2*

Figure 6-14: Pseudo-spectra of the Y-branched structure of figure 6-8 where the fault is situated in different branches

Port MUSIC finds the faulty branch first and then the Green function corresponding to the exact fault position, whereas in the other healthy branches only peaks belonging to the ghosts are present. In 6.14(b), where the fault is included in the second branch, it is possible to observe the highest density of ghosts, evident above all around the fault position. This is due to the the fact that the length of the second branch is greater than the first branch and, being the maximum frequency the same at 5MHz (baseband), the distance between the ghosts decreases. According to this case, it is interesting to point out that when the fault is at 300m from the testing port the oscillations are even more since the distance between the junction and the fault has increased, creating a yellow path in the Pseudo-spectrum at the fault position (figure 6-15). Therefore, increasing the

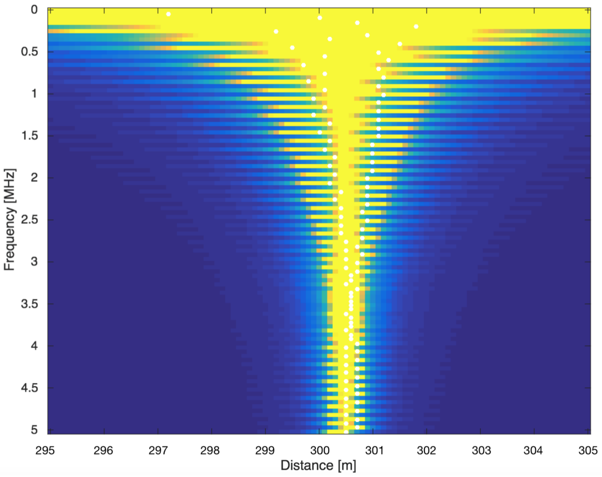

Figure 6-15: Pseudo-spectrum when the fault is on the branch 2 and 300m from the testing port

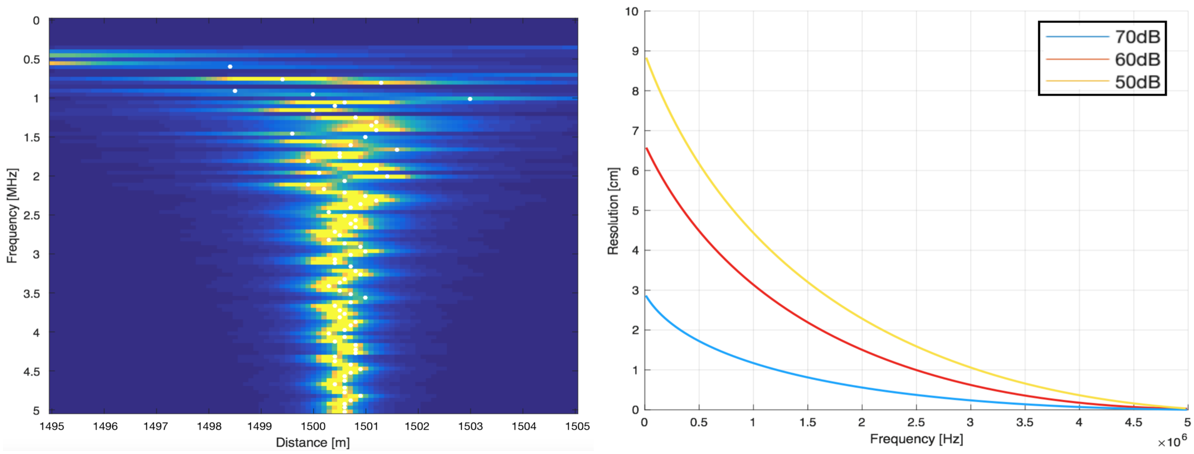

(a) *Accuracy estimation with 20dB SNR and 100 noise realizations* (b) *Precision estimation considering three different SNR values*

Figure 6-16: Port MUSIC performances in the Y-branched structure of figure 6-8

distance between the two discontinuities (fault and junction) more accuracy about the fault position is performed and, ideally, for very long distances the junction weight could be neglected.

6.3.2 Precision and Accuracy Estimation

For a single line, both in lossless and lossy case, the greatest strength of Port MUSIC method is its super resolution, which ensures very precision estimates in the fault location. In the three-dimensional case, the effects of the junction on the method performances are evaluated and a deterioration in accuracy estimation is verified due to the presence of oscillations. The situation gets even worse in presence of noise when the standard deviation over a certain number of noise realizations becomes larger. For example, the Pseudo-spectrum at 20dB SNR is shown in figure 6.16(a). In this case, σ over 100 noise realizations is 0.128, much higher than the 20dB case in a single line. However, it is not a value that can be taken into account since the accuracy estimation is influenced by the presence of oscillations.

Instead, Port MUSIC still ensures a very super resolution performances also in this three-dimensional case, in the range of centimeter and millimeter, depending on the frequency value. As done for the single line case, the 70dB, 60dB and 50dB SNR cases are presented, and the behavior of the spatial resolutions in frequency is shown (figure 6.16(b)). The resolution is slightly increased with respect to the single line case, probably due to the fact that now the projection involves the sum of two vectors. However, super resolution is still achieved and it is important to remind that TDR would perform the same resolution range for bandwidths around 10GHz.

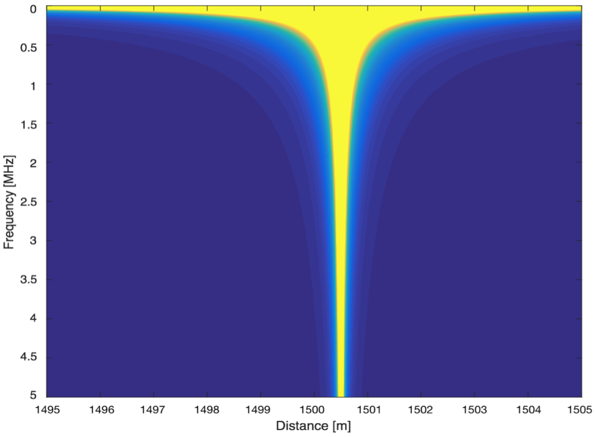

(a) *Pseudo-spectrum when dummy faults are inserted in the Y-branched structure of figure 6-8*

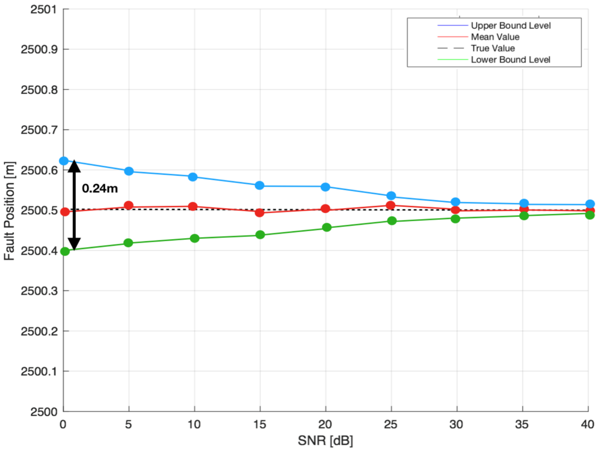

(b) *CDF of the NUT in figure 6-8 with 100 noise realizations and SNR=20dB in presence of dummy faults*

Figure 6-17: Dummy faults

6.3.3 Dummy Faults

In order to improve the performances of MUSIC in a Y-branched structure, it is possible to proceed inserting dummy faults at each position along the line, junction included. The projection procedure is the same as before, with the data scattering matrix computed in the same way. The difference, in this case, is that the "*real* " Green functions are considered and involved in the projection procedure and, thus, the multiple reflections between junction and fault are included into them. In other words, real dummy faults are now present at each position of the line: when the Green function is now generated, reflections occur between junction and the *real* fault, which can be totally compared with the S_{11} reflected wave back propagating. As consequence, oscillations around the fault position are not present and the fault is localized with great accuracy (figure 6.17(a)).

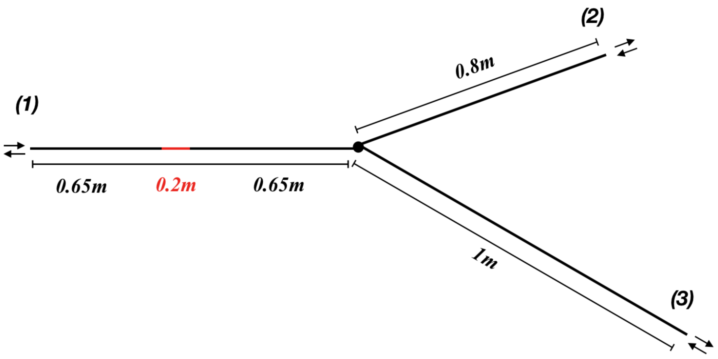

Figure 6-18: Y-branched structure adopted for the experimental results

As procedure, dummy faults with the same length as the real fault are added at each position of the structure, at each branch. The real Green function generated by a dummy fault at each position is computed and its orthogonal vectors carried out.

The super resolution of MUSIC is still performed, whose results are the same as the case in the section 6.3.2 and, beside, the accuracy estimation can be now evaluated. In fact, since no more oscillations are present the fault can be detected without systematic errors. With this in mind, the same approach considered in chapter 4 is studied, where a Monte Carlo simulations with 100 noise realizations is considered. In order to compare this 3-ports system results with the results obtained in the single line case, the same SNR values are considered going from 40dB to 0dB. The cumulative density function is calculated with the upper and the lower bound level at 97.5% and 2.5% of the correspondent *CDF* respectively. As result, the accuracy estimation has improved in this three-dimensional case, and MUSIC performs a better noise robustness with respect to the 2-ports case, as represented in figure 6.17(b). The reason why is probably due to the fact that more data are considered with respect to the bi-dimensional case, resulting in a better accuracy estimation.

6.4 Experimental Results

As done for the single 2 ports-line, the experimental Port MUSIC performances are evaluated also in the case of a Y-branched structure. The experiments set-up is the same as the one adopted in section 5.3, but for sake of clarity, we briefly reintroduce the measurement instruments. High frequency coaxial cables with 50Ω of characteristic impedance are chosen as transmission lines. The soft faults are simulated by using 20cm semi-rigid cables and crushing them in a little portion with 1cm length and 1.4mm thickness. The ends of the cables making up each NUT were used as testing ports, by connecting them to a Rohde&Schwarz ZVB8 vector network analyzer, covering a frequency range from

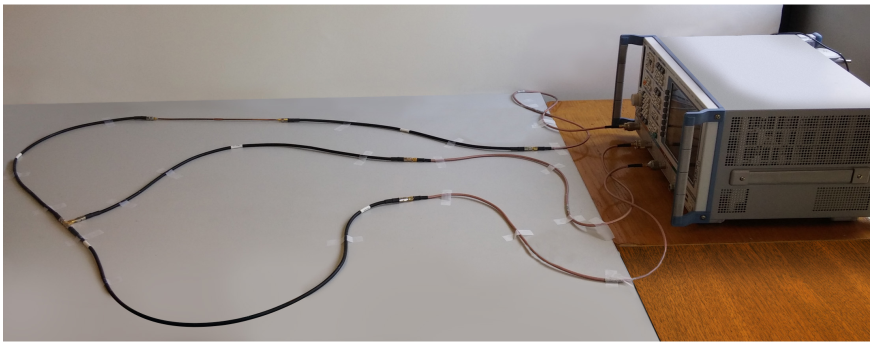

Figure 6-19: Practical implementation in the Y-branched case

300kHz to 8GHz, with four testing ports. The measurement of the scattering matrices was done over a predefined bandwidth ranging from 1MHz to 1GHz and the intermediate-frequency filter bandwidth was set to 100 kHz. After having calibrated the VNA using the calibration kit provided by the manufacturer, the study of the network configuration has been carried out following two steps:

(1) measurement of S_{11}^{b} of the reference healthy system with the unaltered 20cm semi-rigid sections;

(2) measurement of S_{11}^{f} of the NUT, after having replaced the reference samples with the crushed ones.

After having measured the two scattering matrices of the tested networks, post-processing was done by using Matlab where several steps are followed to obtain the results. The line considered is a Y-branched line, where the line lengths of the three branches is shown in figure 6-18. First of all, the experiments have been done by considering the approximated Green functions, computed at each line position without a real fault. The fault is situated in the first branch, with the first termination at 65cm from the testing port 1, and the picture of the implementation is shown in figure 6-19. Besides, the fault position has been changed in order to see its effects on the oscillations, and the Pseudo-spectra shown in figure 6-20, considering the cases in which the semi-rigid line has been inserted at 35cm (b) and 95cm (c) from the testing port of the branch 1. Since the maximum frequency considered here is 500MHz, the distance between the ghosts at that frequency is around 10cm. Here, the Pseudo-spectra are plotted considering 40cm of range in order to show the oscillations around the fault position. As expected and shown in the simulations, oscillations are present due to the multiple reflections between junction and fault and they are stronger as the fault is far from the junction. However, inserting dummy faults at each position of the line, as seen in the previous section, the real function are considered and since in this case the multiple reflections are included in the Green functions no oscillations occur around the fault position. The case (a) is

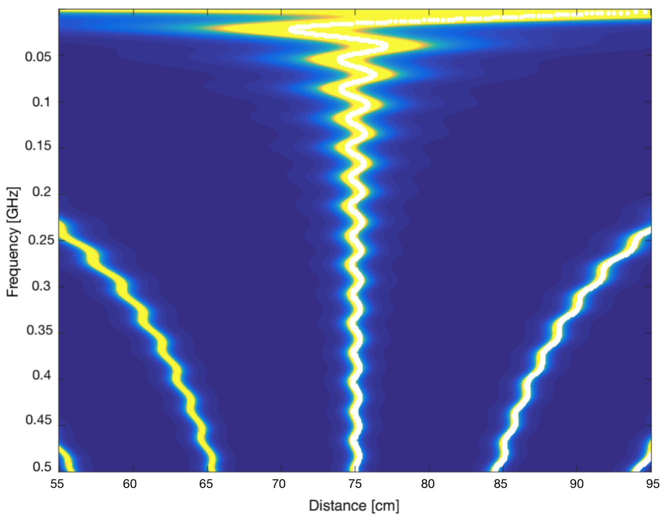

(a) *65cm from the testing port*

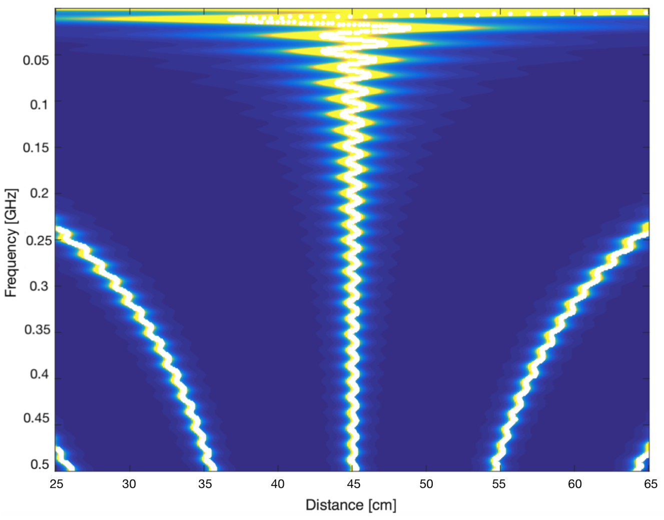

(b) *35cm from the testing port*

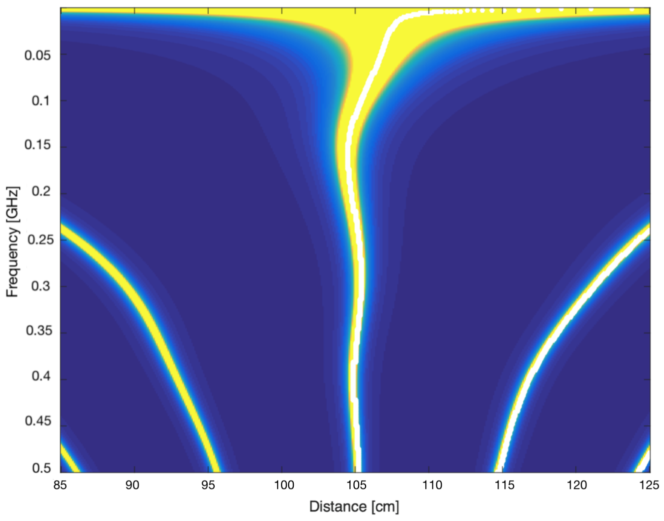

(c) *95cm from the testing port*

Figure 6-20: Pseudo-spectra carried out with VNA measurements

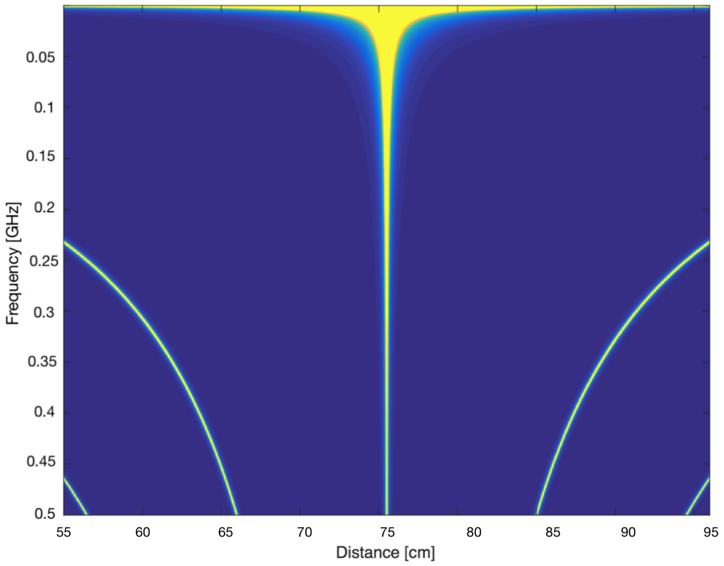

Figure 6-21: Pseudo-spectrum carried out with VNA measurements inserting dummy faults

considered and looking at figure 6-21 a comparison with the oscillations case can be done, where it is evident the same fault position but without the presence of oscillations.

6.5 Summary

In this chapter a more complex structure has been analyzed, with three branches and a junction. First of all, the baselining system has been introduced and deeply discussed aimed to avoid the effect of the junction.

TDR performances are then evaluated where a triangulation is needed and all the testing ports must be used. In the single line case an advantage of TDR with respect to MUSIC was the possibility of using just a single port, which is no more valid in a three-dimensional case.

At last, Port MUSIC is studied: oscillations are shown in the Pseudo-spectrum since multiple reflections arise between fault and junction. To solve this problem, dummy faults at different positions of the line are introduced and their Green functions computed. Besides, super resolution is still performed and an improvement in accuracy is carried out.

Chapter 7

General Conclusions and Perspectives

7.1 Conclusions

A fine analysis of the time reversal method has been presented in this thesis work. The measurement process described pretends to be something that can be used and improved for future measurements in soft fault detection environments.

A 10km medium voltage cable is adopted as NUT and a soft fault simulated as an impedance discontinuity of 1m length. First, TDR method is implemented and a fine comparison with time reversal carried out in order to overcome its limitations. Actually, as seen in chapter 3, different TR methodologies are taken into account but after a deep analysis on each of them (DORT, standard MUSIC, Frequency-delay MUSIC and Port MUSIC), Port MUSIC showed several advantages which lead us to consider it in the performances comparison with TDR.

In chapter 4 a lossless line is considered and a metrological analysis on precision and accuracy estimations of both the methods is carried out. As a result, in precision estimation a super resolution is performed by Port MUSIC (on the order of the millimeter) even with a quite limited bandwidth ($f_{max} = 10MHz$), whereas TDR needs very large bandwidths for achieving such a resolution. Moreover, at the same noise conditions the two methods perform the same accuracy estimation, studying their behavior at different SNR values (from 40dB to 0dB), see figure 4-29. Therefore, in absence of losses, Port MUSIC shows multiple advantages than TDR since performs the same accuracy and a much better precision in fault location. The price to be paid is that MUSIC operates only if the entire length of the line is known a priori and both the testing ports must be used, whereas TDR needs just a single port.

Adding losses the work becomes even more interesting. In fact, limitations in frequency are introduced in TDR in order to reduce the attenuation value. Being TDR a time-domain based method, reducing the frequency a worse resolution has obtained (figure 5-14), around 320m. Instead, Port MUSIC performs great results since is only affected by dispersion, operating just on Green function phase patterns and thus attenuation does not influence its performances. A super resolution on the millimeter order is still achieved, going beyond the limitations encountered by TDR.

In the last chapter (6), the fault detection analysis is carried out on a Y-branched structure. Both TDR and MUSIC need all the testing ports to operate in this case even if MUSIC still require the knowledge of the branches length. Here, the baselining system is introduced in order to avoid the cumbersome effect of the junction. In fact, multiple reflections originate between fault and junction which create oscillations in the Pseudo-spectra around the fault position. This problem is bypassed introducing dummy faults along the line (section 6.3.3). Super-resolution is still accomplished in MUSIC and accuracy improved with respect to the single line case.

To conclude, different topologies and effects of a 10 km power cable have been analyzed in this thesis in order to compare some fault detection methods. Port MUSIC showed very good results, exceeding the limitations encountered by TDR. In particular, some of its strength points can be briefly listed:

(1) it is based on a Green function analysis deriving from a subspace decomposition of the scattering matrix: no time-domain reflected waves are involved and, thus, the problems arisen in the time-domain methods (as TDR) in presence of losses are overcome;

(2) its ability to operate on phase patterns only since a projection procedure involving Green function and S parameters is carried out;

(3) its ability to operate frequency by frequency, which allows the choice of specified frequency samples if distortion is present.

Numerical validations and experiments with VNA are also carried out in order to practically validate the models. With this work an application of MUSIC on MV cables is performed and good results are obtained. However, several applications can be studied and carried on in order to still improve the soft fault detection in power cables.

7.2 Perspectives

We decided to operate in this work adopting time reversal properties to the problem of fault location in transmission lines. Good results are obtained with single as well as Y-branched networks in lossless/lossy conditions. However, an extended study could be continued in order to still improve the methods performances. Some of these perspectives are listed in this section:

- implementation of a new version of MUSIC, in this work just introduced in its concepts in section 3.4.2, *Frequency-delay MUSIC*, which builds the vectors $\underline{v}_1$ and $\underline{g}(x)^{\perp}$ in function of frequency and not depending on the number of testing ports. It implies a greater set of data to be analyzed and, consequently, a more noise robustness and a better accuracy estimation shall be expected;

- the practical experiments on very long MV power cables in order to experimentally validate the theory also on bigger cables are required. For this purpose, the proper instruments are needed, for measuring and to be measured;

- implementation of time reversal, and in particular TR-MUSIC, on more complex structures, with several branches (>3) and junctions;

- analysis of TDR and time reversal in presence of active electrical components in the line (as voltage/current sources, transformers, electronic components) in order to observe and study the response of the structure, both in time and frequency domains. The adoption of the EMTP software can be applied in order to numerically validate the results;

- improvements in DORT method to make it applicable using reflection coefficients only and not the whole scattering matrix S;

- analysis and study of different networks: open-load, short-circuits in order to have multiple reflections and in presence of multiple faults. In those cases DORT should be more advantageous than the other fault location methods. In such a case, the comparison in methods performances could be very useful, even between time reversal methods;

- application of TR-MUSIC on other cable structures, different from coaxial cables. In this case, a study of the cable structure and the frequency dependence with its electrical parameters is initially needed and its consequent mapping in relation to attenuation.

Glossary

List of Acronyms

CDF	Cumulative Density Function
CLT	Central Limit Theorem
CST	Computer Simulation Technology
DOA	Direction Of Arrival
DORT	Decomposition de l' Operateur de Retournement Temporel
EDF	Electricite De France
EMI	Electro Magnetic Induction
EVD	Eigen Value Decomposition
FDR	Frequency Domain Reflectometry
MTL	Multi-conductor Transmission Line
MUSIC	Multiple Signal Classification
MV	Medium Voltage
MWS	Micro Wave Studio
NUT	Network Under Test
PEC	Perfect Electrical Conductor
SNR	Signal to Noise Ratio
SSTDR	Spread Spectrum Time Domain Reflectometry
SVD	Singular Value Decomposition
TDR	Time Domain Reflectometry
TEM	Transverse Electro Magnetic
TOSM	Through Open Short Match
TR	Time Reversal
TRM	Time Reversal Mirror
TRO	Time Reversal Operator
VNA	Vector Network Analyzer

XLPE	Cross Linked PolyEthylene
ZT	Space-Time Diagram

Mathematical Notations

$\mathbb{R}$	set of real numbers
$\underline{x}$	generic column vector
$\underline{x}^{\dagger}$	transpose conjugate of column vector
$\underline{x}^{\perp}$	orthogonal of column vector
$\lambda(\mathit{\Lambda})$	eigenvalues of the matrix $\mathit{\Lambda}$
$\mathrm{diag}(\cdots)$	diagonal matrix
$E[\cdot]$	expected value of
$\approx$	approximated by
$\triangleq$	defined as
$\mathcal{S}$	signal subspace
$\mathcal{N}$	noise subspace
$\underline{g}(x)$	Green function vector
σ	variance of
K	time reversal operator
$\Re\boldsymbol{e}(\cdot)$	real part of
$e_0(t)$	time-domain reflected wave

List of Figures

List of Tables

Bibliography

[1] T. Edison. Electric conductor. *US Patent*, pages 470, 924, Mar 1892.

[2] F. Auzanneau. Wire troubleshooting and diagnosis: Review and perspectives. *Progress In Electromagnetics Research B*, 49:253–279, Mar 2013.

[3] M. Kafal. *Imaging Techniques for soft fault detection and location in wiring networks*. PhD thesis, Nov 2016.

[4] A. G. Bell. Telephone-circuit. *US Patent*, pages 244, 426, Jul 1881.

[5] C. Teal and C. Satterlee. Managed aircraft wiring health directly relates to improved avionics performance. In *Digital Avionics Systems Conference, 2000*, volume 1, pages 3B6–1, Sept 2000.

[6] C. Buccella, M. Feliziani, and G. Manzi. Identification and localization of defects in shielded cables by a numerical/experimental procedure. In *Electromagnetic Compatibility, 2003 IEEE International Symposium*, volume 1, pages 213–218, Jan 2003.

[7] J. Schonfeld, O. Greulich, A. Patterson-Hine, L. Lee, J. Cockrell, and L. Hofland. Wire integrity research (wire) research study. *Doc. No. A0SP-0001-XB1*, 2000.

[8] K. R. Wheeler, I. X. Twombly, K. F. Goebel, and P. F. Wysocki. Aging aircraft wiring fault detection survey. 2007.

[9] L. A. Griffiths, R. Parakh, C. Furse, and B. Baker. The invisible fray: A critical analysis of the use of reflectometry for fray location. *Sensors Journal, IEEE*, 6(3):607–706, Mar 2006.

[10] L. A. Pereira Dos Santos. *Développement d' une nouvelle méthode de détermination des profils de teneur en eau dans les sols par inversion d' un signal TDR*. PhD thesis, September 1997.

[11] R. J. Woodward. Using frequency domain reflectometry for water level measurement. 2000.

[12] C. Neus, P. Boets, and L. Van Biesen. Channel capacity estimation of digital subscriber lines: a frequency domain approach. *ICC, Citeseer*, pages 2676–2681, 2007.

[13] C. Furse, Y. C. Chung, C. Lo, and P.Pendayala. A critical comparison of reflectometry methods for location of wiring faults. *Smart Structures and Systems*, 2(1):25–46, 2006.

[14] L. Abboud. *Application des techniques de retournement temporel au diagnostic filaire automobile et avionique.* PhD thesis, Mar 2012.

[15] N. Ravot, F. Auzanneau, Y. Bonhomme, M. Olivas, and F. Bouillault. Distributed reflectometry-based diagnosis for complex wired networks. *EMC: Safety, Reliability and Security of Communication and Transportation Syst*, 2007.

[16] R. O. Schmidt. Multiple emitter location and signal parameter estimation. *Antennas and Propagation, IEEE Transactions*, 34(3):276–280, 1986.

[17] A. Cozza and L. Pichon. Echo response of faults in transmission lines: Models and limitations to fault detection. *IEEE*, 2013.

[18] C. R. Paul. Analysis of multiconductor transmission lines. *John Wiley and sons*, 2008.

[19] M. Franchet. *Réflectométrie appliquée a la détection de défauts non francs dans les torons de câbles.* PhD thesis, Université Paris-Est, 2012.

[20] C. M. Studio. v5. 0. *Computer Simulation Technology*, 2003.

[21] K. S. Yee. Numerical solution of initial boundary value problems involving maxwell’ s equations in isotropic media. *IEEE Trans. Antennas Propag*, 14(3):302–307, 1966.

[22] K. S. Kunz and R. J. Luebbers. The finite difference time domain method for electromagnetics. *CRC press*, 1993.

[23] D. M. Pozar. Microwave engineering. *John Wiley and sons*, 2009.

[24] M. B. Steer. Microwave and rf design: a systems approach. *SciTech Publication*, 2010.

[25] A. Cozza. *Railways EMC: Assessment of infrastructure impact.* PhD thesis, Université des Sciences et Technologie de Lille-Lille I, 2005.

[26] V. Vahedy. Polymer insulated high voltage cables. *IEEE Electrical Insulation Magazine*, 22(3), 2006.

[27] G. Mugala. High frequency characteristics of medium voltage xlpe power cables. *IEEE Electrical Insulation Magazine*, 2008.

[28] A. Ponniran, N. A. M. Jamail, and N. A. Jalaludin. Tan delta and capacitance characteristics of underground XLPE cables. *Proceedings of MUCEET*, 2009.

[29] L. Qian and Z. Shan. Coaxial cable modeling and verification.

[30] T. Liu, J. Fothergill, S. Dodd, and U. Nilsson. Influence of semicon shields on the dielectric loss of xlpe cables.

[31] N. Merabtine H. Mokhtari, M. M. Alharthi. Psice model for a coaxial cable in high frequency domain submitted to a longitudinal temperature gradient using kelvin-bessel asymptotic functions.

[32] Nexans. Iec-60502-2, nf-c-12/20kv.

[33] J. C. Fothergill, S. J. Dodd, and L. A. Dissado. The measurement of very low conductivity and dielectric loss in xlpe cables: a possible method to detect degradation due to thermal aging. *J. C. Fothergill et al.: The Measurement of Very Low Conductivity and Dielectric Loss in XLPE Cables*, 2010.

[34] F. M. Tesche. A simple model for the line parameters of a lossy coaxial cable filled with a nondispersive dielectric. *IEEE transaction on Electromagnetic Compatibility*, 49(1), Feb 2007.

[35] N.H. Rahim, S. Chairul, S. A. Ghani, M.S. Khiar, and N. Abas. Simulation of tdr circuit for the analysis of wave propagation in xlpe cable model. *IEEE International Conference on Power and Energy (PECon)*, 2012.

[36] O. Gatous and J. P. Filho. A new fomulation for skin-effect resistance and internal inductance frequency-dependent of a solid cylindrical conductor. *IEEE/PES Transmission and distribution conference and exposition: Latin America*, 2004.

[37] T. R. Blackburn and B. T. Phung. The effect of insulation loss and semi-conducting layers on pulse propagation behavior of power cables. *IEEE*, 2004.

[38] A. Medjdoub, A. Boubakeur, and T. Lebey. Broad band dielectric investigation of cross-linked polyethylene use as electrical insulation on underground power cables. *Annual Report Conference on Electrical Insulation and Dielectric Phenomena*, 2010.

[39] C. Paul. Analysis of multiconductor transmission lines. Oct 2007.

[40] A. Parvulescu and C. Clay. Reproducibility of signal transmissions in the ocean. *Radio and Electronic Engineer*, 29(4):223–228, 1965.

[41] M. Fink, C. Prada, F. Wu, and D. Cassereau. Self focusing in inhomogeneous media with time reversal acoustic mirrors. *Ultrasonics Symposium, IEEE*, pages 681–686, 1989.

[42] M. Fink. Time reversal of ultrasonic fields. i. basic principles. *Ultrasonics, Ferroelectrics and Frequency Control, IEEE Transactions*, 39(5):555–566, 1992.

[43] F. Wu, J.-L. Thomas, and M. Fink. Time reversal of ultrasonic fields. il. experimental results. *Ultrasonics, Ferroelectrics and Frequency Control, IEEE Transactions*, 39(5):567–578, 1992.

[44] D. Cassereau and M. Fink. Time-reversal of ultrasonic fields. iii. theory of the closed time- reversal cavity. *Ultrasonics, Ferroelectrics and Frequency Control, IEEE Transactions*, 39(5):579–592, 1992.

[45] J. L. Thomas, F. Wu, and M. Fink. Time reversal focusing applied to lithotripsy. *Ultrasonic imaging*, 18(2):106–121, 1996.

[46] C. Le Floch, M. Tanter, and M. Fink. Self-defocusing in ultrasonic hyperthermia: Experiment and simulation. *Applied physics letters*, 74(20):3062–3064, 1999.

[47] C. Larmat, J.-P. Montagner, M. Fink, Y. Capdeville, A. Tourin, and E. Clévédé. Time-reversal imaging of seismic sources and application to the great sumatra earthquake. *Geophysical Research Letters*, 33(19), 2006.

[48] P. Kosmas and C. M. Rappaport. Time reversal with the fdtd method for microwave breast cancer detection. *Microwave Theory and Techniques, IEEE Transactions*, 53(7):2317–2323, 2005.

[49] M. Fink and C. Prada. Acoustic time-reversal mirrors. *Inverse problems*, 17(1):R1, 2001.

[50] G. Lerosey, J. De Rosny, A. Tourin, A. Derode, G. Montaldo, and M. Fink. Time reversal of electromagnetic waves. *Physical review letters*, 92(19):193904, 2004.

[51] M. Fink, D. Cassereau, A. Derode, C. Prada, P. Roux, M. Tanter, J. l. Thomas, and F. Wu. Time-reversed acoustics. *Reports on progress in Physics*, 63(12):1933, 2000.

[52] C. Prada, S. Manneville, D. Spoliansky, and M. Fink. Decomposition of the time reversal operator: Detection and selective focusing on two scatterers. *The Journal of the Acoustical Society of America*, 99(4):2067–2076, 1996.

[53] D. Clorennec, J. De Rosny, J.-G. Minonzio, C. Prada, M. Fink, T. Folegot, P. Billand, S. Tauvry, S. Hibral, and L. Bernière. First tests of the dort method at 12 khz in a shallow water waveguide. *Oceans 2005-Europe*, 2:1205–1209, 2005.

[54] M. Fink and C. Prada. Eigenmodes of the time reversal operator: A solution to selective focusing in multiple-target media. *Wave motion*, 20(2):151–163, 1994.

[55] N. Maaref, P. Millot, X. Ferrieres, C. Pichot, and O. Picon. Electromagnetic imaging method based on time reversal processing applied to through-the-wall target localization. *Progress In Electromagnetics Research M*, 1:59–67, 2008.

[56] C. Prada, F. Wu, and M. Fink. The iterative time reversal mirror: a solution to self-focusing in the pulse echo mode. *The Journal of the Acoustical Society of America*, 90(2):11191129, 1991.

[57] M. Fink. Time-reversal mirrors. *Journal of Physics D: applied Physics*, 26(9):1333, 1993.

[58] H. Tortel, G. Micolau, and M. Saillard. Decomposition of the time reversal operator for electromagnetic scattering. *Journal of Electromagnetic Waves and Applications*, 13(5):687–719, 1999.

[59] H. Lev-Ari and A. Devancy. The time-reversal technique re-interpreted: subspace-based signal processing for multi-static target location. *Sensor Array and Multichannel Signal Processing Workshop. 2000. Proceedings of the 2000 IEEE*, 2:509–513, 2000.

[60] A. Devaney. Time reversal imaging of obscured targets from multistatic data. *Antennas and Propagation, IEEE Transactions*, 53(5):1600–1610, 2005.

[61] C. Prada, J.-L. Thomas, and M. Fink. The iterative time reversal process: analysis of the convergence. *The Journal of the Acoustical Society of America*, 97(1):62–71, 1995.

[62] B. Y. Zel' Dovich, N. F. Pilipetsky, and V. V. Shkunov. Principles of phase conjugation. *Springer*, 42, 2013.

[63] E. A. Marengo, F. K. Gruber, and F. Simonetti. Time-reversal music imaging of extended targets. *Image Processing, IEEE Transactions*, 16(8):1967–1984, 2007.

[64] A. Baussard and T. Boutin. Time-reversal rap-music imaging. *Waves in Random and Complex Media*, 18(1):151–160, 2008.

[65] S. Flax and M. O' Donnell. Phase-aberration correction using signals from point reflectors and diffuse scatterers: basic principles. *Ultrasonics, Ferroelectrics, and Frequency Control, IEEE Transactions*, 35(6):758–767, 1988.

[66] A. Spanias J. Foutz and M. K. Banavar. Narrowband direction of arrival estimation for antenna arrays. *Synthesis Lectures on Antennas*, 3(1):758–767, 2008.

[67] F. K. Gruber, E. A. Marengo, and A. J. Devaney. Time-reversal imaging with multiple signal classification considering multiple scattering between the targets. *The Journal of the Acoustical Society of America*, 115(6):3042–3047, 2004.

[68] W. Gao, X. Wang, and B. Wang. Review of time reversal imaging techniques.

[69] T. Miwa and I. Arai. Super-resolution imaging for point reflectors near transmitting and receiving array. *Antennas and Propagation, IEEE Transactions*, 52(1):220–229, 2004.

[70] D. Ciuonzo, G. Romano, and R. Solimene. Performance analysis of time-reversal music. *Signal Processing, IEEE Transactions*, 63(10):2650–2662, 2015.

[71] A. J. Devaney. Super-resolution processing of multi-static data using time reversal and music. *J. Acoust. Soc. Am*, 2000.

[72] E. Kerbrat, C. Prada, D. Cassereau, and M. Fink. Ultrasonic nondestructive testing of scattering media using the decomposition of the time-reversal operator. *Ultrasonics, Ferroelectrics, and Frequency Control, IEEE Transactions*, 49(8):1103–1113, 2002.

[73] E. Barbieri and M. Meo. Time reversal dort method applied to nonlinear elastic wave scattering. *Wave Motion*, 47(7):452–467, 2010.

[74] C. Prada and J.-L. Thomas. Experimental subwavelength localization of scatterers by de- composition of the time reversal operator interpreted as a covariance matrix. *The Journal of the Acoustical Society of America*, 114(1):235–243, 2003.

[75] NASA. Wire integrity research pilot study final report. 2000.

[76] Y. C. Chung, N. Amarnath, C. Furse, and J. Mahoney. Capacitance and inductance sensors for location of open and short circuited wires. *IEEE Trans Instrum. Meas*, pages 604–613, Jun 2009.

[77] Y. C. Chung, C. Furse, and J. Pruitt. Application of phase detection frequency domain reflec- tometry for locating faults in an f-18 flight control harness. *Electromagnetic Compatibility, IEEE Transactions*, 47(2):327–334, 2005.

[78] C. Furse, Y. C. Chung, R. Dangol, M. Nielsen, G. Mabey, and R. Woodward. Frequency-domain reflectometry for on-board testing of aging aircraft wiring. *Electromagnetic Compatibility, IEEE Transactions*, 45(2):306–315, 2003.

[79] C. Furse and N. Kamdar. An inexpensive distance measuring system for navigation of robotic vehicles. *Microwave and Optical Technology Letters*, 33(2):84–87, 2002.

Acknowledgements

> *[. . .] If a person has no dreams, they no longer have any reason to live. Dreaming is necessary, although in the dream reality should be glimpsed.*
>
> Ayrton Senna

With this piece of paper I concluded six years of studies, full of satisfactions, difficult moments and sacrifice. It has allowed me to grow up in so many points of view and extend my horizons. I would like to thank all the people who support me in this path, making possible the achievement of this goal.

First of all, I'm thankful to my Chinese supervisor, prof. YanZhao Xie who assisted me in every problem I encountered during my period in China, gave me the opportunity for the internship in France and for the several suggestions about the thesis work. Then, thank to my Italian supervisor prof. Flavia Grassi for helping me in the supervision of this work and, together with prof. Sergio Pignari, for making possible the double degree program I attended.

I would like to express my deep gratitude to prof. Andrea Cozza, without him this work would not be possible. For all the time to guide me throughout the period I spent in France and for the endless patience in front of my infinite questions. I'm very glad to have worked with him and I will be always grateful, not only for the professional point of view but above all for his great human level.

In these two years abroad I knew a lot of people and I shared very beautiful moments with some of them. First, I'd like to mention Vigno for all the funny moments spent together in both the years in China and to have made some moments softer with him by my side. With you I found a real friend. Thank also to Fede for the days and the good moments spent together. The older and younger Italian guys have been also very important for me and I'm very happy to have met all of them: Luca, Giami, Gio, Paolino, Antó, Pan, Giaming, Vittoria and Pietro. A thought also to all the Chinese guys who

helped me in so many situations. Every time I need they were always there and I won't never forget their great kindness; a special mention to Qi Tianxing and Wang Xing.

I can't not keep a few rows for two special guys, Betti and Enri. Thank you for having helped me during the first year in China, for making me feel at home and for making me smile every time I need. Maybe I've never told you but I consider you very great friends.

Although the distance, so many people have been very close to me and I'd like to spend some words for all of them. My uncles Alberto and Isa for having support me all this time, my cousins Bettina and Marco, Barbara and Marco. A mention also to Marcolino, who represents for me a very special friend, and Simo.

A particular thought is reserved to all my grandparents. They represent a piece of my hearth and have always been fundamental for me. The person I've become now is also due to their wise teachings. You are the most valuable thing I have.

Last, but not the least, some words to who makes everything possible: my family. My father Vittorio and my mother Nadia always support me every day of my life, both economically and mentally. I owe you everything. A huge thought to Andreolli, a fantastic guy and the brother who everybody would like to have. I'm so proud to be part of your life.

Manuel

Ringraziamenti

> *[...] Se una persona non ha più sogni, non ha più alcuna ragione di vivere. Sognare è necessario, anche se nel sogno va intravista la realtà.*
>
> Ayrton Senna

Con questo pezzo di carta ho concluso sei anni di studi, pieni di soddisfazioni, momenti difficili e sacrifici. Questo percorso mi ha permesso di crescere sotto moltissimi punti di vista e di allargare i miei orizzonti: vorrei ringraziare tutte le persone che mi hanno sostenuto, rendendo possibile il raggiungimento di questo obiettivo.

Prima di tutto, sono grato alla mia relatrice italiana, la professoressa Flavia Grassi per avermi aiutato nella supervisione di questo lavoro e, insieme al professor Sergio Pignari, per aver reso possibile il programma di doppia laurea che ho frequentato. Un grazie poi al mio supervisore cinese, il professor YanZhao Xie che mi ha assistito in ogni problema incontrato durante il mio periodo in Cina e mi ha dato l'opportunità di svolgere lo stage in Francia.

Vorrei esprimere la mia profonda gratitudine al professor Andrea Cozza, senza il quale questo lavoro non sarebbe stato possibile. Per tutto il tempo speso ad aiutarmi durante il periodo trascorso in Francia e per l'infinita pazienza di fronte alle mie numerose domande. Sono molto contento di aver lavorato con lui e sarò sempre grato, non solo dal punto di vista professionale ma soprattutto per la sua grande umanità.

In questi due anni all'estero ho conosciuto molte persone e ho condiviso momenti molto belli con alcuni di loro. Innanzitutto, vorrei menzionare Vigno per tutti i momenti divertenti trascorsi insieme in entrambi gli anni in Cina e aver reso alcuni momenti più dolci con lui al mio fianco. Grazie anche a Fede per i giorni e i bei momenti trascorsi insieme. Anche i ragazzi italiani più vecchi e più giovani sono stati molto importanti per me e sono molto felice di avere incontrato ognuno di loro: Luca, Giami, Gio, Paolino, Anto, Pan, Giaming e Vittoria. Un pensiero anche a tutti i ragazzi cinesi che mi hanno

aiutato in tante situazioni, dei quali non dimenticherò mai la grande gentilezza; una menzione speciale a Qi Tianxing e Wang Xing.

Non posso non scrivere qualche riga per due ragazzi speciali, Betti ed Enri. Grazie per avermi aiutato durante il primo anno in Cina, per avermi fatto sentire a casa e per avermi fatto sorridere ogni volta che ne avevo bisogno. Con voi ho trovato davvero due grandi Amici.

Nonostante la distanza, molte persone mi sono state molto vicine e vorrei spendere qualche parola per tutti loro. I miei zii Alberto e Isa per avermi supportato per tutto questo tempo, i miei cugini Bettina e Marco, Barbara e Marco. Una menzione anche a Marcolino, che rappresenta per me un amico molto speciale, a Simo e a Brambuz.

Un pensiero particolare è riservato a tutti i miei nonni. Rappresentano un pezzo del mio cuore e sono sempre stati fondamentali per me. La persona che sono diventato ora è anche grazie ai loro saggi insegnamenti. Siete la cosa più preziosa che ho.

Ultimo, ma non meno importante, alcune parole per chi ha reso tutto ciò possibile: la mia famiglia. Mio papà Vittorio e mia mamma Nadia mi hanno sempre sostenuto ogni giorno della mia vita, sia economicamente che mentalmente. A voi devo tutto. Un pensiero enorme per Andreolli, un ragazzo fantastico e il fratello che tutti vorrebbero avere. Sono così orgoglioso di far parte della vostra vita.

Manuel